The Development of a Novel Impingement Heat Transfer Device

by

Derwalt Johannes Erasmus

Thesis presented in partial fulfilment of the requirements for the degree of Master of Engineering (Mechanical) in the Faculty of Engineering at Stellenbosch University

Supervisor: Prof. Theodor Willem von Backström

Co-supervisors: Dr. Matti Lubkoll
Prof. Kenneth John Craig

December 2020

Declaration

By submitting this thesis electronically, I declare that the entirety of the work contained therein is my own, original work, that I am the sole author thereof (save to the extent explicitly otherwise stated), that reproduction and publication thereof by Stellenbosch University will not infringe any third party rights and that I have not previously in its entirety or in part submitted it for obtaining any qualification.

Date: 2/09/2020 .....

Abstract

The Development of a Novel Impingement Heat Transfer Device

DJ. Erasmus

Department of Mechanical and Mechatronic Engineering,
Stellenbosch University,
Private Bag X1, Matieland 7602, South Africa.

Thesis: MEng (Mech)

December 2020

Current central receiver Concentrating Solar Power (CSP) plants using molten salt as a heat transfer fluid operate at around 565 °C for heat addition in a thermodynamic cycle. Adding heat at a higher temperature can improve the thermodynamic performance and may reduce the cost of power. One way to achieve this is by using pressurized air solar receivers operating under a high concentration of solar flux at an outlet temperature of around 800 °C and a thermal efficiency exceeding 80 %. A novel high-flux impingement heat transfer device, called the Tadpole, is developed to improve the heat transfer and pressure loss (performance) characteristics of solar receivers such as the Spiky Central Receiver Air Pre-heater (SCRAP) concept.

The Tadpole is scrutinized through an experimental comparison with a conventional jet impinging on the inner wall of a hemisphere. The device demonstrates promising capability by exceeding the performance characteristics of the impinging jet. Multiple dimensional degrees of freedom in the Tadpole's flow domain facilitate obtaining a favourable combination of heat transfer and pressure loss characteristics. A Computational Fluid Dynamics (CFD) model is developed to enable investigating the application potential of the Tadpole. The Four-Equation Transition SST turbulence model demonstrates satisfactory experimental validation with a deviation of $< 5\,\%$ for the heat transfer coefficient and $< 23\,\%$ for the total pressure loss.

The application potential of the Tadpole within the SCRAP concept is explored and compared with a previous favourable impinging jet configuration. It is estimated that the implementation of the Tadpole instead of this impinging jet can result in a 43 % reduction in the total pressure loss of a

SCRAP spike or improved spike tip thermal absorption with a reduction in the spike tip temperature of 33 K. This improved thermal absorption may lead to an improved lifespan of the receiver. However, the receiver's performance improvements are estimated to marginally ($< 1\,\%$) improve the coupled solar hybrid Brayton cycle efficiency and specific fuel consumption.

Based on the Tadpole concept, a novel central air receiver technology called the SUNflower is conceived as an alternative to the SCRAP receiver. An initial performance outlook estimates that an air outlet temperature of 800 °C can be reached at a thermal efficiency of below 63 %. A limitation of the concept is an insufficient exterior surface area to absorb the incoming flux which causes a high surface temperature and radiative heat loss. The SCRAP concept is more suitable because of its larger absorber surface area. Further work on the advancement and integration of the Tadpole within the SCRAP concept is therefore recommended.

To avoid localized overheating, the SUNflower requires a relatively uniform incoming solar flux distribution. A new heliostat aiming strategy called Blossaim is developed to flatten an incoming flux distribution on a circular aperture receiver. An analytical investigation incorporating a Heliopod heliostat field demonstrates promising performance in reducing the peak flux magnitude by 66 % with a reduction in the Heliopod field's optical efficiency of only 2 %.

Uittreksel

Die Ontwikkeling van 'n nuwe Botsing Warmte-oordrag Toestel

("The Development of a Novel Impingement Heat Transfer Device")

DJ. Erasmus

Departement Meganiese en Megatroniese Ingenieurswese,
Universiteit van Stellenbosch,
Privaatsak X1, Matieland 7602, Suid Afrika.

Tesis: MIng (Meg)

Desember 2020

Huidige sentrale ontvanger Gekonsentreerde Sonkrag (GS) stasies wat gesmelte sout as warmte-oordragvloeistof gebruik, werk teen ongeveer 565 °C vir hitte-toevoeging in 'n termodinamiese siklus. Hoër temperatuur hitte-toevoeging kan die termodinamiese benuttingsgraad verbeter en dit kan dalk die koste van krag verminder. Een manier om dit te bereik is om gebruik te maak van höedruk lugontvangers wat onder 'n hoë konsentrasie van sonvloed funktioneer by 'n uitlaat temperatuur van ongeveer 800 °C en 'n termiese benuttingsgraad van meer as 80 %. 'n Nuwe hoë-vloed botsing warmte-oordrag toestel, genaamd die Paddavissie, word ontwikkel om die warmte-oordrag en drukverlies (prestasie-eienskappe) van lugontvangers, soos die Stekelrige Sentrale Ontvanger Lug Voorverwarmer (SCRAP) konsep, te verbeter.

Die Paddavissie word ondersoek deur 'n eksperimentele vergelyking met bestaande straal botsing op die binnewand van 'n halfrond. Dit word gevind dat die Paddavissie in staat is om die prestasie-eienskappe van die botsingstraal te oortref. Verskeie dimensionele vryheidsgrade in die Paddavissie se vloeigebied vergemaklik die verkryging van 'n gunstige kombinasie van warmte-oordrag en drukverlies eienskappe. 'n Berekeningsvloeidinamika (CFD) model word ontwikkel om die toepassingspotensiaal van die Paddavissie te ondersoek. Die Vier-vergelyking 'Transition SST' turbulensiemodel is gestaaf met die eksperimentele resultate met 'n afwyking van $< 5\,\%$ vir die warmte-oordragskoëffisiënt en $< 23\,\%$ vir die totale drukverlies.

Die toepassingspotensiaal van die Paddavissie binne die SCRAP ontvanger word ondersoek en vergelyk met 'n vorige gunstige botsingstraal konfigurasie.

Die implementasie van die Paddavissie in plaas van hierdie botsingstraal in die SCRAP kan lei tot 'n 43 % vermindering in totale drukverlies of verbeterde warmte-oordrag binne die spitspunt met 'n vermindering in die spitspunt se temperatuur van 33 K. Hierdie verbeterde warmte-oordrag kan lei tot 'n langer leeftyd van die ontvanger. Hierdie verbeterings van die ontvanger mag egter lei na marginale verbeterings in die gekoppelde Brayton-siklus se benuttingsgraad en spesifieke brandstofverbruik van < 1 %.

Gebaseer op die Paddavissie, word 'n nuwe sentrale lugontvanger-tegnologie genaamd die Sonneblom ondersoek as 'n alternatief aan die SCRAP ontvanger. 'n Aanvanklike vooruitsig skat dat 'n uitlaat temperatuur van 800 °C bereik kan word teen 'n termiese benuttingsgraad van minder as 63 %. 'n Beperking van die konsep is 'n onvoldoende absorber oppervlakte om die inkomende vloed op te neem. Hierdie veroorsaak 'n hoë oppervlaktemperatuur en hoë stralingshitteverlies. Die SCRAP ontvanger is meer geskik weens 'n groter absorberoppervlak. Verdere werk aan die bevordering en integrasie van die Paddavissie binne die SCRAP ontvanger word dus aanbeveel.

Om gelokaliseerde oorverhitting te voorkom, benodig die Sonneblom 'n relatiewe eenvormige inkomende vloedverspreiding. 'n Nuwe heliostaat-mikstrategie genaamd Blossaim word ontwikkel om 'n inkomende vloedverspreiding op 'n sirkelvormige ontvangeropening te produseer. 'n Analitiese ondersoek wat 'n Heliopod-heliostaatveld modelleer, toon belowende prestasie met 'n 66 % vermindering van die maximum vloeddigtheid en 'n vermindering in die Heliostaatveld se optiese benuttingsgraad van slegs 2 %.

Acknowledgements

I express gratitude to:

- Prof. Theodor von Backström for his invaluable mentorship and support throughout this journey.
- Dr. Matti Lubkoll for his guidance and for representing an inspiring example of excellence.
- Prof. Ken Craig for hosting me at the University of Pretoria and for his guidance and assistance with CFD modelling as well as Mr. Jesse Quick for our valuable discussions and his assistance with CFD modelling.
- Dr. Alberto Sánchez-González for hosting me at Universidad Carlos III de Madrid, for enthusiastic conversations and guidance on solar flux modelling and heliostat fields.
- Mr. Pine van Wageningen for his assistance with 3D printing Tadpole prototypes as well as Mr. Cobus Zietsman, Mr. Graham Hammerse and Mr. Nathi Hlempu for their assistance on experimental apparatus modifications.
- The Solar Thermal Energy Research Group (STERG) for an encouraging research environment.
- The South African Centre for High Performance Computing (CHPC) and Stellenbosch University's Rhasatsha High Performance Computer for their computational power.

The financial assistance of the Solar Thermal Energy Research Group (STERG) and the Erasmus+ programme of the European Union are acknowledged. The European Commission's support for the production of this publication does not constitute an endorsement of the contents, which reflect the views only of the authors, and the Commission cannot be held responsible for any use which may be made of the information contained therein.

With the support of the Erasmus+ Programme of the European Union

Dedications

I dedicate this work to my almighty father in heaven, Jesus Christ.

Contents

List of Figures

List of Tables

Nomenclature

Constants

R_{air} $= 287.12\,\mathrm{J/(kg\,K)}$

σ $= 5.6703 \times 10^{-8}\,\mathrm{W/(m^2\,K^4)}$

Abbreviations

ABS Acrylonitrile Butadiene Styrene

CC Combined Cycle

CFD Computational Fluid Dynamics

CHPC Centre for High Performance Computing

CSP Concentrating Solar Power

DO Discrete Ordinates

G Gauge pressure sensor

HF High-flux

HP High-pressure

HPC High Performance Computer

HRN High Reynolds Number

HT Heat Transfer

LF Low-flux

LES Large Eddy Simulation

LP Low-pressure

LRN Low Reynolds Number

MCRT Monte-Carlo Ray-Tracing

RANS Reynolds Averaged Navier Stokes

SCRAP Spiky Central Receiver Air Pre-heater

SS Supersonic

SST Shear Stress Transport

sCO_2 Supercritical Carbon Dioxide

SUNflower Stellenbosch University flower

TRL Technology Readiness Level

TS	Transonic
TUI	Text User Interface
US	Up-scaled

Symbols

A	Area	$[\mathrm{m}^2]$
C	Discharge coefficient (orifice plate)	$[-]$
C	Static pressure recovery coefficient	$[-]$
c_p	Specific heat	$[\mathrm{kJ/(kg\,K)}]$
d	Diameter	$[\mathrm{m}]$
DNI	Direct normal irradiance	$[\mathrm{kW/m}^2]$
E	Energy	$[\mathrm{J}]$
E	Velocity approach factor (orifice plate)	$[-]$
H	Heliostat	$[-]$
h	Heat transfer coefficient	$[\mathrm{W/(m}^2\,\mathrm{K})]$
h_fg	Enthalpy of condensation	$[\mathrm{J/kg}]$
I	Irradiation	$[\mathrm{kW/m}^2]$
K	Loss factor	$[-]$
k	Standard deviation multiplier	$[-]$
k	Thermal conductivity	$[\mathrm{W/(m\,K)}]$
k	Turbulence kinetic energy	$[\mathrm{m}^2/\mathrm{s}^2]$
l	Length	$[\mathrm{m}]$
$LCOE$	Levelized cost of electricity	$[\mathrm{USD/kWh}]$
m	Heliostat row	$[-]$
$\dot{m}$	Mass flow rate	$[\mathrm{kg/s}]$
N	Node number	$[-]$
N_Mach	Mach number	$[-]$
Nu	Nusselt number	$[-]$
n	Heliostat identification number	$[-]$
P	Perimeter	$[\mathrm{mm}]$
P	Power	$[\mathrm{W}]$
p	Pressure	$[\mathrm{Pa}]$
$\dot{Q}$	Heat rate	$[\mathrm{W}]$
$\dot{q}$	Heat flux	$[\mathrm{W/m}^2]$
Re	Reynolds number	$[-]$
r	Radius	$[\mathrm{m}]$
SFC	Specific fuel consumption	$[\mathrm{kg/kWh}]$

SLR	Slant range (distance from receiver)	[m]
T	Temperature	[°C]
TI	Turbulence intensity	[−]
V	Velocity	[m/s]
x	Travel distance along mean pathline	[mm]
y^+	Dimensionless distance from a wall (turbulence modelling)	[−]
z	Height	[m]

Greek letters

α	Kinetic energy correction factor	[−]
α	Angle centred from the HT surface origin	[°]
α	Absorptivity	[−]
α'	Angle centred from the Tadpole origin	[°]
α''	Angle centred between the Tadpole and the HT surface origin	[°]
ε	Expansion factor (orifice plate)	[−]
ε	Emissivity	[−]
ε	Turbulence dissipation rate	[m^2/s^2]
ζ	Flow area projection line	[mm]
η	Efficiency	[−]
θ	Angle	[deg]
μ	Dynamic viscosity	[kg/(m s)]
ξ	Axial Tadpole offset from concentricity	[mm]
ρ	Density	[kg/m^3]
σ	Standard deviation	[−]
σ	Stress	[N/m^2]
ϕ	Flow area projection angle	[deg]
ϕ	Normalized characteristic (graphs)	[−]
ω	Specific turbulence dissipation rate	[1/s]
ω	Sun beam to heliostat normal angle	[rad]

Subscripts

abs	Absolute
ap	Aperture
Br	Brayton
c	Nozzle throat
cond	Condensation
DO	Discrete Ordinates

d	Diffuser
dyn	Dynamic
e	External, error
es	Exterior heat transfer surface
F	Flow
f	Fluid
fg	Latent heat
g	Gauge
h	Half angle
hyd	Hydraulic
i	Inner
is	Interior heat transfer surface
it	Inner tube
l	Liquid
n	Nozzle
nose	Tadpole's nose
null	Position of contact between Tadpole and interior HT surface
o	Outer
Pyr	Pyromark
rad	Radiation
s	Static, surface, solid
sat	Saturation
sph	Sphere
t	Tadpole surface, total
th	Thermal
v	Vapour
VM	Von Mises
w	Wetted

Chapter 1

Introduction

1.1 Background

With the onset of global warming, a sustainable future driven by renewable resources is required. Renewable power generation has now advanced to a stage where the levelized cost of electricity ($LCOE$) is competitive with fossil fuels (IRENA, 2020). Energy storage is also required to accommodate the intermittent and cyclic availability of wind and solar resources as well as fluctuations in energy demand.

A Concentrating Solar Power (CSP) plant, harvesting thermal energy from the sun, represents a major value proposition because captured solar thermal energy can be stored on a large scale and harnessed during peak demand periods within a national electricity grid. CSP with thermal storage can serve a "mid-merit to peaking role" along with Combined Cycle Gas Turbines (CCGT) to satisfy the hourly demand fluctuations in the South African energy mix (Gauché *et al.*, 2016).

This research is focused on the development of a new heat transfer device applicable within the receiver of a central receiver CSP plant. A central receiver CSP plant has an array of mirrors, called heliostats, that concentrate reflected sunlight onto the thermal receiver at the top of a tower. Such a concentration can amount to between $1\,\mathrm{MW/m^2}$ and $2\,\mathrm{MW/m^2}$. The receiver captures this heat and transfers it to the heat transfer fluid at a high temperature to add heat to a thermodynamic cycle.

Existing commercial central receiver CSP plants heat a molten salt heat transfer fluid in the receiver to around $565\,^{\circ}\mathrm{C}$ for heat addition in a Rankine thermodynamic cycle. The Rankine cycle uses steam as its working fluid to generate power from the movement of thermal energy through a temperature difference from the central receiver to a condenser. The power blocks of such CSP plants can operate with a thermodynamic cycle efficiency of up to $42\,\%$ (Kolb *et al.*, 2011). Higher temperature head addition to the power block leads to a higher power block efficiency according to the Carnot cycle.

A higher power block efficiency may enable a lower *LCOE*.

Molten salt as a heat transfer fluid is limited by its degradation temperature limits, whereas air or solid particles can operate at higher temperatures. Alternative thermodynamic cycles can also be implemented to reach higher efficiencies. An example is the Brayton cycle which uses pressurized air or gas as its working fluid.

A Combined Cycle (CC) CSP plant can be implemented to further improve the cycle efficiency from a Brayton cycle (Buck *et al.*, 2002). Kröger (2012) presented a conceptual combined cycle central receiver CSP plant called the SUNSPOT cycle. This CC CSP plant uses a pressurized air solar receiver to pre-heat air for a downstream combustion chamber and a Brayton cycle, the Brayton cycle then rejects heat to a rock bed thermal storage medium and a Rankine cycle. Korzynietz *et al.* (2016) estimated that a thermal efficiency of more than 50 % can be achieved with a CC CSP plant, although no CC CSP plant has been implemented on a pre-commercial scale yet.

Current research in the CSP space is substantially concentrating on closed loop supercritical carbon dioxide (sCO_2) Brayton cycles. Higher thermodynamic efficiencies may be achieved when compared to an air or steam cycle. This is associated with the benefit of a relatively small compressor input power needed to compress a fluid near its critical point where it has a high density (Neises and Turchi, 2014). An additional benefit is the higher energy density associated with running the entire closed loop cycle at an elevated pressure where the fluid density is higher enabling smaller turbo-machinery to be used (Saravanamuttoo *et al.*, 2001).

It may be possible to benefit from using air as the heat transfer fluid (high- or low-pressure) along with an sCO_2 cycle by using a separate heat transfer loop. Thermal energy storage (such as rock bed thermal storage) can be incorporated in a low-pressure air heat transfer loop if a sufficient heat addition temperature of 650 °C can be reached in the sCO_2 thermodynamic cycle. A solar receiver operating directly with sCO_2 would have to withstand such a temperature as well as pressures of around 25 MPa (Neises and Turchi, 2014), this limitation indicates that an air heat transfer loop may be more practical as it permits avoiding the receiver pressure.

High- and low-pressure air receiver concepts have been proposed that are comprised of metallic or ceramic materials that withstand high temperatures. High-pressure air receivers typically contain the pressurized heat transfer fluid within a metallic structure or by means of a pressure-sealed quarts glass window. A glass window is typically required for ceramic pressurized receivers due to the brittle nature of ceramic materials. Pre-commercial metallic pressurized air receivers have demonstrated the ability to heat air up to 800 °C (Korzynietz *et al.*, 2016) with material creep limiting higher outlet temperatures. An air receiver using ceramic components sealed with a glass window has reached and sustained temperatures of 1000 °C (Doron, 2020). Although, durability and scale are limitations for glass windows (Lubkoll, 2017).

The high achievable outlet temperatures indicate that there is application potential for air receivers in an sCO_2 cycle. For the interest of a Brayton cycle or CC application, industrial small scale gas turbines (of around 500 kW) typically operate at around 900 °C and larger axial-flow turbines (of around 150 MW) can operate in the realm of 1300 °C (Saravanamuttoo *et al.*, 2001). In either case, a metallic pressurized air receiver can be used to pre-heat air for a downstream combustion chamber or a secondary receiver to reach the gas turbine inlet temperature.

It is advantageous that the receiver absorbs maximal thermal energy. The heat transfer performance of a receiver is measured using the thermal efficiency: the ratio of thermal power that is transferred into the heat transfer fluid, and the thermal power that is concentrated onto it by the heliostats. Major losses that limit the thermal efficiency of a receiver include:

- Reflective losses: concentrated irradiation intercepted by a receiver which is reflected by it's exterior surface.
- Radiative losses: radiation emitted by the receiver's exposed surface as a consequence of its elevated operating temperature.
- Convective losses: forced and natural convective heat losses occurring from external flow of air over the receiver.

Recent research has shown that metallic pressurized air receivers can reach outlet temperatures of approximately 800 °C at an efficiency of around 80 % (Lubkoll *et al.*, 2020). The performance of a solar receiver is also adversely affected by the total pressure losses that occur along the path of the working fluid. The total pressure loss is related to the power required to move a working fluid through a domain and thus should be minimized. Current metallic pressurized air receivers operate with a pressure loss of between 12 kPa and 40 kPa (Lubkoll *et al.*, 2020).

Two notable high-pressure air receiver concepts have reached an advanced Technology Readiness Level (TRL): the advanced Directly Irradiated Annular Pressurized Receiver (DIAPR) (Doron, 2020) and the SOLUGAS receiver (Korzynietz *et al.*, 2016). Both receivers are enclosed in a cavity with an opening aperture to accept concentrated irradiation. Such a design limits convective and radiative heat losses.

A DIAPR manifestation forms part of the Tulip system developed by Aora Solar. In the DIAPR manifestation shown in Figure 1.1, concentrated solar irradiation enters a pressurized chamber through a quarts glass window to heat an array of tubular pins with a large surface area called the Porcupine. The air flow enters the receiver where it first sweeps over the inside of the window to cool it, thereafter the flow turns around to be heated by the irradiated pins of the Porcupine as it proceeds towards the outlet.

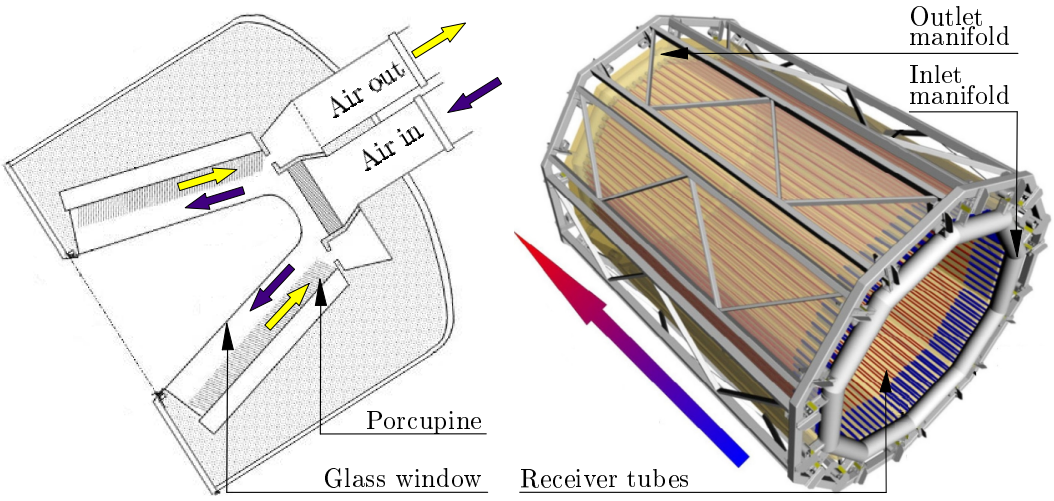

Figure 1.1: The Tulip's DIAPR receiver (left) and the SOLUGAS receiver (right) (adapted from Doron (2020) and Korzynietz *et al.* (2016)).

The large surface area of the pins ensures favourable heat transfer to the air flow. The Tulip's DIAPR receiver was designed to supply 400 kW_{th} at 4.5 bar_g and 950 °C to a gas turbine (Doron, 2020), the receiver has demonstrated on-sun operation for 1680 h. To satisfy continuous electricity generation, the Tulip system includes natural gas combustion to provide power when insufficient solar energy is available.

The SOLUGAS is a metallic receiver developed by a consortium including the German Aerospace Center (DLR) and Abengoa. In the SOLUGAS receiver, concentrated irradiation enters the cavity to heat a cylindrical array of tubes. The cylindrical design is favourable because the absorber surface area is large relative to the aperture area. A pressurized air flow enters the inlet manifold where it is distributed into the array of tubes, here it is heated as it proceeds towards the outlet manifold. The SOLUGAS receiver has been tested for more than 1000 h and has been shown to deliver 2.9 MW_{th} at 9 bar_g to pre-heat air to 801 °C for a downstream second stage ceramic receiver or a combustor for a gas turbine. A thermal efficiency and pressure loss of around 71 % and 20 kPa respectively were reported at this outlet temperature (Korzynietz *et al.*, 2016).

Low-pressure air receivers have also been investigated at a pre-commercial scale. Such a receiver has been implemented in a 200 kW_e pilot plant in Daegu, South Korea by Daesung Energy (Lee *et al.*, 2015). The receiver supplies air between 700 °C and 1000 °C to heat a solid thermal storage medium. This circulation loop is then used to generate steam for a Rankine cycle. The plant benefits by achieving an elevated cycle temperature from using air as a heat transfer fluid instead of molten salt while also incorporating thermal storage. An air receiver operating at a low pressure has the advantage of avoiding pressure-related stress.

The above mentioned air receivers make use of polar heliostat fields. Such a field contains heliostats only on one side of the receiver tower. Alternatively, a surrounding heliostat field can be used, with heliostats spanning outwards from the entire circumference of the tower. Designing a receiver for a surrounding field is favourable because such fields collect increased annual solar energy and also operate on a larger scale (Lubkoll, 2017). An alternative air receiver will now be introduced that makes use of a surrounding heliostat field.

1.2 Overview of the SCRAP concept

The Spiky Central Receiver Air Pre-Heater (SCRAP) concept is shown in Figure 1.2. The SCRAP is a metallic pressurized air receiver envisaged by Kröger (2008) at Stellenbosch University to provide pre-heated air for a Brayton cycle gas turbine of a combined cycle CSP plant. The performance characteristics of the SCRAP concept was investigated by Lubkoll *et al.* (2020).

The SCRAP receives concentrated solar irradiation on its numerous heat transfer assemblies called spikes and benefits from several inherent advantages. Firstly, the configuration of protruding spikes makes up a large heat transfer surface area to absorb concentrated solar irradiation. Secondly, convective heat losses deep within the external structure are mitigated by spiky obstructions blocking external flow.

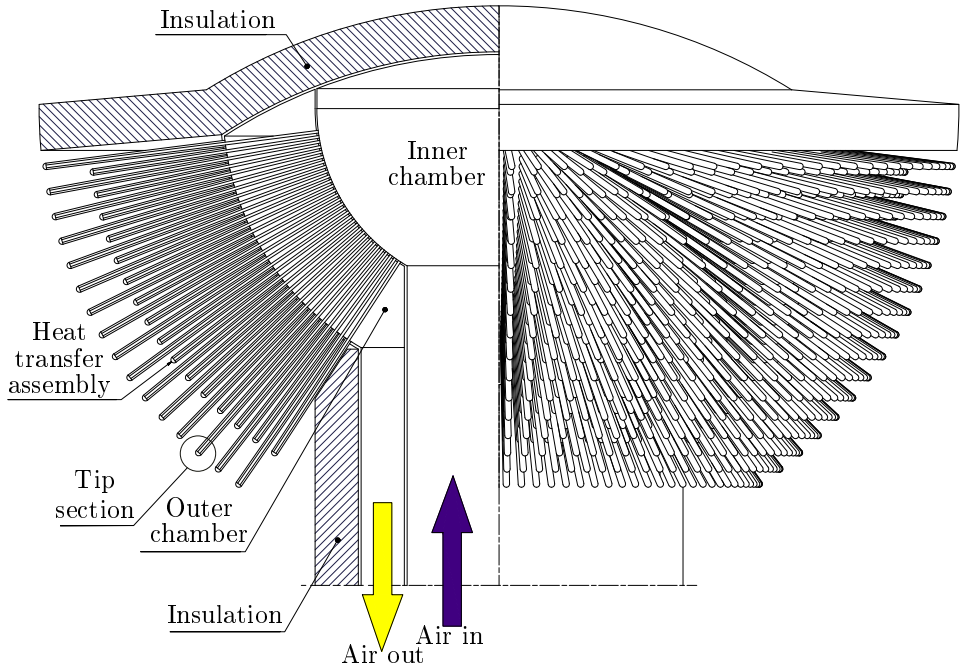

Figure 1.2: A SCRAP concept manifestation (Kröger, 2008).

Radiative and reflective heat losses within the spiky structure are also characteristically low due to relatively small view factors to ambient — emitted and reflected radiation from a spike can be absorbed by a neighbouring spike.

The internal geometry of a spike consists of an inner tube and a surrounding finned annulus that is closed off with a hemisphere at the tip section as shown in Figure 1.3. The air flow enters the inner chamber and is distributed to the spikes. Within a spike, the air flow proceeds through the inner tube towards a nozzle and a jet at the tip section. Here the flow turns around at the spike tip's hemisphere. The air is then directed through air passages between annular fins where it is further heated to reach 800 °C near the spike root before returning to the outer chamber to exit the receiver.

Adding to the benefit of a large external surface area, the internal surface area of the spike is also large due to the annular fins. During the concept's first investigation by Lubkoll (2017), rectangular air passages between the annular fins were used. The applicability of swirling fins was later explored by Grobbelaar (2019). The value of the swirled fin implementation is to to direct the air flow around the circumference of a spike for improved absorption of a non-uniform circumferential flux distribution on the outer tube while also improving the heat transfer performance.

A one-dimensional computational model was developed by Lubkoll *et al.* (2017) to estimate the capability of a characteristic spike of the SCRAP concept to absorb an expected imposed solar flux while considering radiative and natural convective thermal losses.

Figure 1.4 demonstrates the temperature and pressure characteristics of the simulated SCRAP spike — the air and surface temperatures are shown as well as the air static pressure. It is demonstrated that the spike root reaches a high temperature as the air reaches its outlet temperature here. This characteristic of the receiver is favourable because the spike root is most significantly shaded from convective and radiative heat losses.

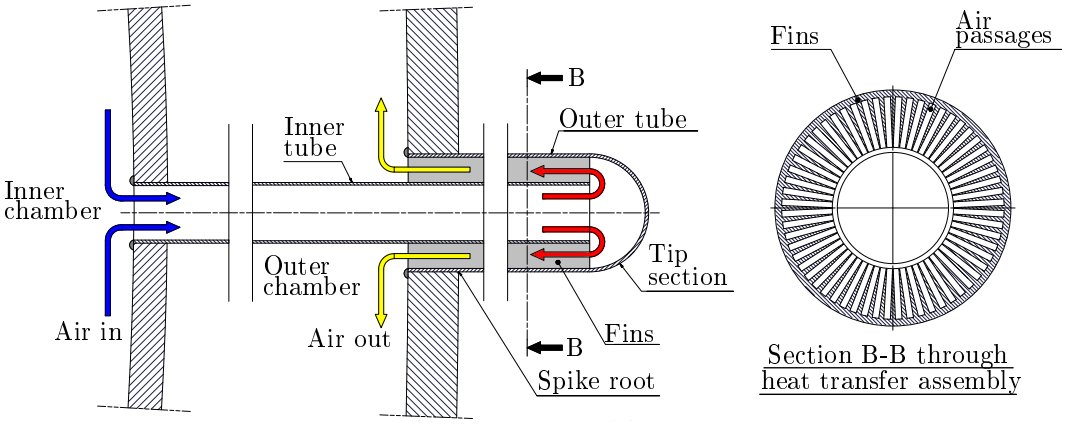

Figure 1.3: The SCRAP heat transfer assembly (spike) (Kröger, 2008).

It is also shown that the spike tip reaches a locally high temperature because the tip section receives the maximum solar irradiation from the heliostat field. This occurs because the spike tip is not shaded from incoming irradiation by other spikes. Unlike the spike root, the tip section is also most significantly exposed to radiative, reflective and convective losses. Therefore a highly effective internal heat transfer device is required to extract the heat flux imposed on the spike tip.

Figure 1.4 further illustrates that around 20 % of the receiver's heat transfer occurs in the tip section (hemisphere), this occurs through jet impingement heat transfer. Jet impingement heat transfer is an effective heat transfer mechanism. A typical jet impingement heat transfer device accelerates a fluid flow in a nozzle to a turbulent Reynolds number to emit a jet which impacts onto a surface. A stagnation region is formed at the point of impact. From here, the flow is redirected by the impingement heat transfer surface. Where a high velocity turbulent jet is redirected by a surface, a thin boundary layer is formed. Through this thin boundary layer, a large heat flux can move into a flow with a relatively low surface temperature due to a relatively large convective heat transfer coefficient.

However, even with the employment of an impinging jet, it is clear that the local peak surface temperature at the tip section shown in Figure 1.4 can still benefit from an improved heat transfer capability.

Along with its favourable heat transfer performance, an impinging jet typically undergoes a significant pressure loss because of rapid expansion (Erasmus *et al.*, 2020*b*). The graph on the right of Figure 1.4 shows that the most significant pressure loss of a SCRAP spike occurs in the tip section, also indicating a need for further improvement.

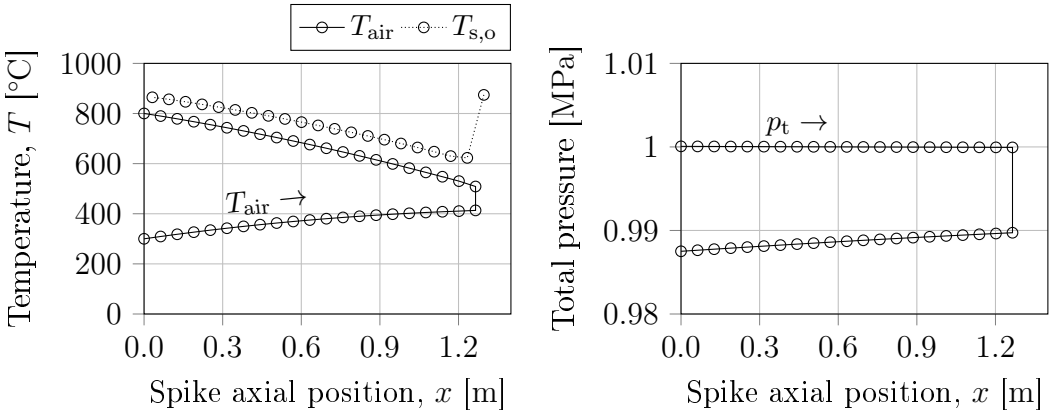

Figure 1.4: Axial distribution of a characteristic SCRAP spike's outer tube temperature, $T_{s,o}$, the air temperature, T_{air} (left) as well as the total pressure (right) (adapted from Lubkoll *et al.*, 2020).

The value proposition of developing a favourable combination of heat transfer and pressure loss (performance) characteristics for the tip section of the SCRAP concept is that the local peak temperature at the spike tip and the overall total pressure loss of a SCRAP spike may both be kept to a minimum, thereby enabling the receiver material to operate with an improved lifespan and the solarized Brayton cycle or Combined Cycle to achieve a higher overall thermodynamic efficiency. This may enable a lower $LCOE$.

Previous research involving a Computational Fluid Dynamics (CFD) analysis of the jet impingement heat transfer and pressure loss characteristics within the tip section of the SCRAP concept was conducted by McDougall (2019). He found that a reduction of the impinging jet's outlet diameter results in an increased Reynolds number and an increased heat transfer coefficient but also an increased pressure loss. To determine an appropriate trade-off between these two metrics, Mcdougall investigated their combined impact on the thermodynamic efficiency of a coupled solar-hybrid Brayton cycle and found a favourable nozzle diameter for the impinging jet. It is also possible to implement a swirled impinging jet in the tip section. A swirled jet implementation in a central receiver was explored by Quick (2020).

As part of the author's undergraduate thesis, the heat transfer and total pressure loss characteristics of impinging jet configurations were investigated experimentally and using CFD (Erasmus, 2018). The author subsequently discovered a novel concept, called the Tadpole, that is expected to improve the combination of heat transfer and pressure loss characteristics of the spike tip region when compared to an impinging jet. This research will focus on the development and investigation of the Tadpole (PCT patent application: Erasmus *et al.*, 2019).

1.3 The Tadpole concept

1.3.1 Introduction

The Tadpole originated from the observation of the total pressure contoured pathlines of the impinging jet flow domain from a Reynolds Averaged Navier Stokes (RANS) CFD simulation. Figure 1.5 qualitatively illustrates the similarities and differences between the flow domains of the impinging jet and a manifestation of the Tadpole — a key similarity is the impingement region and a key difference is that the Tadpole does not produce a free jet. It is shown that the impinging jet forms large ring vortices around the free jet. These vortices are associated with sudden expansion caused by the sudden change in flow area at the emission of the jet. Rapid expansion is not ideal because it dissipates mechanical energy through viscous heating (Erasmus *et al.*, 2020*b*).

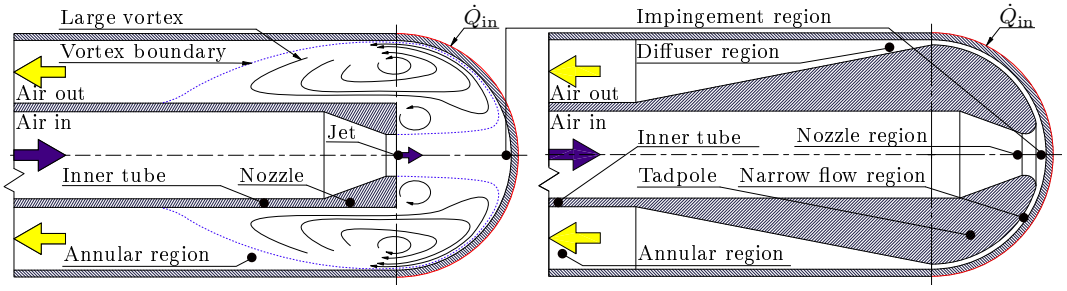

Figure 1.5: Illustrations of the jet (left) and Tadpole (right) flow domains.

The Tadpole was conceived from the idea of replacing the ring vortices with a solid device developing similarly to the vortex boundary shown on the left of Figure 1.5. The solid device in this region avoids a sudden change in flow area and thereby is expected to improve the performance characteristics of the domain. The Tadpole was also inspired by the Venturi volumetric flow meter. A Venturi flow meter contains a nozzle, a throat and a diffuser to accelerate and decelerate a flow while undergoing a relatively low pressure loss without sudden area changes encountered by an orifice plate flow meter for example.

In the Tadpole's domain, the flow enters through the inner tube to be accelerated in the nozzle region — the dynamic pressure is increased here. The flow subsequently impinges on the interior of a concave surface. The flow is then constrained to the narrow flow region and reaches a maximum Reynolds number in this region. The elevated Reynolds number ensures a thin boundary layer and a large convective heat transfer coefficient on the interior heat transfer surface. In the diffuser region, the flow is expanded to recover the previously developed dynamic pressure. The flow subsequently leaves the domain through an annular region. The Tadpole's name comes from the shape it displaces in the axisymmetric flow domain as illustrated in Figure 1.6.

The application of the Tadpole within the tip section of the SCRAP spike is shown in Figure 1.7. It is expected that the Tadpole application will improve the performance characteristics of the SCRAP concept, thereby potentially improving the lifespan of the receiver and the coupled Brayton cycle thermodynamic efficiency to facilitate the transition towards an improved *LCOE* for CSP. Additional application potential for the Tadpole will now be described.

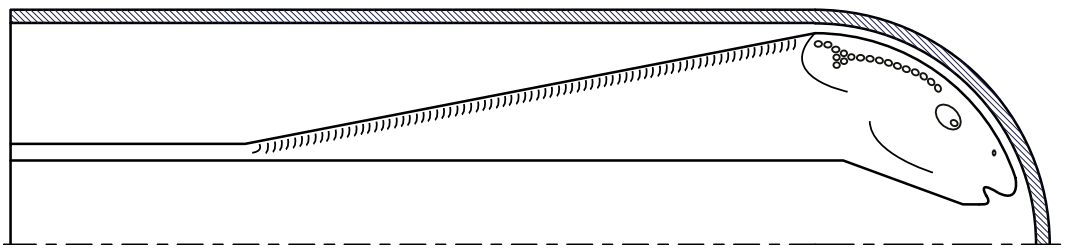

Figure 1.6: Axisymmetric illustration demonstrating the origin of the Tadpole.

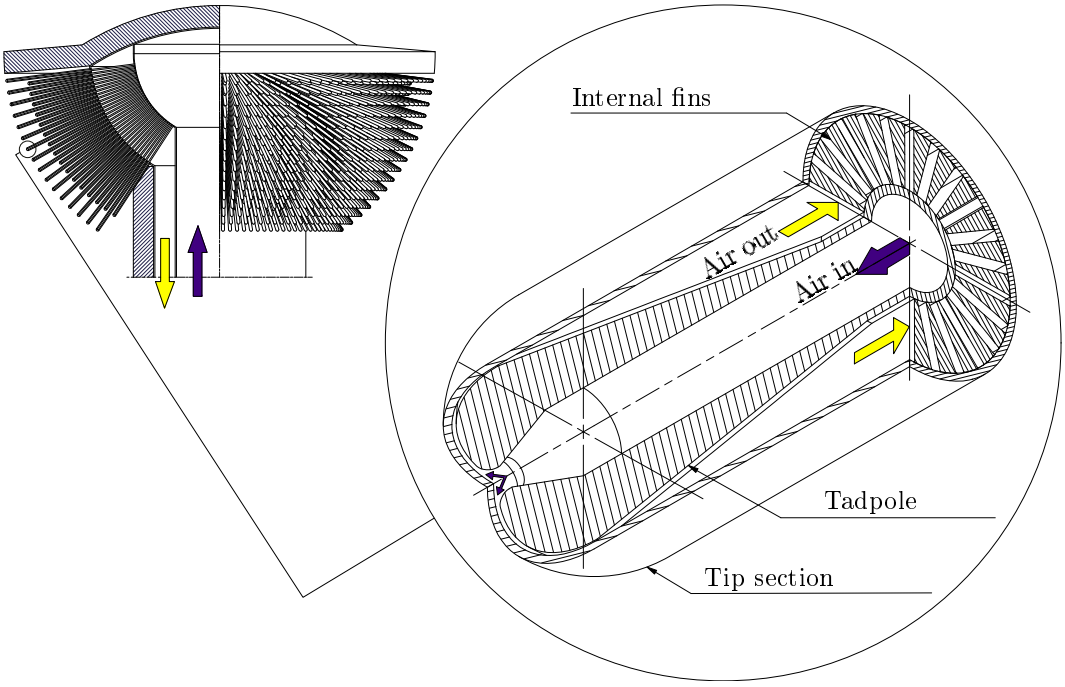

Figure 1.7: Implementation of the Tadpole within the SCRAP concept (adapted from Kröger (2008).

1.3.2 Overview of the SUNflower concept

A new solar receiver, comprised of many Tadpoles, called the SUNflower receiver is presented in Figure 1.8. It contains multiple Tadpoles within hemispherical domes, called SUNflower units, in a tessellated layout similar to a honeycomb with each unit having a hexagonal base. Favourable thermal absorption performance is expected due to the elevated impingement heat transfer coefficient within the Tadpoles. The receiver is similar to the one presented in Garbrecht *et al.* (2012) in that it makes use of impingement and hexagonal tessellation. The SUNflower surface structure resembles the densely packed seeds contained in a ripe sunflower. The base region of a hemispherical unit is substantially protected from reflective and radiative heat losses due to the base region being nearly perpendicular to the aperture. The receiver also has a secondary reflector (the petals of the SUNflower) to recover (by re-reflection) spillage — incoming solar irradiation that does not directly reach the heat transfer units. The secondary reflector is also expected to reduce convective heat losses.

The absorber structure of the SUNflower may be capable of being implemented in combination with the previously described SOLUGAS receiver as demonstrated in Figure 1.9. The SOLUGAS absorber's pipe array extends towards a flat region at it's rear section where the SUNflower can be implemented instead of a reflective material.

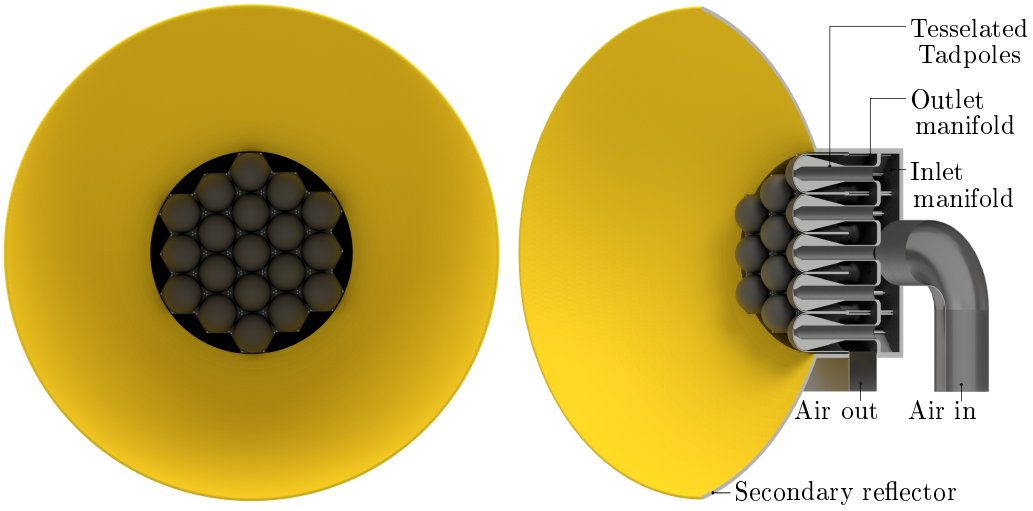

Figure 1.8: The SUNflower central receiver concept.

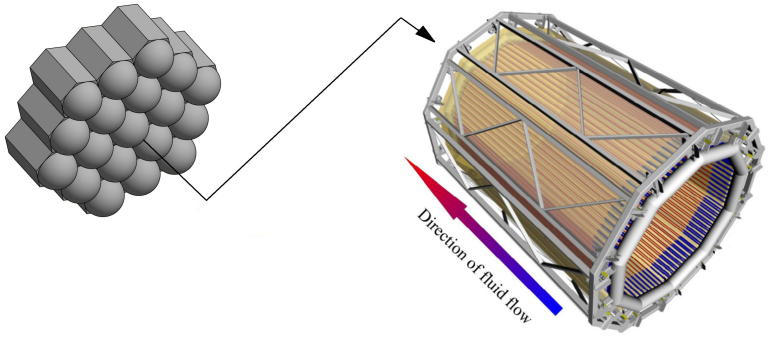

Figure 1.9: Application of the SUNflower within the SOLUGAS concept (adapted from Korzynietz *et al.* (2016)).

1.3.3 Additional Tadpole applications

The Tadpole is also envisaged in general for applications where a large heat flux is required. A specific application is a bayonet tube heat exchanger. A bayonet tube is similar to the SCRAP spike shown in Figure 1.3. Bayonet tubes have a variety of potential applications, including high-temperature hydrogen production Ma *et al.* (2011) and the steam generators of a nuclear reactor Damiani *et al.* (2013). An additional potential parabolic dish solar receiver application of the Tadpole concept is outlined in Appendix A.

The Tadpole may find further applicability in a planar domain instead of the axisymmetric domain (where Figure 1.5 is extruded instead of revolved around an axis). An example is the internal cooling of a gas turbine blade or the de-icing of an aircraft wing's leading edge.

1.4 Objectives

The focus of this thesis is to answer the research question: Is the Tadpole concept a viable heat transfer device to improve the thermal performance of concentrating solar power central receiver technologies?
To answer this question, three objectives are established:

- Describe the flow domain of the Tadpole concept and investigate its heat transfer and total pressure loss characteristics.
- Investigate the high-temperature applicability of the Tadpole within the SCRAP receiver coupled with a solarized Brayton cycle.
- Develop a reference design for the SUNflower and predict the performance characteristics of the concept.

1.5 Methodology

To develop the flow domain of the Tadpole, a kinematic model of the Tadpole will first be developed to explore the kinematic characteristics through the domain. This will enable designing Tadpoles for further development. Several Tadpole prototypes will then be designed and manufactured for experimental testing. An experimental apparatus built by Lubkoll *et al.* (2017) will be modified and a steam generator will be built and commissioned to enable testing the Tadpole.

The experimental heat transfer and pressure loss characteristics of the Tadpole prototypes will then be investigated. The previously developed impinging jet will be used as the baseline with which the performance of the Tadpole will be measured. A CFD model will be developed and validated using the experimental results to enable predicting the Tadpole's performance at an extensive variety of applications and operating conditions.

The next step is to investigate a high-temperature application of the Tadpole using the validated CFD model. The investigation will explore the potential performance improvement of the Tadpole within the SCRAP receiver from a favourable impinging jet configuration found by McDougall (2019). The investigation will extend to observing the effect of this improvement on a coupled Brayton cycle's thermodynamic efficiency.

The SUNflower will finally be explored. A suitable configuration and set of design dimensions will initially be chosen. Thereafter, the external radiative heat transfer characteristics between a heliostat field and the receiver will be explored using a convolution-projection method. Finally, the overall performance characteristics of the receiver at various operating conditions will be investigated using CFD.

Chapter 2

Literature review

This review firstly outlines the prior art of the Tadpole. Thereafter, literature on CFD turbulence modelling is reviewed to find appropriate models to compare the Tadpole with an impinging jet. Literature on diffusers will then be studied to guide the design of a suitable Tadpole diffuser. Finally, background considerations pertaining to the design of a receiver are explored, including the estimation of thermal efficiency and material considerations.

2.1 Prior art

Jet impingement flow finds various applications in CSP, aeronautical engineering and turbo-machinery.

2.1.1 Solar thermal energy

Garbrecht *et al.* (2012) describe a thermal receiver design that contains hexagonal pyramid-shaped heat transfer devices. Within the components of this device, cold fluid enters through a central pipe, impinges on the inside apex (concave surface) of a pyramid and flows out through finned channels around the pyramidal structure. Craig *et al.* (2018*a*) present an investigation for the implementation of hemispherical dome jet impingement within this receiver.

Wang *et al.* (2015) and Li (2014) present investigations where impinging jets are used within a solar cavity receiver concept. Wang and Laumert (2018) present an axial-type impinging jet cavity receiver. The axial-type is shown in Figure 2.1 and is similar to the Tadpole. Although the flow through the axial-type absorber appears to undergo substantial rapid expansion (with flow separation) through two 45° diffusers, as well as immediately downstream of the impingement region as shown in the CFD results in Wang and Laumert (2018). The design does, however, have the benefit of being manufacturable from welded sheet metal.

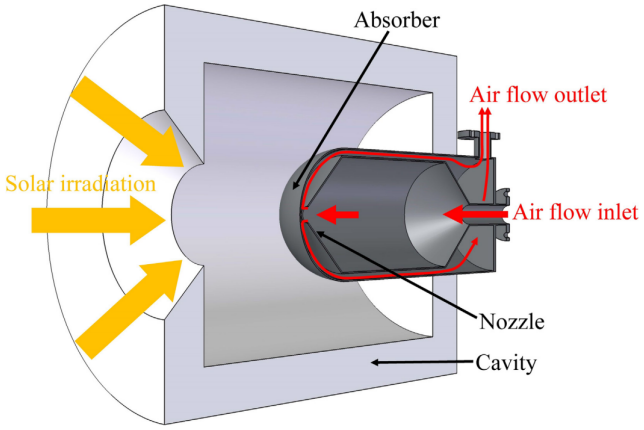

Figure 2.1: Axial-type receiver from Wang and Laumert (2018).

From a CFD analysis, Wang and Laumert (2018) found that the receiver achieved an outlet temperature of 800 °C, a peak absorber temperature of 1029 °C and a thermal efficiency of 82.8 % (without considering convective losses) at an aperture flux of 800 W/m^2. They also found that the performance of the investigated axial-type receiver performed similarly to the radial-type impinging receiver at this aperture flux but not as well at higher aperture fluxes.

It is postulated that an implementation of the Tadpole may improve the performance of the axial-type receiver shown in Figure 2.1. The potentially improved concept is described in Appendix A.

2.1.2 Aeronautical engineering and turbo-machinery

Impinging jets have been used in heat transfer devices within aircraft wings as de-icing systems. Such devices make use of hot gas bled from the engines to heat the wing's leading edge internally with an impinging jet. The jet is either a slot jet or an array of circular jets, such a concept is detailed in Kobayashi *et al.* (2000). Brand and Dowhan (2009) depict a de-icing system for the hub of an aircraft jet engine's compressor section. A jet impinges on the inside of an internal concave surface of the compressor hub, thereafter it is directed around the internal edges to heat the hub. This device rotates around the central axis with the shaft of the engine.

Gas turbines are used in the aeronautical and power industries. Gas turbine blades operate under high temperatures that are near the creep and fatigue operating limits of the materials. For this reason the turbine blades require cooling within the internal leading edge, impinging jets can be implemented here. Liu and Feng (2011) investigated the heat transfer characteristics of circular impinging jets (at various positions) within the internal leading edge of a turbine blade.

2.2 CFD turbulence modelling

2.2.1 Overview

An appropriate turbulence model is required for the CFD model of the Tadpole. It is required to model an impingement region near the nose of the Tadpole and an adverse pressure gradient in the diffuser.

Low Reynolds Number (LRN) turbulence models resolve the boundary layer computationally. The first computational node is placed well within the viscous sub-layer — around the vicinity of $y^+ \approx 1$ or less (ANSYS, 2016). LRN turbulence models are more accurate than High Reynolds Number (HRN) models but are more computationally expensive to use (Bredberg, 2000).

McDougall (2019) investigated the implementation of jet impingement heat transfer on the SCRAP concept by developing a 2D (axisymmetric) RANS CFD analysis. McDougall found that the k-ω Shear Stress Transport (SST) LRN turbulence model (Menter, 1993), with the extension of an intermittency function and a production of k limiter, correlated well with the heat transfer experimental results from Lee *et al.* (1999) and performed marginally better than the Transition SST LRN turbulence model.

Craig *et al.* (2018*a*) investigated a similar domain using an axisymmetric RANS CFD model with the Four-Equation Transition SST turbulence model (Langtry and Menter, 2009) and a 3D Large Eddy Simulation (LES) CFD model. They determined that the results from a 3D LES model as well as the axisymmetric RANS model are validated by the experimental results from Lee *et al.* (1999). Erasmus *et al.* (2020*b*) validated both the k-ω SST and the Transition SST based CFD models for a similar domain.

Literature has demonstrated that the k-ω SST and Transition SST RANS turbulence models are both suitable for application in the impingement domain. These models will be investigated further in the CFD analysis of Chapter 5. A brief overview of these models and their features now follows.

2.2.2 The k-ω SST RANS turbulence model

The k-ω SST model combines the k-ε model in the free stream region and the k-ω model near the wall with a blending function. The benefit of this model is that it is not sensitive to turbulence boundary conditions which is an issue of the k-ε model. This characteristic is important and necessary for this domain because the turbulence intensity boundary conditions represent an uncertainty (Schobeiri, 2010). The SST model is also suitable to model an adverse pressure gradient (ANSYS, 2016) — a requirement for the Tadpole.

The impingement region of an impinging jet typically contains a stagnation region and a subsequent laminar to turbulent transition (Craig *et al.*, 2018*a*). Intermittency is a turbulence metric used to quantify the fraction of time that a flow at a localized region is turbulent (as opposed to laminar) and it is used to

describe flow that is transitional (Schobeiri, 2010). An intermittency function can also be included alongside the k-ω SST model in FLUENT® to improve the modelling quality of transitional flows.

In some cases — such as near a stagnation region — the turbulence model over-approximates the turbulence kinetic energy, k. The production of k limiter mitigates this effect (McDougall, 2019).

2.2.3 The Four-Equation Transition SST RANS turbulence model

The k-ω SST model was the basis for the development of the Four-Equation Transition SST model. This model couples the former model along with functions describing intermittency and a criterion for the transition of the flow between laminar and turbulent (ANSYS, 2016). The model has been developed for domains that contain regions of transitional flow, as in the present application.

2.3 Diffusers

Diffusers cause higher total pressure losses than nozzles with similar lengths and area ratios because diffusers operate with an adverse pressure gradient. The adverse pressure gradient permits the flow to separate from the walls and cause a stall. The performance of a diffuser can be characterized by the pressure loss coefficient — from Kröger (2004). A higher loss coefficient implies a less efficient diffuser. The lost total pressure is normalized with the diffuser's inlet dynamic pressure to obtain the diffuser total pressure loss coefficient:

$$K_{\mathrm{d}} = \frac{p_{\mathrm{t}1} - p_{\mathrm{t}2}}{\frac{1}{2}\rho V_1^2}. \tag{2.1}$$

From Johnston (1953), the diffuser performance is also expressed as an efficiency in terms of the inlet and outlet static pressures and the inlet velocity. The efficiency is the ratio of the actual static pressure coefficient and the static pressure coefficient of an ideal isentropic situation as derived from the Bernoulli equation:

$$\eta_{\mathrm{d}} = \frac{p_{\mathrm{s},2} - p_{\mathrm{s},1}}{\frac{1}{2}\rho V_1^2 (1 - \frac{A1}{A2}^2)}. \tag{2.2}$$

Kröger (2004) shows that, for a round conical diffuser, the maximum achievable efficiency is around 90 % with an expansion half angle of 4.3° and a range of area ratios between 2 and 9. It is also noted that, with increasing expansion half angles, the sensitivity of the diffuser efficiency to the diffuser area ratio increases with larger area ratios resulting in lower efficiencies.

A further observation is that half angles below 4° do not result in an increase in the diffuser efficiency because of an increase in skin-friction drag. The rate of increase in drag from reducing the half angle below the optimum value is not significant in comparison to increasing the angle. This is a key finding because it demonstrates that a good diffuser can have a smaller than optimal expansion angle.

The diffuser of the Tadpole is most appropriately classified as an 'annular diffuser' with a 'constant diameter outer wall' and a 'conical centerbody' (Adkins *et al.*, 1983). The Tadpole's diffuser differs from this classification only because the outlet of the diffuser is an annulus whereas in the work of Adkins *et al.* (1983) the outlet is an open circular pipe. Such a conical annular diffuser may be used for pressure recovery downstream of a turbine or a shrouded fan. Adkins *et al.* (1983) note that, if it is assumed that the boundary layer mass flow rate is constant as it progresses through the diffuser, then 'the progressive decrease in perimeter' of the diffuser would produce a sharp increase in boundary layer thickness — larger than round conical diffusers. Conversely, in a round conical diffuser, the perimeter increases progressively.

Adkins *et al.* (1983) provide experimental results of conical annular diffusers for cone half angles of between 12.5° and 66.5°. They found that the smallest cone half angle achieved a C_p of 0.6. This was interpreted as an efficiency (η_d) of up to 91 % (for an area ratio of 1.489). This demonstrates that a similar maximum diffuser efficiency of a round conical diffuser is achievable. Adkins *et al.* (1983) observed that, for cone half angles of 22.5° or more, the recovery coefficient is less than that of sudden expansion (without a diffuser). They found that, with large cone half angles, re-circulating vortices around the diffuser become large enough to constrict the flow, so as to accelerate it further, causing a greater amount of rapid expansion downstream of the vortex than nominal sudden expansion. Johnston (1953) obtained experimental results for a diverging annular diffuser and achieved efficiencies of 85 % with a diffuser angle of 6.5°.

Vortex generators can be implemented in diffusers to enhance the diffuser efficiency by preventing flow separation (Manglik, 1987). Vortex generators may also enhance the heat transfer characteristics. A vortex generator can be placed near the inlet of the diffuser. The trailing vortices caused disrupt the downstream boundary layer in such a way as to prevent or delay separation.

Within a venturi, relatively large diffuser efficiencies can be achieved due to the upstream nozzle producing a uniform diffuser inlet velocity profile with a thin boundary layer and hence low blockage Kröger (2004). Distorted entrance velocity profiles may result in a poorer diffuser performance (Manglik, 1987). The uniformity of the exit velocity profile of the diffuser is affected by the behaviour of the diffuser: a large transitory stall causes an unsteady and non-uniform velocity profile at the diffuser outlet (Dixon, 1998).

2.4 Central receiver systems

For the Tadpole's application to a central receiver, a definition of the receiver thermal efficiency is first established. Material limitations for a pressurised air receiver are then outlined to establish a limiting operating temperature and stress for such a receiver.

2.4.1 Thermal efficiency

The thermal output of a receiver can be related to a balance of incoming irradiation and the thermal losses around the receiver (Stine and Geyer, 2001). To focus on the receiver's thermal performance, the incoming irradiation will be considered as the total irradiation reaching the receiver's surface. Hence, spillage losses (losses from incoming radiation missing the absorber) will not be included in the thermal efficiency. The output power, $\dot{Q}_{\text{out}}$, from the receiver can be related to the incoming irradiation, $\dot{I}_{\text{in}}$, and the thermal losses:

$$\dot{Q}_{\text{out}} = \dot{I}_{\text{in}} - \dot{Q}_{\text{ref}} - \dot{Q}_{\text{rad}} - \dot{Q}_{\text{conv}} - \dot{Q}_{\text{cond}}, \tag{2.3}$$

where the thermal loss: $\dot{Q}_{\text{ref}}$ is the reflected radiation from the receiver surface; $\dot{Q}_{\text{rad}}$ is the emitted radiation losses from the receiver surface and finally $\dot{Q}_{\text{conv}}$ and $\dot{Q}_{\text{cond}}$ represent the convective and conductive losses respectively. From the input irradiation and output power, the receiver's thermal efficiency can be calculated:

$$\eta_{\text{th}} = \frac{\dot{Q}_{\text{out}}}{\dot{I}_{\text{in}}}. \tag{2.4}$$

2.4.2 Suitable high-temperature materials

A pressurized air receiver is required to withstand pressure and thermally induced stress at elevated temperatures. Material creep is a deformation resulting from continuous stress loading at elevated temperatures. At elevated temperatures, the choice of metals that can withstand the allowable creep stress is limited.

Figure 2.2 demonstrates the creep strength performance of high-temperature metals. A characteristic trend of decreasing 10 000 h creep rupture stress, $\sigma_{\text{rupture,10k}}$, can be observed with increasing operating temperature, T_{sample}, for various high performing alloys. If a thermal receiver operates for an average of 12 hours per day, it will reach 10 000 hours of operation in 2.28 years. This indicates that a receiver should operate below its rupture stress.

Swindeman and Marriott (1994) shows that, according to the the American society of mechanical engineers (ASME) boiler and pressure vessel (BPV) code, the allowable creep stress of high performance Inconel alloys is around 10 MPa at an operating temperature of 950 °C.

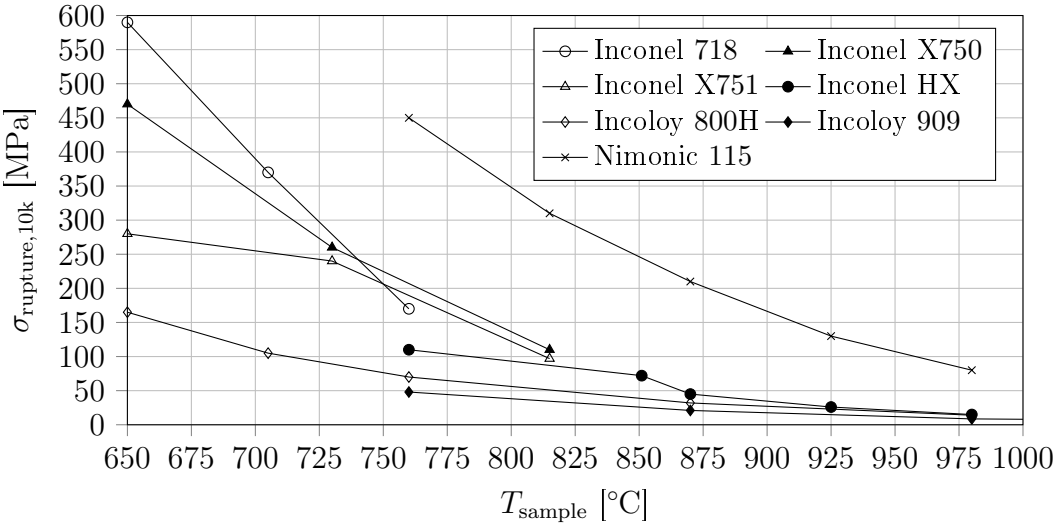

Figure 2.2: Comparison of the 10 000 h rupture strengths of high-performing, high-temperature metals (Data from (SMC, 2019)).

2.5 Conclusion

Several prior concepts in the solar energy and turbo-machinery fields have been described to provide a perspective on the application potential of the Tadpole. Literature has demonstrated that the k-ω SST and Transition SST RANS turbulence models are both suitable for application in the impingement domain and will be investigated further in the CFD analysis. Insight from diffuser literature shows that a favourable Tadpole diffuser would develop with a half angle of 12.5° or less.

The formulation of a central receiver thermal efficiency has been described and a temperature and pressure limit of a pressurised air receiver has been established.

Chapter 3

Development of a kinematic flow model

This chapter establishes an understanding of the Tadpole's flow domain. A kinematic model is developed to design Tadpoles. A geometric model is first detailed to depict the area and hydraulic diameter at discrete points within the domain and then the kinematic flow model is detailed.

3.1 Geometric model

The Tadpole's reference flow domain is established in terms of several variables in Figure 3.1, these variables will be referenced and explored in subsequent chapters through various prototypes.

It is of interest to describe the flow area — the sectional area perpendicular to the mean flow direction — as a function of an approximated 1D mean pathline throughout the domain. The mean pathline of the axisymmetric domain is drawn in Figure 3.2. To capture the area development, 18 node points are defined, of which 12 are within the narrow flow region[1].

The flow area at the inner tube and annular nodes are calculated using circle geometry. In the narrow flow region, the flow area can be characterized in terms of a lateral right cone frustum area. This is now detailed for a concentric Tadpole, where the Tadpole hemisphere and the heat transfer surface centre points are the same. The conical frustum equation described by Boljanovic (2007) has been adapted to describe this flow area (A_{F}) explicitly in terms of the Tadpole's radius (r_{t}), the interior surface radius (r_{i}) and the angular progression around the hemisphere (from $\alpha = \alpha_1$ to $\alpha = 90°$). Equation (3.1) is valid for any node in the narrow flow region between $\alpha_1 \leq \alpha \leq 90°$:

$$A_{\mathrm{F}}(\alpha) = \pi(r_{\mathrm{i}}^2 - r_{\mathrm{t}}^2)\sin\alpha. \tag{3.1}$$

[1]Between the Tadpole surface and the interior heat transfer surface.

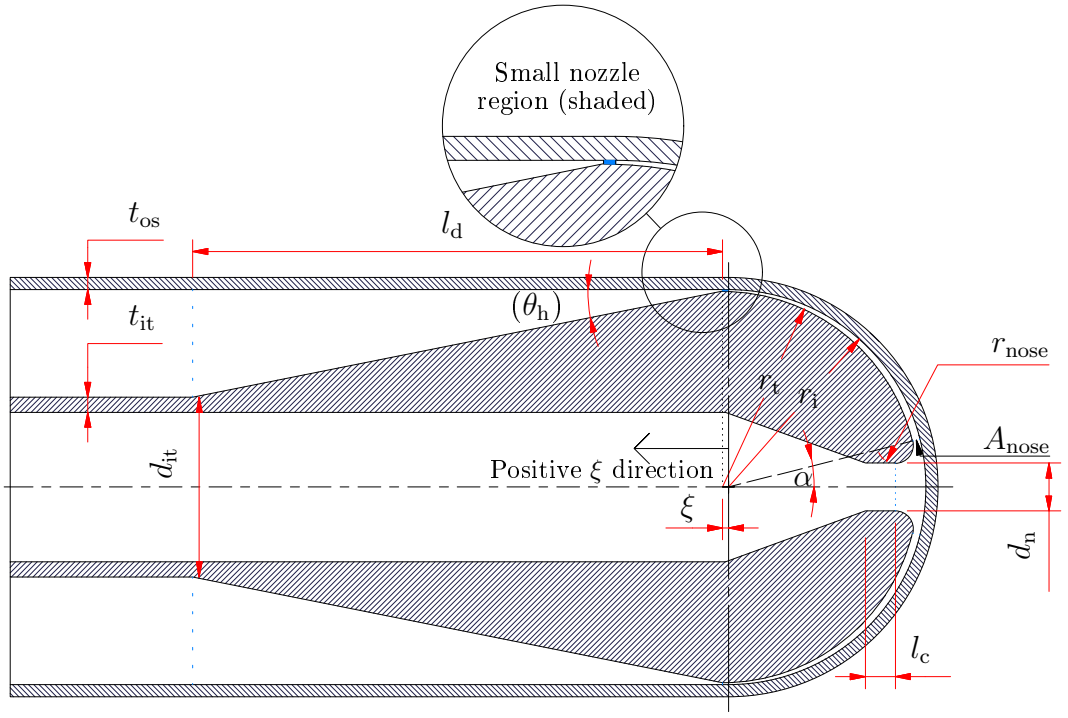

Figure 3.1: Physical dimensions of a generic Tadpole — demonstrated in a positive ξ position.

It is necessary to calculate the angle, α_1, at the start of the narrow flow area (depicted at A_{nose} in Figure 3.1). It will be shown that this region is particularly important and will be referred to as the nose of the Tadpole. Tangent constraints at the Tadpole's nose permit α_1 to be calculated explicitly using trigonometry:

$$\alpha_1 = \sin^{-1} \frac{d_n/2 + r_{nose}}{r_t - r_{nose}}. \tag{3.2}$$

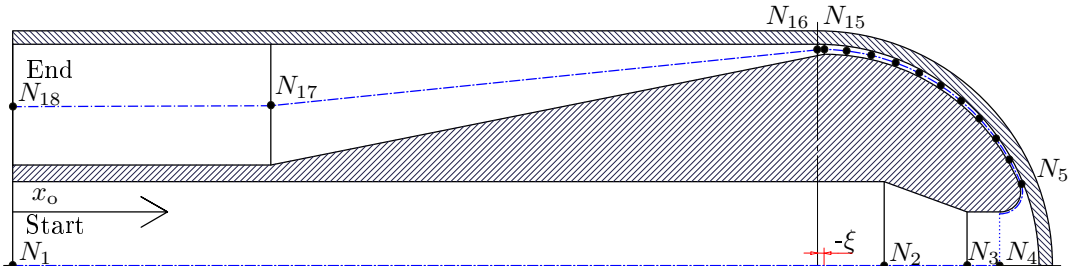

Figure 3.2: Mean pathline (dash-dotted) and 1D computational nodes (points) of the (axisymmetric) flow domain — demonstrated in a negative ξ position.

With the introduction of a non-zero axial position (ξ) in the Tadpole's domain, the Tadpole's surface and the inner heat transfer surface become non-concentric and the previous area calculation becomes invalid. If ξ is positive, the flow area equation (as a function of α) has been derived implicitly and must be solved iteratively. If ξ is negative (or zero), an explicit solution has been derived. Appendix B details the non-concentric frustum area derivations.

Further complexity caused by a non-zero ξ is that a small nozzle ($\xi > 0$) or a small diffuser ($\xi < 0$) is formed near the end of the narrow flow region at $\alpha \approx 90°$. This is because the start of the Tadpole's inwardly sloping region (the diffuser) does not coincide with the start of the outer-shell cylinder. Figure 3.1 shows the small nozzle and Figure 3.2 shows the small diffuser. Two nodes (N_{15} and N_{16}) are therefore positioned on either side of these regions in each case. The area at N_{15} (for both $\xi > 0$ or $\xi < 0$) is calculated using the procedure detailed in Appendix B. At N_{16}, the sectional flow area is approximated as that of an annulus; in the case of $\xi < 0$ the slightly reduced inner annular radius at N_{16} is interpolated using r_t and ξ.

The mean flow area is assumed to vary linearly around the anomalous stagnation region (between N_4 and N_5) because the real flow area cannot be described analytically in this region and a localized high-pressure zone is caused by impingement resulting in an irregular velocity profile here.

The equations describing the narrow flow region area have been verified geometrically using Autodesk Inventor®. The implicit flow area calculation procedure is executed iteratively using Microsoft Excel®with Visual Basic®.

The development of the flow area for a Tadpole with a 16 mm nozzle diameter is demonstrated in Figure 3.3). The flow area is described in terms of a characteristic area radius, $\sqrt{A_F/\pi}$. The area radius is of such a form that, for the round circular nozzle region, it is equal to the radius of a conventional circular round nozzle. This enables a relative visual comparison of the area development with the axisymmetric circular domain of the Venturi.

The hydraulic diameter development is also shown in Figure 3.3. The hydraulic diameter at any node is: $d_{hyd} = 4A_F/P_w$ (Çengel and Cymbala, 2014), where P_w is the wetted perimeter enclosing the flow area. Within the narrow flow region, the wetted perimeter is represented by the addition of two relatively large circumferences (projected from hemispheres).

If the flow area were round circular throughout (as in a Venturi) instead of an annulus or a frustum, there would be no variation between the hydraulic diameter and area developments in Figure 3.3. However, the flow within the narrow flow region and the annular diffuser follows a significantly larger P_w (and hence a reduced d_{hyd}) than in a round circular domain. The reduced hydraulic diameter has the effect of linearly reducing the Reynolds number according to the relation: $Re = \rho V d_{hyd}/\mu$ (Çengel and Cymbala, 2014). This suggests that the flow through the domain may remain laminar at higher flow velocities compared to the round circular domain.

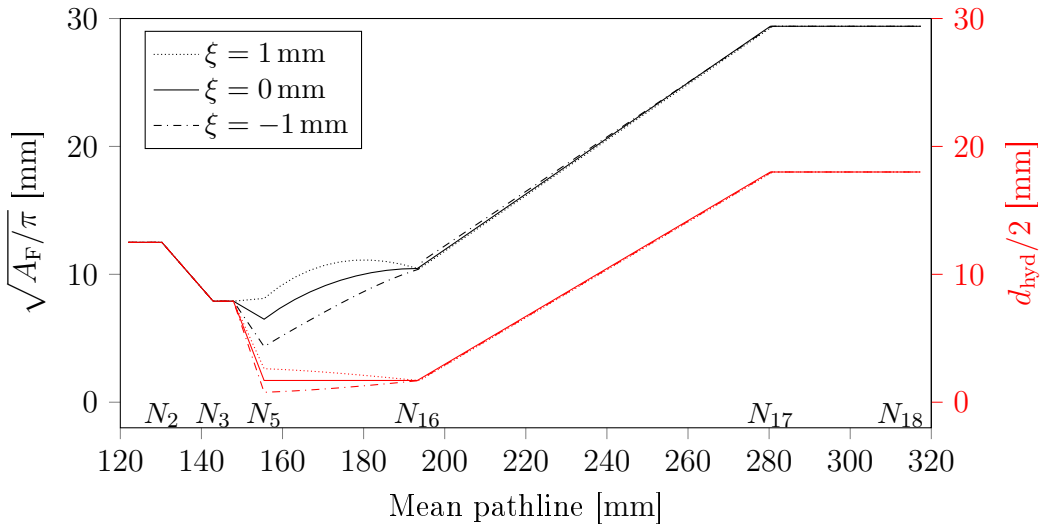

Figure 3.3: Flow area characteristic radius (black) and hydraulic diameter (red) development with the mean (1D) pathline (pathline node locations are depicted in Figure 3.2).

The flow area sensitivity to a change in axial position (ξ) is depicted. It can firstly be observed that the area development can be manipulated by varying ξ; and secondly, that the minimum flow area characteristically occurs at the Tadpole's nose (α_1) and is particularly sensitive to ξ. It can lastly be seen that the narrow flow region can operate as a diffuser and a nozzle.

3.2 Kinematic flow model

3.2.1 Overview

An analytical flow model is presented to observe the kinematic behaviour around the Tadpole. The model primarily makes use of mass conservation to determine the velocity at each node. Although, because high velocities are considered ($N_\mathrm{Mach} > 0.3$), compressibility is also considered. The flow is solved with the isentropic flow simplifying assumption, therefore the total pressure is conserved through the domain.

An iterative calculation procedure is followed. The velocity at each node is initialized using incompressible flow mass conservation (with a constant density as at N_1 all around the domain). This result enables the calculation of the dynamic pressure, p_dyn at each node. The new static pressure at each node, p_s, can then be calculated with $p_\mathrm{s} = p_\mathrm{t} - p_\mathrm{dyn}$. The new static pressure is used to determine the new density from the ideal gas law. thereafter, the new velocity is calculated to complete an iteration. The velocity converges to a normalized residual of 10^{-12} in approximately 8 iterations.

3.2.2 Assumptions

The first simplifying assumption is conserved total pressure. This assumption is expected to cause an average Mach number error of around 1.7 % based on the expected total pressure loss from an initial CFD model. Thus, for an estimation of the kinematic characteristics, this is negligible.

The second simplifying assumption is excluded thermal effects, a constant temperature is assumed for the domain. Heat addition and the Joule-Thomson effect of expansion cooling are therefore neglected. The model thirdly does not consider boundary layer effects (like the Euler-flow assumption). It is expected that, with the anticipated high velocity turbulent flow, the surfaces will not develop a significant boundary layer. The uncertainty of the final two assumptions are not possible to predict and will therefore be assessed through verification.

3.2.3 Verification

A CFD model will be developed in Chapter 5 which does not make the above-mentioned simplifying assumptions. In Appendix C the kinematic model is verified with the CFD model to asses whether the model's results are reliable. It is demonstrated that the kinematic model can satisfactorily reproduce the peak Mach number as well as the Mach number development of the CFD model.

3.2.4 Model demonstration

A demonstration of the flow model was executed at a typical mass flow rate of 0.0166 kg/s and an outlet gauge pressure of 55 kPa. The development of the Mach and Reynolds numbers are presented in Figure 3.4. It can be observed that the Mach number is sensitive to ξ with the peak Mach number occurring at the Tadpole's nose. For $\xi = -1$, the Mach number decreases in a small increment around the small diffuser; whereas a less noticeable small nozzle is formed at the same position for $\xi = 1$.

It is interesting to observe in Figure 3.4 that the Reynolds number is not at all sensitive to ξ in this domain. This is explained by the following derivation of the Reynolds number in terms of the mass flow rate and perimeter (as a function of the hydraulic diameter reference length): $Re = 4\dot{m}/(\mu P_{\mathrm{w}})$. It is shown that the only influential geometric variable is the wetted perimeter which does not change with a change in ξ because the cumulative circumference of the flow area frustum remains nearly the same.

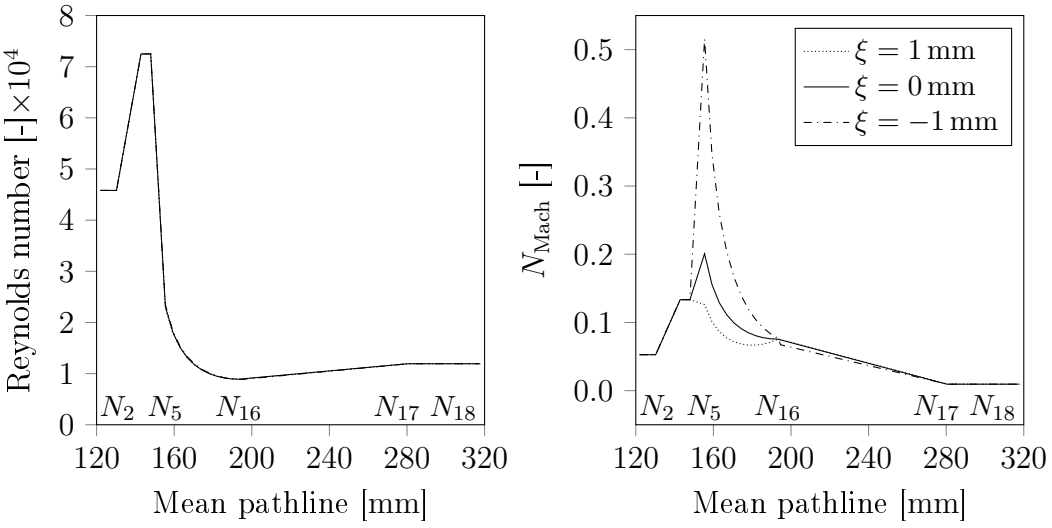

Figure 3.4: Reynolds number (left) and the Mach number (right) development with the mean pathline (pathline node locations are depicted in Figure 3.2).

3.3 Conclusion

A geometric and kinematic model has been developed for an established reference Tadpole flow domain. The typical kinematic behaviour of the Tadpole has been demonstrated. The model permits rapidly choosing various combinations of design variables of Tadpole prototypes to achieve a certain kinematic profile through the domain. The main limitations of the model is that it is 1D and it assumes a constant temperature throughout the domain. In the proceeding chapter, the model will aid designing various experimental prototypes.

Chapter 4

Experimental investigation

This chapter first describes the experimental apparatus and the development of the Tadpole prototypes. The testing procedure and the processing of results are then detailed. An investigation into error and uncertainty as well as safety considerations follow. Finally, the heat transfer and pressure loss experimental results are revealed. Parts of this chapter has been published in Erasmus *et al.* (2020*b*) and Erasmus *et al.* (2020*a*), and is pending journal submission in Erasmus *et al.* (2021*a*).

4.1 Apparatus overview

The experimental apparatus used in this work was built by Lubkoll *et al.* (2017) and was modified to investigate jet impingement heat transfer in Erasmus *et al.* (2020*b*). The setup was further developed to investigate the heat transfer and pressure loss characteristics of Tadpole prototypes. The working fluid of the setup is pressurized air supplied by a 10 bar air-supply system.

Heat is supplied to the air stream using a steam bath with steam condensation at atmospheric pressure (nominally 100 °C). In Figure 4.1, the hot steam bath assembly is shown transferring heat to the insulated test section. The entire test section except the steam bath is insulated from ambient with fibreglass wool. This ensures that the path of the air flow — between where its inlet and outlet temperatures are measured — is isolated from ambient. A steam generator was also built and commissioned along with this project to supply 6 kW of steam to the steam bath of the apparatus. An overview of the steam generator is given in Appendix D.

Figure 4.2 presents the test section and Figure 4.3 shows a sectioned view of the test section. Air enters the section at the inlet pipe to proceed through the nozzle assembly towards the Tadpole or an impinging jet configuration. The nozzle assembly communicates with the exhaust section with an o-ring. A section containing annular fins aligns the nozzle assembly with the annular axis. A hemispherical dome interfaces with the steam bath.

Figure 4.1: The insulated setup (left) with an infrared image (right) demonstrating heat addition during operation.

Here, heat addition to the air occurs through and around the hemispherical dome where steam condenses. After being heated, the air flows through the finned section to reach the outlet section and finally the exhaust section.

The exhaust section contains a silencer that chokes the flow, thereby pressurizing the upstream components. The silencer delays the onset of a sonic condition in the upstream domain. This facilitates investigating small upstream flow areas (as is characteristically found at the Tadpole's nose) under subsonic and transonic conditions. Moreover, if the silencer was not installed, the investigated impinging jets and Tadpoles would reach a sonic condition at a relatively low mass flow rate.

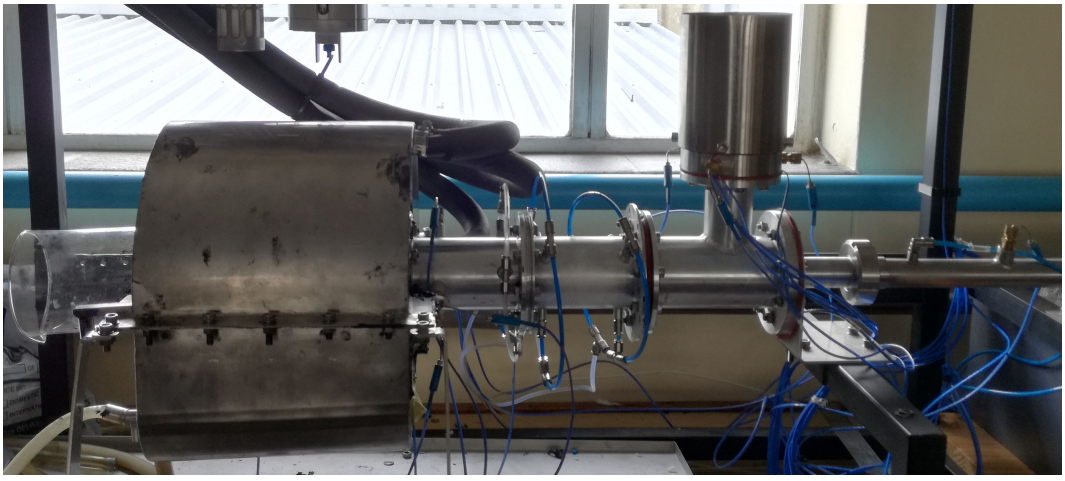

Figure 4.2: Uninsulated experimental test section.

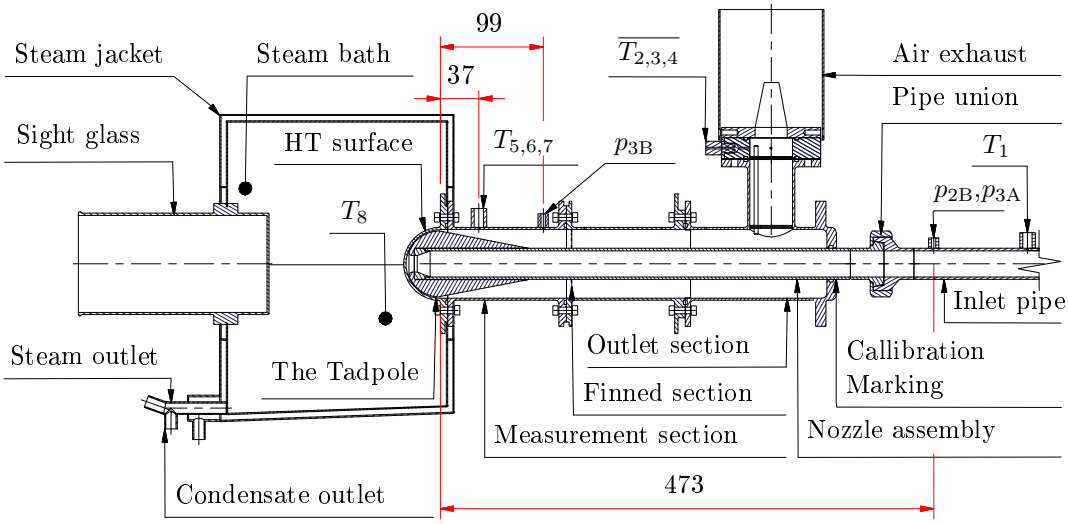

Figure 4.3: Sectioned view of the experimental test section (dimensions in mm).

The heat transfer region of the test section is shown in Figure 4.4. A flange around the hemispherical dome interfaces with the steam bath and is sealed using a high-temperature silicone adhesive. Heat travels through conduction from the exterior HT surface towards the interior HT surface and through the flange before it reaches the convection domain. This combined interaction of conductive and convective heat transfer is termed conjugate heat transfer. It will be shown in Section 5.4.3 that the region where most of the heat is transferred into the convection domain is through the dome and the neighbouring flange.

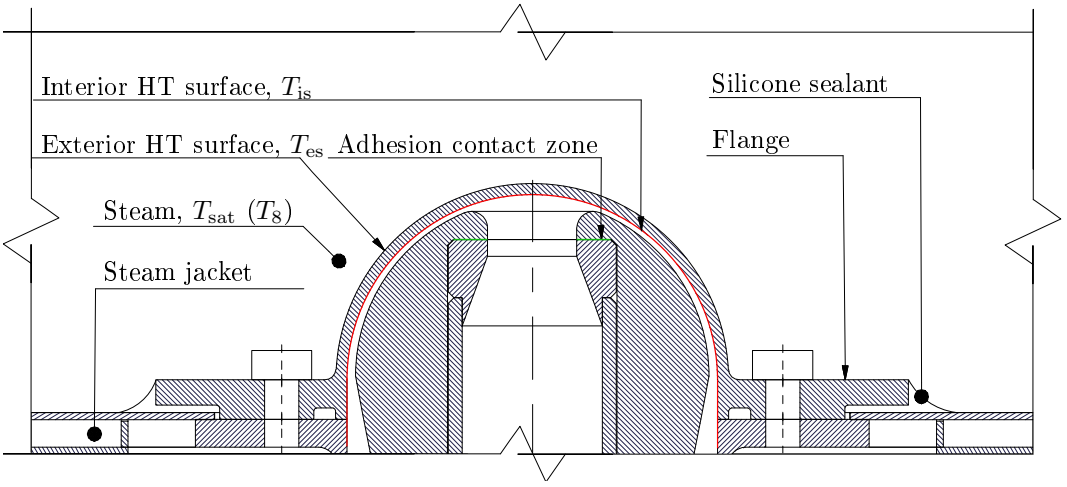

Figure 4.4: Sectioned view of heat transfer region of the test section.

For this reason, the conventional area for estimating the average heat flux represents a combination of the hemispherical area and a part of the flange (denoted by the red line in Figure 4.4)[1].

The heat transfer characteristics of an impinging jet or a Tadpole are determined using a combination of T-type thermocouples. The air inlet temperature (T_1) is measured at the inlet pipe and the outlet temperature is measured after the air flow temperature has mixed from the average of three thermocouples: $\overline{T_{2,3,4}}$. The heat addition to the air stream is determined from the temperature difference of $\overline{T_{2,3,4}}$ and T_1 through energy conservation:

$$\dot{Q}_{\text{air}} = \dot{m}_{\text{air}} c_{\text{p}} (\overline{T_{2,3,4}} - T_1). \tag{4.1}$$

The air heat addition rate is used to calculate the area-weighted-average (overall) heat transfer coefficient over the interior heat transfer surface. This is determined following the same convention as an impinging jet (VDI, 2010):

$$h_{\text{is}} = \frac{\dot{Q}_{\text{air}}}{A_{\text{is}}(T_{\text{is}} - T_1)}, \tag{4.2}$$

where A_{is} represents the area of the interior heat transfer surface — illustrated as the red line in Figure 4.4. The Nusselt number is then determined (also with the impinging jet convection):

$$Nu_{\text{is}} = \frac{h_{\text{is}} d_{\text{n}}}{k}, \tag{4.3}$$

where d_{n} is the diameter of the nozzle region of the Tadpole prototype or the nozzle diameter of an impinging jet. It must be noted that T_{is} is not measured with a thermocouple because thermocouples in the hemisphere will interfere with the heat transfer characteristics. Instead the temperature is obtained using the measured steam saturation temperature (T_8), the known $\dot{Q}_{\text{air}}$ and the temperature drop caused by condensation and conduction over the hemispherical dome. The steam heat transfer coefficient is therefore required to approximate the average temperature of the exterior heat transfer surface (T_{es}) in terms of the saturation temperature (T_8). The empirical steam condensation heat transfer coefficient from Çengel and Ghajar (2011) — is employed for a spherical surface of diameter d_{sph}:

$$h_{\text{cond}} = \left(\frac{0.815 g \rho_{\text{l}} (\rho_{\text{l}} - \rho_{\text{v}}) [h_{\text{fg}} + 0.68 c_{\text{pl}} (T_8 - T_{\text{es}})] {k_{\text{l}}}^3}{\mu_{\text{l}} (T_8 - T_{\text{es}}) d_{\text{sph}}} \right)^{1/4}. \tag{4.4}$$

The interior surface temperature (T_{is}) can then be determined in terms of T_{es} using 1D conduction through the thickness of the hemispherical dome. The uncertainty of the exterior surface temperature estimation due to the condensation heat transfer coefficient will be analysed later in Section 4.4.3.

[1] An insignificant extraneous heat transfer rate is also expected by cross-flow between the nozzle assembly and annular region, this will be considered in Section 4.4.3.

The test section components, with the exception of the Tadpole prototypes and the steam bath, were manufactured from aluminium. The steam bath was manufactured from stainless steel. Figure 4.4 shows that an experimental Tadpole configuration is made of two components: a nozzle assembly and an attached bulbous ABS plastic part joined by an adhesion contact zone (denoted by green lines). The main part of the Tadpole is manufactured from plastic because heat transfer through the Tadpole is not necessarily desired – this will later be investigated with the CFD model in Section 5.4.1. The values and origins of the air, steam and material properties used in processing the results are given in Appendix E.

Figure 4.5 illustrates the system diagram of the apparatus. Here, p represents a pressure measurement from a differential pressure transducer (Freescale MPX2050DP), T represents a thermocouple's temperature and G is the gauge pressure sensor's measurement (measured with a Firstrate FST800-10B sensor). Also shown in Figure 4.5 are the air supply, control valve and flow measurement device upstream from the test section.

The pressurized air enters the system at the air supply. The air mass flow rate is controlled by varying the static pressure using the control valve. The orifice plate inlet temperature (T_0) and gauge static pressure (G) are required to determine the density the orifice plate through the ideal gas law: $\rho = (G + p_{\text{atm}})/(RT_0)$. The mass flow rate is obtained iteratively using $\dot{m}_{\text{air}} = CE\varepsilon\frac{\pi}{4}d^2\sqrt{2\rho p_1}$, where p_1 is the orifice plate differential pressure; d is the orifice diameter; ρ is the density upstream of the orifice plate and the remaining empirical variables: C (coefficient of discharge), E (velocity approach factor) and ε (expansion factor) are calculated using the method detailed in Lubkoll (2017).

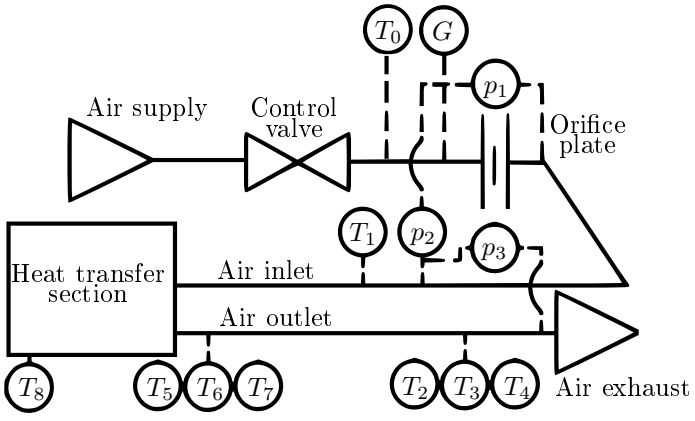

Figure 4.5: System diagram of the experimental apparatus.

The air inlet gauge static pressure of the test section is determined using p_2. The differential pressure, p_2, is measured between G and p_{3A} (shown previously in Figure 4.3) and is used to determine the density with the ideal gas law at the air inlet of the test section. The differential static pressure measurement over the test section, $p_3 = p_{3A} - p_{3B}$, is firstly used to determine the static pressure and density at the outlet of the test section. Secondly, it is used to derive the total pressure at the outlet and hence determine the total pressure loss through either the Tadpole or impinging jet flow domains. To determine the total pressure at the inlet or at the outlet: the conservation of mass is used with the known density and flow area to calculate the velocity: $V = \dot{m}/(\rho A)$. From the velocity, the dynamic pressure is calculated: $p_{\text{dyn}} = 1/2\rho V^2$. Finally the total pressure is determined: $p_{\text{t}} = p_{\text{s}} + p_{\text{dyn}}$.

There are three pressure taps positioned at the same axial position downstream of the diffuser at 120° intervals around the annular axis and are connected to measure an averaged pressure reading (p_{3B}) around the axis.

4.2 Overview of experimental prototypes

4.2.1 Designing the experimental prototypes

Overview

The prototypes will be designed to experimentally investigate the behaviour of the Tadpole's flow domain through a wide variety of characteristic variables — the physical dimensions of the flow domain (shown previously in Figure 3.1) and the Reynolds number. The combination of these variables are too numerous to investigate individually, therefore a prototype-based experimental approach will be followed. Several prototypes will be developed, which each representing a combination of key dimensions.

An initial CFD sensitivity analysis was executed to explore suitable dimensions. It was found that, if the flow velocity reaches a maximum at the Tadpole's nose, separation is avoided near the stagnation region — this is intuitive because with this constraint, a positive pressure gradient is maintained before the Tadpole's nose. This was identified to produce a low total pressure loss in this region. A peak velocity at the Tadpole's nose is therefore the primary design objective.

The kinematic model from Chapter 3 predicts the location of the peak velocity in the domain for any combination of dimensions in the subsonic realm and thus enables satisfying the primary objective. The secondary objective is to produce a gradual velocity development through the domain to avoid sudden expansion or contraction of the flow.

In Erasmus *et al.* (2020*b*), impinging jet nozzle assemblies including nozzle diameters of: 16 mm and 12 mm were tested to explore a low and high nozzle Reynolds number. The first Tadpole dimensional constraint is for the nozzle region of two Tadpoles to be comparable to these two jets with a similar nozzle-region diameter. These nozzle assemblies physically make up part of the Tadpole prototypes as shown previously in Figure 4.4. An 8 mm (nozzle region) Tadpole was also created to explore even higher velocities — this makes up three different Tadpole prototypes. The imposed constraints are that the Tadpole's radius (r_t), its nose radius (r_nose) and its axial position (ξ) be selected in order to satisfy the above-mentioned primary and secondary objectives.

The nozzle region's convergence angle was retained at 20° as in Erasmus *et al.* (2020*b*) because it was found to have a small loss coefficient (Çengel and Cymbala, 2014) and it enables comparability to the previous impinging jets. The diffuser half angles, θ_h, were constrained between 11° and 13° for all cases. The apparatus did not permit longer diffusers than these — longer diffusers (around 7°) would have been chosen if permitted. This is because in Section 2.3 it was found that a conservatively small half angle works favourably.

Table 4.1 and Table 4.2 describes the dimensions required to manufacture and configure the experimental prototypes and flow domains.

Table 4.1: Dimensions applicable to all Tadpole prototypes (dimensions in mm as depicted in Figure 3.1).

r_i	t_os	d_it	t_it	l_c
33	2	30	2	5

Table 4.2: Dimensions of the experimental Tadpole prototype configurations (dimensions depicted in Figure 3.1).

Parameter		16-A	16-B	12-A,ss	12-B	12-C,ts	8-A,ss	8-B
d_n	[mm]	15.8	15.8	11.7	11.7	11.7	7.7	7.7
r_nose	[mm]	3	3	2.5	2.5	2.5	2	2
r_t	[mm]	31.3	31.3	32	32	32	32.5	32.5
l_d	[mm]	85	85	90	90	90	95	95
ξ_low	[mm]	−1.09	0.263	−0.743	0.157	−0.293	0.0902	1.09
ξ_high	[mm]	−0.587	0.663	−0.643	1.16	0.357	0.0902	1.29

Tadpole naming convention

The naming convention for the prototypes and configurations in Table 4.2 are intuitively described using the critical variables. Here, a prototype refers to a specific physical Tadpole and a configuration refers to a testing position of the prototype. Each physical prototype is named with a number according to its nozzle diameter and the configuration of each prototype is named according to its relative axial position (ξ), such as 8-A or 8-B for example. With A depicting the prototype configuration where the nose is nearest to the interior heat transfer surface (lesser ξ) and B depicting the farthest (greater ξ). There is also a special case configuration, 12-C, with an axial position between the 12-A and 12-B configurations.

Supersonic exploration

The area development of the Tadpole's flow domain characteristically converges before diverging as shown previously in Figure 3.3. This means that if a large enough pressure difference over the domain is applied, $N_{\text{Mach}} = 1$ will be reached at the Tadpole's nose, then the diverging flow area region downstream of the nose will further accelerate the flow into the supersonic realm. For the coincidental inherent capability of the Tadpole to reach supersonic speeds, the heat transfer and pressure loss characteristics in this realm will also be explored experimentally. The prototype configurations in Table 4.2 that ventured in the transonic and supersonic realms are denoted with the abbreviations: ts and ss.

Managing a changing geometry with mass flow rate

During experimental operation, it was found that the Tadpole generates thrust in the axial direction. The thrust is generated by the pressure and shear stresses acting on the exposed surfaces of the Tadpole (from the nozzle region to the diffuser). The thrust causes the relative axial distance between the Tadpole and the interior heat transfer surface centre points (ξ) to increase slightly with an increase in air mass flow rate. Moreover, the apparatus elastically deforms during a test in relation to mass flow rate.

To address this characteristic, the axial positions were measured at a low mass flow rate (to determine ξ_{low}) and at a high mass flow rate (to determine ξ_{high}) of a varying mass flow rate test as shown in Table 4.2. These ξ values were linearly interpolated for other data points based on the mass flow rate to estimate the geometry of the flow domain. For the CFD model developed in the following chapter, the interpolated ξ values will be used for the mesh of each simulated mass flow rate (shown in Appendix G).

4.2.2 Design improvements through prototyping

Due to the prototyping approach followed, minor improvements were made during the experimental exploration. The 16 mm prototype was first tested. Thereafter, two minor design improvements were made for the subsequent 12 mm and 8 mm prototypes.

The first improvement was the diffuser's inlet geometry. The Tadpole's transition from the narrow flow region to the diffuser may be a sharp transition or a transitional arc so as to create two interfacing tangents as demonstrated on the plastic parts of two prototypes in Figure 4.6. A sharp transition was chosen for the 16 mm prototype and a tangent transition (curved entrance diffuser) was subsequently chosen for the 12 mm and the 8 mm configurations. The curved entrance diffuser affects a more gradual initial expansion rate of the flow and a larger rate nearer to its end.

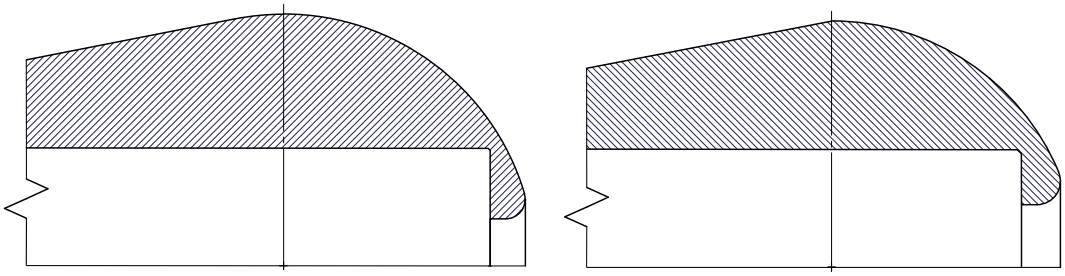

Figure 4.6: Tangent diffuser transition on the 12 mm prototype (left) and the sharp transition on the 16 mm prototype (right).

A comparative CFD investigation was conducted between the curved entrance and sharp diffuser transitions. It was found that, for the same diffuser length (l_d) on the 16-B configuration, the curved entrance diffuser manifestation experiences 3.67 % lower total pressure losses[2]. The CFD model also depicts an exponential decrease in Mach number through the diffuser (in Appendix C, Figure C.1). This indicates that the diffuser's entrance geometry is more important than its outlet in the process of pressure recovery.

The second design improvement was the introduction of locating fins. The 16 mm prototype was tested first without any locating fins. From this test it was learned that the following 12 mm and 8 mm prototypes may be improved by adding small locating fins to further ensure improved concentricity with the outer surface of the annulus around its axis. The fins are positioned at the entrance of the diffuser at 120° intervals around the axis as shown in Figure 4.7. The fins make up less than 2 % of the sectional flow area and are therefore not expected to significantly influence the validation of the axisymmetric CFD model.

[2]This CFD model will be developed and validated in the following chapter.

4.2.3 Manufacturing the prototypes

A drawing describing the design of the plastic part of a prototype (that fits onto a nozzle assembly) is shown in Figure 4.7. The figure also shows the (temporary) printing foothold where printing starts. The prototype is printed in this direction to prioritize an accurate surface finish around the Tadpole's nose.

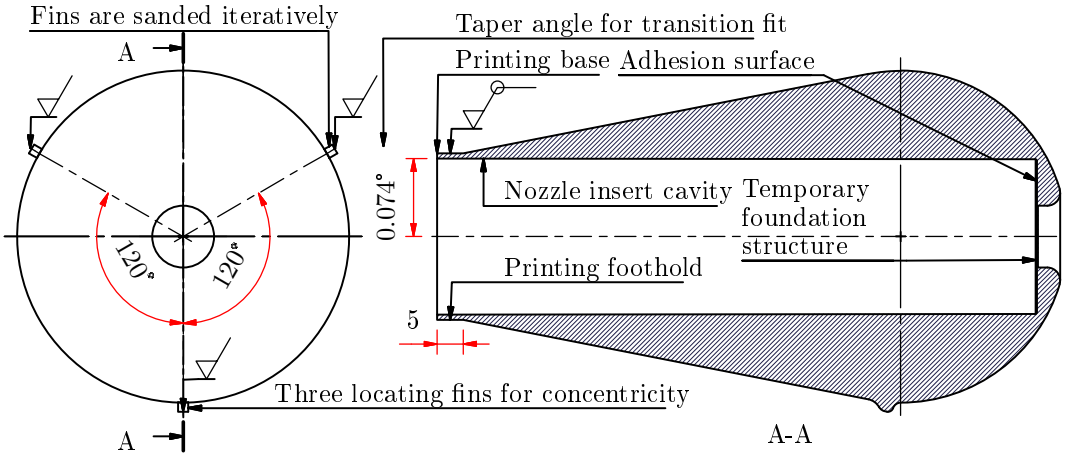

Figure 4.7: Description of a typical 3D printed prototype.

Printing

The plastic parts of the prototypes were printed using a hard ABS+ plastic printing filament. Figure 4.8 shows a prototype during the printing process. A temporary infill structure is shown within the internal cavity which provides a foundation for the overarching bulbous region of the Tadpole. The prototypes print within 25 hours on average.

A fine filament layer height of 0.12 mm was used in the parts. The solid outer shell is made up of 10 layers at the top (around the nose), 9 layers at the printing foothold and 5 layers everywhere else. Figure 4.8 also shows that the plastic parts are porous with an interior infill of 50 % to provide axial structural strength in the form of a honeycomb structure. The porous internal structure is sealed from the pressurized flow domain by the outer shell. Although, no evidence of permanent deformation was suspected after prototype testing and therefore pressure-related deformation is not expected to influence the CFD validation.

Figure 4.8: Prototype during the 3D printing process.

Processing and installation

After each plastic part was printed, the temporary infill structure was removed. The printed surface finish of the part is relatively rough. A smooth surface is desired so that the domain can be recreated in the CFD model. Light sandpaper was applied to smooth out the foothold at the base as well as the entire exterior surface as shown in Figure 4.9. It is expected that the uncertainty of the resulting surface is a deformity of less than the printing layer height (0.12 mm) and that this deformity will have negligible effect on the CFD validation in comparison with a dominating effect which will later be described in Section 4.4.3.

The fins were printed to protrude an excess of 0.5 mm so that they can be processed for a transition fit. To process the fins, the plastic part is grasped and manoeuvred to draw lines of equal length on a piece of sandpaper with each fin (as the point of contact) successively. This is iterated until a neat transition fit is achieved with the outer shell of the annular region. This technique makes use of randomness and repetition to remove operator error and ensure equal surface removal on each fin. The technique is similar to a dated method used to form a parabolic reflective surface on a (astronomical) telescope mirror with a remarkably low surface slope error.

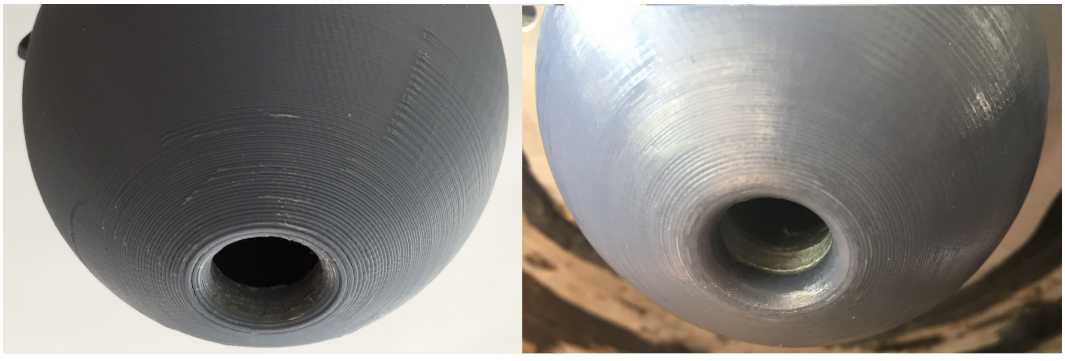

Figure 4.9: The 12 mm prototype before surface processing (left) and after processing and installation (right).

Negligible error is expected in the concentricity of the finned Tadpoles.

After surface processing, the plastic part can be installed in the apparatus. Figure 4.10 shows the nozzle assembly within the apparatus without the plastic part. The figure shows three spots of cyanoacrylate adhesive (also known as super glue) are applied to the front of the nozzle to make contact with the internal adhesive surface of the plastic part (adhesive surface is shown in green on Figure 4.4). The plastic part is pressed onto the nozzle assembly. The cylindrical opening of the plastic part has an angular taper (shown in Figure 4.7) to ensure a transition fit onto the nozzle assembly. After fitting, a small internal gap between the nozzle assembly and the plastic part is filled using a thin layer of epoxy — Epidermix 372. The hemispherical dome is installed as shown in the right of Figure 4.10. The axial position of the Tadpole (ξ) is then calibrated following the process detailed in Appendix B.4.

Figure 4.10: The nozzle assembly within the experimental apparatus with adhesive applied to attach a prototype (left), the hemispherical dome is also shown after installation (right).

4.3 Experimental procedure

The full experimental procedure incorporates a test at ambient temperature and a heat transfer test with the steam system activated. The ambient test determines the total pressure loss characteristics of the domain without the influence of heat addition. The heat transfer test investigates the heat transfer and pressure loss characteristics together. Both tests together require approximately 6 h to complete.

The experimental measurements are time-averaged over approximately 6 min for the ambient temperature (unheated) tests and 10 min for the heated tests after steady-state operation is reached. Readings are taken at 4 s intervals and averaged over the test period. The time averaging accounts for minor fluctuations of the air-supply temperature due to the air-supply system being situated outside the laboratory. In order to maintain consistency and comparability with the baseline impinging jet configurations, the method is kept the same as in Erasmus *et al.* (2020*b*) and is exhibited in Appendix F.

4.4 Error and uncertainty

Accuracy of the experimental results is desired in order to firstly compare the heat transfer and pressure loss characteristics of Tadpole prototypes with impinging jets and secondly to validate a CFD model. In this section, the calibration of the sensors will be detailed and the error of the sensor measurements will be estimated. Thereafter, general extraneous variables will be discussed and, where possible, their effect on the performance characteristics of the domain will be estimated.

4.4.1 Calibration

The differential pressure transducers were calibrated with a mercury manometer (between 5000 kPa and 50 000 kPa) and a BETZ 5000 water manometer (between 0 kPa and 5000 kPa). A piecewise linear model of measured pressure and voltage was fitted to the differential pressure transducers. The pressure transducers' calibration readings deviate from the calibration models by an average of 0.238 % and a maximum of 4.03 %. The gauge pressure sensor was calibrated using a standardized 10 bar analogue pressure gauge and a linear model was fitted. The gauge pressure sensor has a mean calibration uncertainty of 0.161 % and a maximum deviation of 1.30 %.

The thermocouples were calibrated with a FLUKE 9142 dry well calibrator over the measured temperature range (between 284 K and 373 K) and a linear model was fitted. The thermocouples have a mean calibration deviation of 0.109 K and a maximum deviation of 0.677 K.

4.4.2 Sensor measurement error analysis

Taylor (1997) details an error analysis methodology that estimates the uncertainty of a function from the propagation of uncertainty in the function's constituent parameters. Moreover, each constituent parameter's uncertainty has a characteristic propagation to the overall function's uncertainty depending on whether the parameter participates in a sum, product or power operation.

In the present experimental analysis, the propagation of the calibration uncertainty of sensor measurements is estimated on the key operating characteristics according to this methodology. The results of the analysis are given in Table 4.3.

Table 4.3: Results from the experimental uncertainty analysis.

Uncertainty	Unit	$\dot{Q}_{\text{air}}$	h_{is}	Nu_{is}	$\dot{m}_{\text{air}}$	Re_{n}	Δp_{t}	K_{loss}
Maximum	[%]	2.75	6.43	6.43	2.74	2.74	7.42	9.68
Mean	[%]	0.148	2.91	2.91	0.146	0.146	0.522	0.699

The sensor uncertainty affects all tests and thus it is understood that a relative comparison between Tadpole prototype configurations and impinging jets will be reliable. The comparison with CFD results will be subject to error bars reflecting this uncertainty. Additional uncertainty in the experimental results also arises from the limitations and extraneous variables of the apparatus.

4.4.3 Limitations and extraneous variables

Geometric uncertainty

The dominating uncertainty within the experimental apparatus is expected to be the axial position measurement (ξ) of 0.5 mm. This is the discretization of the axial position measurement device shown in Figure 4.11. The ξ measurement has a significant effect on the flow area at the Tadpole's nose as was previously demonstrated in Figure 3.3. The effect on a particularly sensitive Tadpole configuration is an uncertainty of around 32 % on the minimum flow area (at the Tadpole's nose). This is expected to affect the heat transfer and pressure loss characteristics significantly. It is for this reason that the effect of other minor (and not practically quantifiable) prototype geometric imperfections on the performance characteristics will not be scrutinized. Such imperfections include the previously described Tadpole's surface finish, the locating fins, concentricity and pressure-related elastic deformation of the Tadpole. In the following chapter, a CFD sensitivity analysis will be conducted on the ξ measurement to understand its effect on the CFD validation together with a correction of the most affected results.

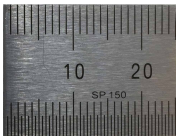

Figure 4.11: Axial position (ξ) measurement device.

Heat transfer uncertainty

A general concern is the correct measurement and calculation of the heat addition rate. To verify this, a concomitant method to obtain the heat transfer rate to the system was recorded using the latent heat addition from condensation in the steam bath: $\dot{Q}_{\text{cond}} = \dot{m}_{\text{cond}} h_{\text{fg}}$. The net condensate mass accumulation rate, $\dot{m}_{\text{cond}}$, was measured with a condensate collection container on a weight scale over the steady-state test time period.

The condensate measurement was calibrated with the accumulation rate at a steady-state operation period while the test section's air mass flow rate was zero. This represents the extraneous condensate that forms within the collection container. This accumulation rate was subtracted from the measured gross rate during a test to obtain the net rate that reflects the condensation rate due to heat transfer to the test section. Figure 4.12 shows the absorbed heat flux calculated from the energy balance on the air stream ($\dot{q}_{\text{air}}$) primary method together with the calibrated latent heat flux ($\dot{q}_{\text{cond}}$) concomitant method.

From the data points of all the flow rates as shown in Figure 4.12, $\dot{q}_{\text{air}}$ and $\dot{q}_{\text{cond}}$ deviate an average of 0.958 %, this verifies the air energy balance method. The noted deviation is attributed to a varying lab temperature affecting the collection cup's temperature and hence the total accumulated condensate. Therefore it is expected that the uncertainty of the air energy balance is less than this deviation. Nonetheless, the deviation is less than the maximum sensor uncertainty of $\dot{q}_{\text{air}}$ and therefore considered negligible.

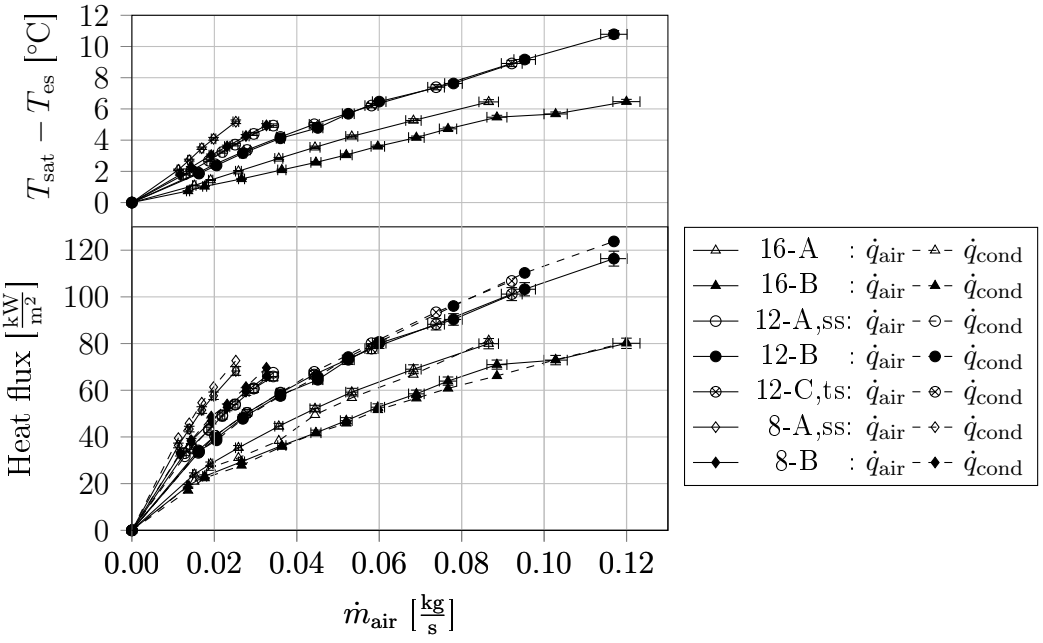

Figure 4.12: Experimental heat addition flux with the corresponding temperature difference between the steam and the exterior heat transfer surface.

Figure 4.12 also shows the corresponding temperature difference between the measured steam saturation temperature and the calculated exterior heat transfer surface temperature (T_{es}). It can be observed that the greater this temperature difference becomes, the greater the absorbed heat flux becomes for all the tests. This temperature difference is the driving force of heat addition through steam condensation.

There is uncertainty in the calculated T_{es} using the empirical heat transfer coefficient (Equation 4.4). This surface temperature is not measured because thermocouples at this position would affect the heat transfer experiment adversely. Thus, the limiting boundary of uncertainty was explored with a sensitivity investigation on the Nusselt number depicted in Figure 4.13.

The nominal Nusselt number arising from the empirical condensation coefficient is shown along with a lower boundary representing the assumption that there is no temperature difference between the condensation surface and the steam.

It is clear that at higher Reynolds numbers, the assumption of $T_{\text{es}} \approx T_{\text{sat}}$ deviates a maximum of 10.3 % from the nominal result. This is understandable because, as demonstrated by Figure 4.12, the steam and condensate temperature difference (condensation driving force) increases with the nozzle-region Reynolds number together with the heat extraction rate of the test section. Therefore, to incorporate the effect of a decreasing condensation surface temperature with an increasing heat transfer rate, the condensation heat transfer coefficient is retained in the processing of the experimental results. It is expected that the error in the temperature estimation of the condensation surface would be insignificant and at most constrained by the demonstrated lower boundary deviation — on the same order as the maximum sensor uncertainty for Nu_{is}.

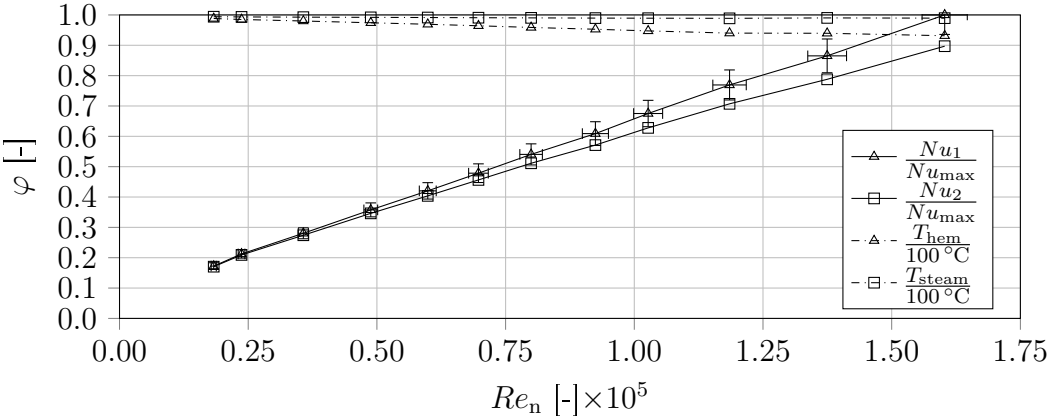

Figure 4.13: Sensitivity of the Nusselt number to the approximation of T_{es} — with Nu_1 representing the consideration of an empirical condensation heat transfer coefficient and Nu_2 representing the assumption that $T_{\text{es}} \approx T_{\text{sat}}$.

Another potential uncertainty arises from the variation in the inlet temperature from the air supply between and throughout tests. To account for this, the CFD model will use the average inlet temperature boundary condition for each data point to recreate the test environment for validation. Furthermore, the Nusselt number is characteristically a function of the Reynolds number and Prandtl number. At 1 bar between 10 °C and 30 °C (a conservatively large ambient temperature variation), the Prandtl number of air deviates 0.38 % (VDI, 2010). For a steady-state testing period, the nozzle-region Reynolds number was found to vary by around 0.34 %, caused by a slight system mass flow rate drift. To estimate the propagation of these variables on the Nusselt number, the impinging jet Nu_{overall} correlation from Erasmus *et al.* (2020*b*) was used along with power-law and product error propagation from Taylor (1997). The uncertainty on the Nusselt number arising from these deviations is 0.38 % and is therefore deemed negligible in comparison with the sensor uncertainty.

A heat transfer measurement limitation arises from the characteristic cross-flow configuration of the apparatus comprised of the nozzle assembly communicating with the annulus and also a finned section. A small amount of cross-flow heat transfer occurs between the inner tube and the annular region. A 144 mm cross-flow section was therefore included in the impinging jet CFD model by means of a conduction domain in the nozzle assembly. It was found that introducing the conduction domain to enable cross-flow heat transfer increases the measured Nusselt number by 0.07 % (Erasmus *et al.*, 2020*b*). It is therefore expected that, with the entire cross-flow region making up around 432 mm, the uncertainty in Nusselt number arising from cross-flow is on the order of 0.21 % and is thus negligible.

4.5 Safety

Before commencement of experimental testing, the safety risks associated with the apparatus and the prototypes during operation were analysed. This included thick-walled pressure vessel stress calculations based on Dowling (2013). It was determined that the modified components of the apparatus are classified within the 'not regulated' region of the SANS 347 pressure vessel standard, SABS (2012).

The fluid to body force interaction between the air flow and the Tadpole was explored using CFD to investigate the risk associated with the sudden dismantlement of the Tadpole prototype from the nozzle assembly during operation. It was found that the net thrust on the Tadpole acts so as to push the prototype onto the nozzle assembly. This is in agreement with the changing of the flow domain (increasing ξ) with mass flow rate detailed in Section 4.2.1. The test setup and prototype configuration are therefore safe.

4.6 Results

This section presents the experimental heat transfer and pressure loss characteristics of the Tadpole prototype configurations in perspective with the impinging jets.

4.6.1 Kinematic development

Figure 4.14 shows the kinematic characteristics of the prototype configurations for the lowest mass flow rate data point of each experimental result set (excluding the supersonic results). Observing the variations in the kinematic development of the configurations enables understanding the variations in the performance characteristics depicted in the following subsections. Moreover, higher Mach numbers in the narrow flow region will tend to produce larger heat transfer coefficients and larger pressure losses.

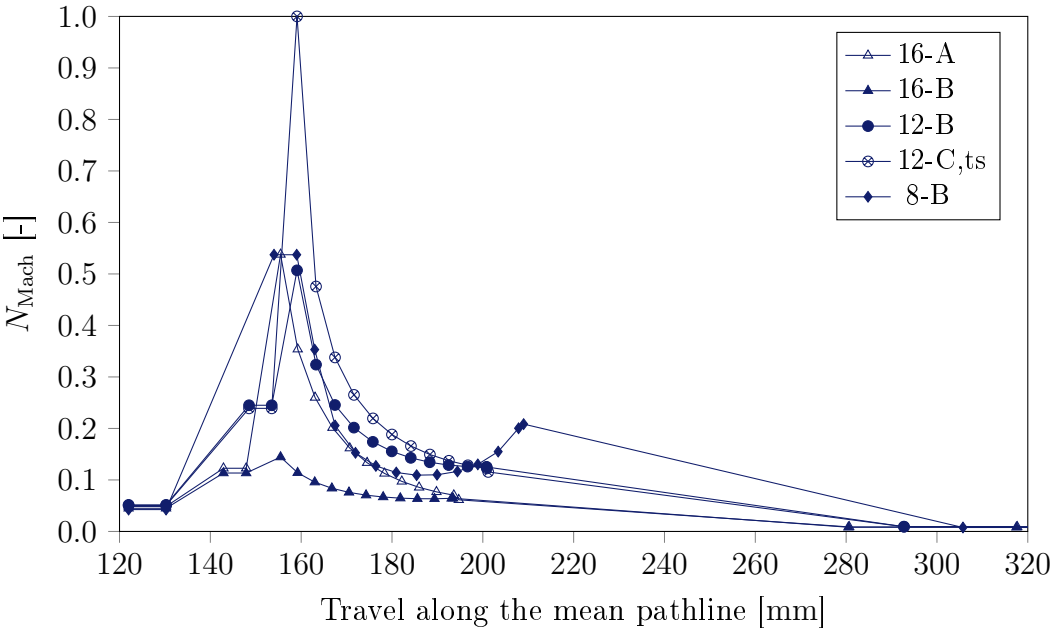

Figure 4.14: Comparison of the kinematic model's Mach number development as a function of the mean (1D) pathline for the Tadpole configurations at the lowest mass flow rate data point of each experimental result set.

4.6.2 Heat transfer characteristics

The overall heat transfer coefficients are presented in Figure 4.15. The coefficients develop almost linearly with mass flow rate.

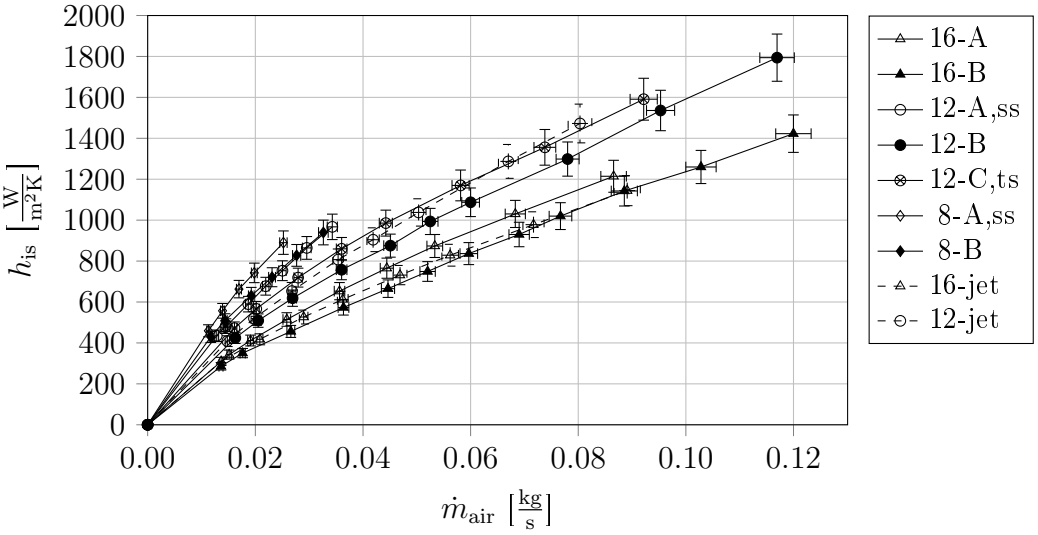

Figure 4.15: Comparison of the overall heat transfer coefficients between the experimental results of the Tadpole configurations and the impinging jet configurations with the maximum sensor uncertainty shown.

The characteristics of the Tadpole configurations straddle the impinging jets with corresponding nozzle diameters. The two supersonic cases represent the highest heat transfer coefficients with the steepest gradients as well.

It is observed that, in an experimental Tadpole configuration where the peak flow velocity substantially exceeds that of a corresponding impinging jet, the heat transfer coefficient is greater; but where the peak velocity is the same or even slightly higher, the heat transfer coefficient is lower. From the CFD simulations described in the next chapter, it is observed that the impinging jet characteristically maintains the maximum developed velocity around the impingement surface (after being redirected by the surface) for a longer arc length than a corresponding Tadpole. After impingement, the flow of the impinging jet is constrained only by the impingement surface, whereas the Tadpole constrains the flow with two walls (in the narrow flow region). Immediately downstream of the Tadpole's nose, the narrow flow region (of the experimental prototypes) decelerates the flow as shown in Figure 4.14. The impinging jet domain does not exhibit deceleration in the wall jet at the same rate due to less constraint on the flow movement near the heat transfer surface. The impinging jet also generates significantly higher turbulence kinetic energy levels near the velocity gradient (mixing layer) of the wall jet whereas the Tadpole does not generate high levels of turbulence kinetic energy due to the absence of a mixing layer.

It is accordingly postulated that the increased deceleration of a similar peak velocity magnitude and significantly reduced turbulence kinetic energy within the narrow flow region of the Tadpole (relative to an impinging jet

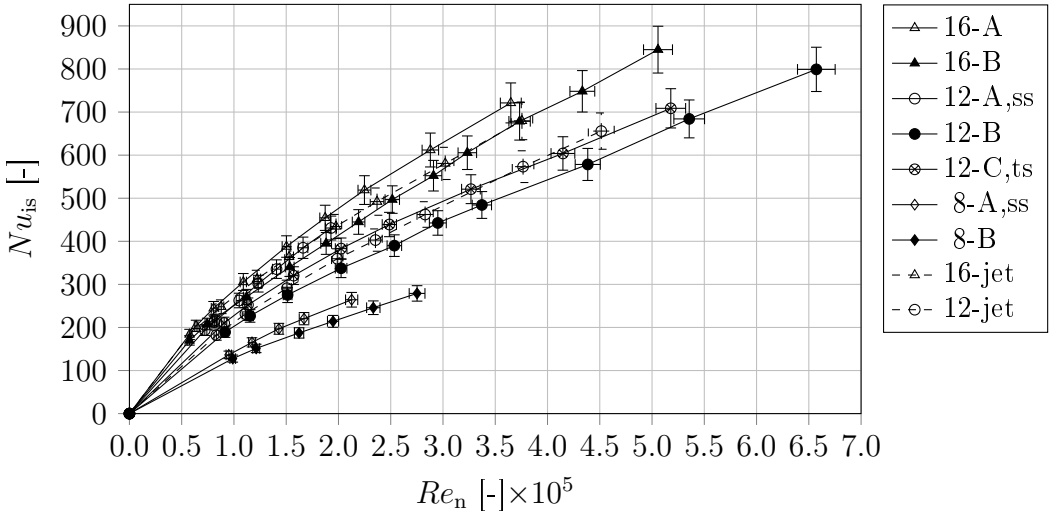

Figure 4.16: Comparison of the overall Nusselt numbers (based on the nozzle-region diameter) between the experimental results of the Tadpole configurations and the impinging jet configurations.

with a similar peak velocity magnitude) results in an increased boundary layer thickness, thereby developing a lower surface heat transfer coefficient. This may be improved in the future by using a non-hemispherical Tadpole surface to maintain the peak velocity magnitude through the narrow flow region.

Nusselt numbers are shown in Figure 4.16. In addition to the heat transfer coefficient, the Nusselt number is affected by a dimensional variable. The effect is that the largest Nusselt numbers arise from the largest nozzle-region diameters instead of the inverse relationship shown with h_{is} in Figure 4.15. Although, a similar comparison between the Tadpoles and the jets is depicted.

4.6.3 Total pressure loss characteristics

The total pressure losses are presented in Figure 4.17 for the heated and ambient temperature (unheated) domains. The two result-sets with the steepest gradients correspond with the supersonic cases and the sets with the most gradual gradients correspond with configurations developing the lowest peak velocity magnitude. It is demonstrated that both the heat transfer coefficient and total pressure loss increase with the peak velocity magnitude.

Comparing performance characteristics between Tadpoles and jets, it is shown that 16-A experiences a marginally lower total pressure loss (in the heated domain) compared with 16-jet while the heat transfer coefficient is higher for all mass flow rates. The 12-C,ts case experiences significantly lower pressure losses than 12-jet at higher mass flow rates while the heat transfer coefficients are similar. This demonstrates that the Tadpole is capable of outperforming an impinging jet.

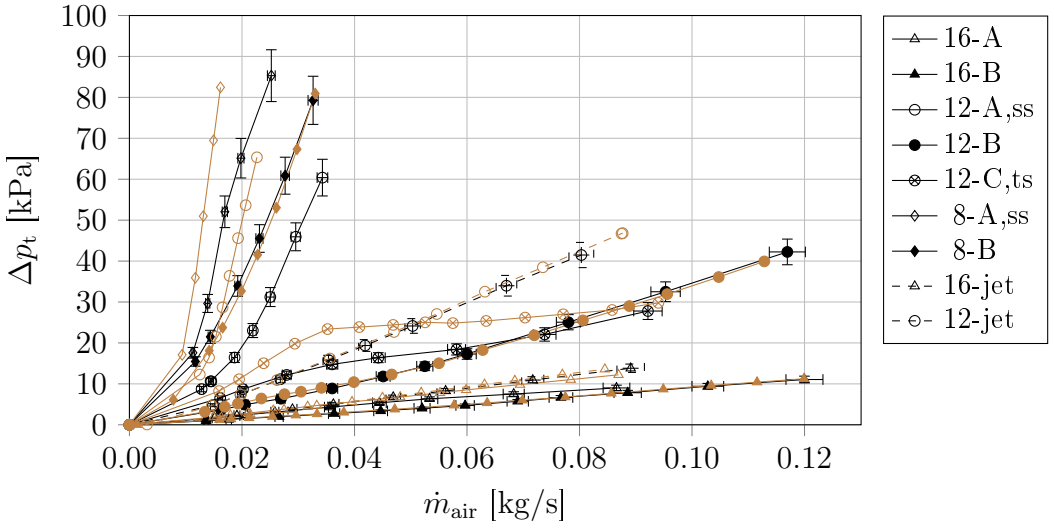

Figure 4.17: A comparison of the total pressure losses over the experimental heated (black) and ambient (brown) domains of the Tadpole configurations and the impinging jet configurations with the maximum sensor uncertainty shown.

It is insightful to observe the calculated Mach number at the Tadpole's nose in Figure 4.18. This represents the maximum N_{Mach} in the domain of the subsonic cases and N_{Mach} at the sonic threshold of the supersonic nozzle for the supersonic data points. It can be observed that the Mach number for 12-C,ts is maintained near this threshold. Notably, the pressure loss characteristics of this case appears to make a cusp at a sonic transition, although the calculated

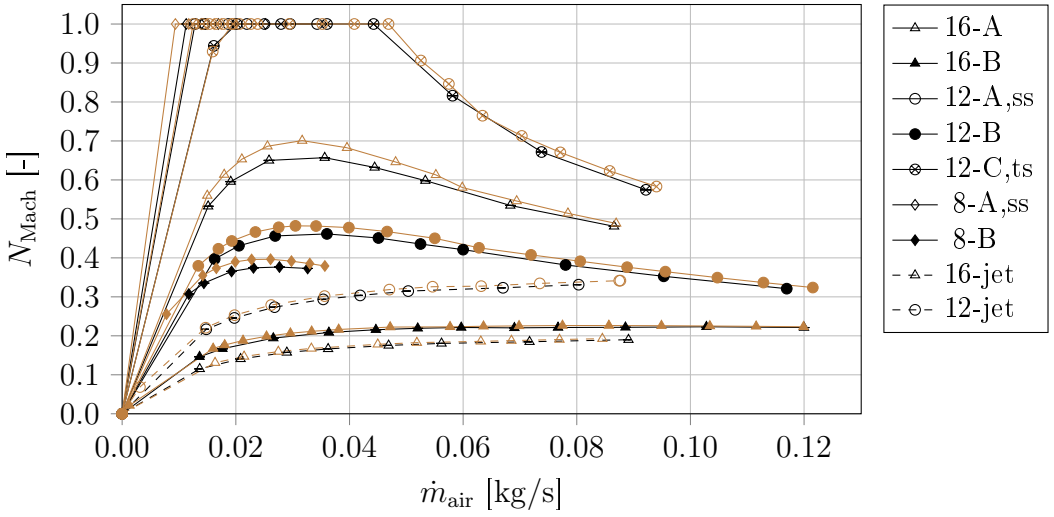

Figure 4.18: Comparison of the calculated Mach numbers at the nose of the Tadpole configurations compared with the Mach number at the nozzle throat of the impinging jet configurations for the heated domain (black) and the ambient domain (brown).

N_{Mach} in Figure 4.18 predicts this cusp two data-points later. A distinctly different high frequency sound was emitted from this test case — seemingly attributed to the high frequency instability of the transonic flow.

It was found that, for the transonic and supersonic cases at the same mass flow rate, the total pressure loss is significantly lower (around 40 %) in the heated domain than in the ambient temperature domain. This may be because sonic speed is elevated at higher temperatures — increasing by around 2.48 % per 15 °C — this is expected to modify the maximum developed supersonic velocity and thereby the pressure loss.

The loss coefficients for the heated and ambient domains are presented in Figure 4.19. The jet configurations all produce an average loss coefficient of 0.992 for the turbulent flow regime with evidence of a laminar to turbulent transition at $Re \approx 10^5$ and higher loss coefficients in the transitional flow regime. A loss coefficient of 1 indicates that all the dynamic pressure developed in the nozzle is dissipated.

Several subsonic Tadpole configurations produce loss coefficients of less than 1, indicating that the narrow flow region and the diffuser are able to substantially recover the dynamic pressure developed in the nozzle region (even after a further increase in dynamic pressure downstream of this region). Of the prototype configurations, 16-B reaches the smallest (ambient temperature) loss coefficient of 0.512. The supersonic loss coefficients are more than 1 because the narrow flow region is significantly accelerating the flow velocity (and thereby the dynamic pressure) downstream of the Tadpole's nose. This indicates that a supersonic Tadpole in unfavourable.

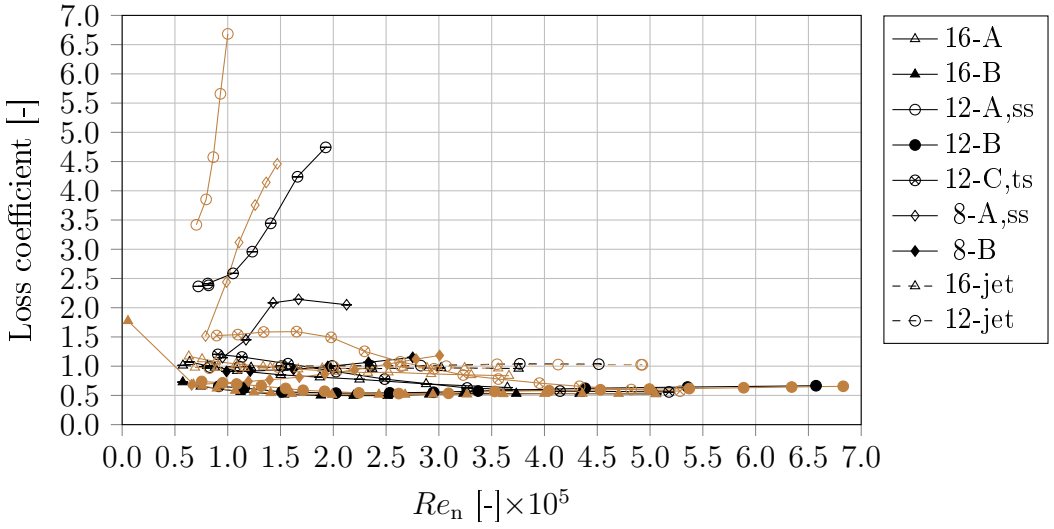

Figure 4.19: Comparison of the loss coefficients (based on the dynamic pressure at the nozzle throat) of the Tadpole compared with the impinging jet configurations for the heated domain (black) and the ambient domain (brown).

The Tadpole shows favourable performance in the subsonic realm and the turbulent flow regime.

The 8-B configuration showed a notably high loss coefficient and represents a special case. The high loss coefficient is attributed to the deceleration followed by a subsequent substantial re-acceleration in the narrow flow region shown previously in Figure 4.14. It is accordingly noted that significant re-acceleration should be avoided in the narrow flow region. This can be achieved if $\xi \approx 0$ or $\xi \leq 0$ is maintained as demonstrated previously in Figure 3.4.

The impinging jet loss coefficient demonstrates independence to the Reynolds number within the turbulent flow regime. A characteristic difference can be observed when comparing the jet configurations and the Tadpoles. The Tadpole configurations produce loss coefficients that change with Reynolds number while it is expected that subsonic loss coefficients for a fixed geometry should remain constant (as with the jets) in the turbulent flow regime — turbulent Reynolds number independence was also shown for diffuser performance metrics in Adkins *et al.* (1983). It is thus understood that the variation in loss coefficient within the turbulent flow regime for the subsonic Tadpole configurations can be attributed only to the shifting of ξ with mass flow rate. One similarity with the jets is that the loss coefficients for the configurations with a lower peak velocity: 16-A and 16-B tend to be slightly higher at lower Reynolds numbers, this is also understood to be a laminar to turbulent transition.

With higher loss coefficients at lower transitional Reynolds numbers, it is possible that adding vortex generators upstream of the Tadpole diffuser may improve the low Reynolds number performance (Manglik, 1987).

4.7 Conclusion

The experimental apparatus has been described and seven Tadpole prototype configurations have been developed. The experimental procedure and the processing of the results have been detailed along with an investigation into the uncertainty of the results.

It is expected that the uncertainty of the Tadpole's axial position will hinder the ability to re-produce the results. Future manifestations should be manufactured so that the axial position support is robust with the applied fluid-body force and the measurement of the axial position is more precise.

The experimental results have shown that two Tadpole configurations (16-A and 12-C,ts) are capable of outperforming an impinging jet as a heat transfer device. The Tadpole shows favourable performance in the subsonic realm and the turbulent flow regime. Therefore, the concept has promise and is recommended for further exploration. In the following chapter, the CFD model will be developed and validated with the experimental results.

Chapter 5

CFD investigation

This chapter describes the development of a CFD model using ANSYS Fluent® which enables predicting an extensive variety of applications and operating conditions of the Tadpole's flow domain. The model is validated with the experimental results. At the end of the chapter, further insight into the domain is revealed from the CFD model.

5.1 Development of the CFD validation model

The flow domain for the RANS CFD validation model is axisymmetric. As detailed in Section 2.2 — RANS turbulence models have been successfully validated in the axisymmetric domain. Within the experimental apparatus, heat travels from steam, through an aluminium volume and a flange to reach the air stream. Because steam condenses at a constant temperature, the heat source is modelled using a constant temperature boundary condition.

In order to integrate the conjugate heat transfer characteristics in the domain, a bottom-up modelling approach is taken for the model development. All significant parts within the validation domain are therefore modelled. This includes the aluminium nozzle assembly, the annulus, flanges as well as the porous plastic ABS+ parts of the Tadpole prototypes. The effective thermal conductivity of the porous prototypes was calculated according to the procedure in Appendix E. The values and origins of the air and material properties are also given in Appendix E.

The experimental validation CFD flow domain is illustrated in Figure 5.1. The figure shows a partition (blue line) that cuts through the middle of the convection domain to form an approximated mean pathline. This is used to verify the 1D analytical kinematic model of Section 3.2 in Appendix C.

Three data points from each configuration of the heated system experimental results were chosen for validation. Moreover, the first data point, the nearest to middle and the last data point of the investigated heat transfer coefficients.

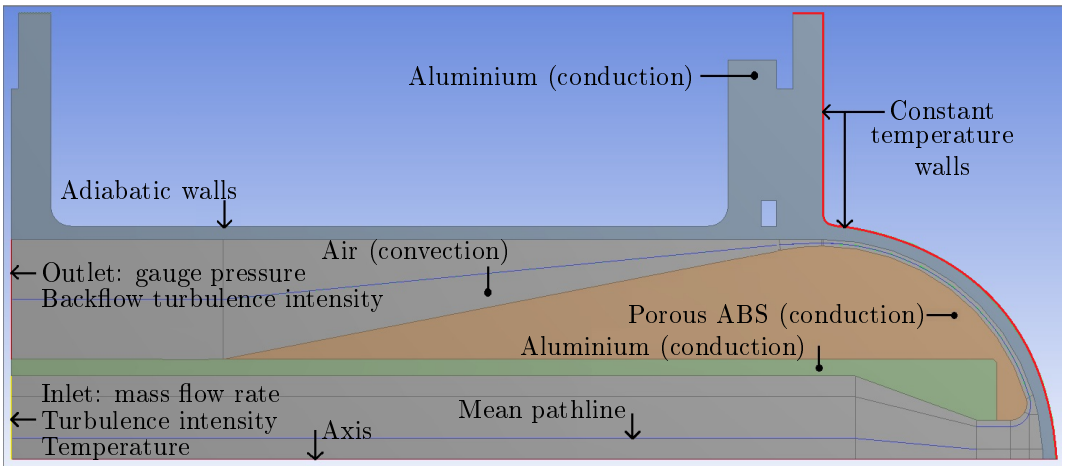

Figure 5.1: Flow domain of the Tadpole's experimental validation CFD model.

Because the geometry of the experimental flow domain changes during each test (previously detailed in Section 4.2.1), the geometry at each validation point mass flow rate was recreated (15 unique geometries).

Although the supersonic characteristics of the flow domain were investigated experimentally, the supersonic realm will not be validated using the CFD model because the Tadpole's envisaged application is not supersonic.

5.2 Boundary conditions

Appendix G contains the set of boundary conditions for each simulation. As depicted in Figure 5.1, the experimental validation boundary conditions are:

- The inlet temperature, mass flow rate and back-flow turbulence intensity[1] (mass flow rate inlet).
- The outlet gauge pressure and backflow turbulence intensity (pressure outlet).
- The temperature of the exterior heat transfer surface (constant temperature)[2].
- Adiabatic conditions on all other exterior surfaces (zero heat flux).

[1] The back-flow turbulence intensity was not investigated experimentally. Instead, it was approximated using fully developed turbulent duct flow empirical correlations from ANSYS (2016). A sensitivity analysis was conducted on the affect of increasing the turbulence intensity for one data point from around 4 % to around 7 % at the inlet and outlet. This resulted in an increase in h_{is} and Δp_t of 1.31 % and 0.35 % respectively. This sensitivity is below experimental uncertainty and is therefore deemed negligible.

[2] For the application cases in Chapter 6 and Chapter 7, heat flux and heat generation rate boundary conditions will be used instead of a constant temperature boundary condition.

5.3 Modelling considerations

5.3.1 Turbulence and viscous effects

The literature study revealed two turbulence models that are most suitable for this flow domain: the k-ω SST model and the Four-Equation Transition SST model. These models are both considered in this work.

Both models were implemented with the production of k limiter and the Kato-Launder model. The k-ω SST model was additionally used with the intermittency transition extension function, turbulence compressibility as well as low Reynolds number correction. It was found that the solver often diverges without low Reynolds number correction. This correction equation is understood to improve the modelling of the laminar flow region near the stagnation region.

The energy transport equation must be solved to account for the flow of heat through the domain as well as viscous heating. Compressibility effects are accounted for because the flow may venture near sonic velocity.

5.3.2 Radiation

The Tadpole's exterior surface is characteristically near the interior heat transfer surface. The view factor between the two surfaces is almost unity — for example, the 12-A configuration's view factor is 0.98. This means that, if the Tadpole's surface is colder than the temperature of the heat transfer surface, there will be net radiative heat transfer to the Tadpole's surface. This heat will accordingly move into the air flow. This effect may especially be pertinent at elevated operating temperatures according to the fourth temperature exponent in the Stefan-Boltzmann law equation.

The radiation between surfaces enclosing the convection flow domain is modelled with the Discrete Ordinates (DO) radiation model (computational settings given in Appendix H). This was chosen because it is an appropriate model for localized heat sources and has a modest solving computational requirement (ANSYS, 2016). Because the narrow flow region is thin and free of particles, the participation of air in radiation modelling was neglected.

5.3.3 Computation

The solver settings, relaxation details, computational mesh generation, grid independence study and a convergence investigation are exhibited in Appendix H. In summary, a fully-structured convection domain mesh was developed. It is robust with grid refinement and appropriate for LRN turbulence models. The convergence study showed that sufficient convergence was reached for most cases although five data points were characteristically unstable — these were corrected.

5.4 Results

This section firstly presents an initial CFD validation sensitivity of this domain and secondly a full validation with the most suitable turbulence model. Thereafter, additional insights will be gleaned from the model.

5.4.1 Validation Sensitivity

An example Tadpole and jet configuration were chosen for an extensive turbulence validation and modelling sensitivity study. A turbulence model comparison is given in Table 5.1. It is demonstrated that the Four-Equation Transition SST model is better validated for both the Tadpole and the impinging jet; this was also observed for the other subsonic and transonic configurations.

Table 5.1: Average deviation between the CFD turbulence models and the experimental results.

	16-B		16-jet	
	k-ω SST	Transition SST	k-ω SST	Transition SST
h_{is}	−6.59 %	−4.88 %	11.9 %	5.12 %
Δp_{t}	−35.4 %	−33.4 %	−4.72 %	−6.93 %

To investigate parameters that affect the heat transfer validation, the model's sensitivity to various effects is shown in Figure 5.2. Included are the turbulence model, the conductivity of the aluminium outer shell, the deactivation of internal conduction through the plastic Tadpole part and aluminium nozzle, internal radiation as well as a hypothetical aluminium Tadpole (to determine whether conduction through the Tadpole is favourable). The latter effects were investigated with the Transition SST turbulence model.

Figure 5.2 shows that for the low temperature experimental setup: internal radiation makes almost no difference to the low temperature heat transfer characteristics. Although, the radiation effects will be more significant at higher temperatures.

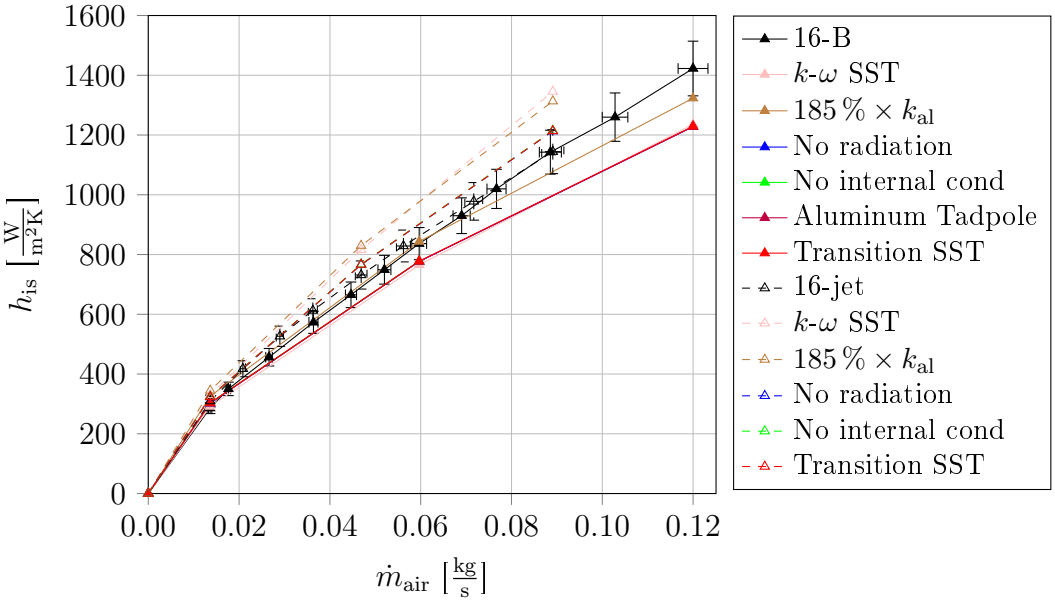

Figure 5.2: Comparison of the overall heat transfer coefficients between the experimental results of the 16-B Tadpole configuration, the 16-jet configuration and CFD results of various domain and model modifications.

Figure 5.2 demonstrates a negligible heat transfer effect of deactivating internal conduction through the Tadpole and/or the nozzle assembly. Furthermore, it is demonstrated that a hypothetical aluminium Tadpole also has almost no heat transfer effect[3]. This confirms the initial expectation that conduction through the Tadpole is not necessarily favourable.

The most notable effect in Figure 5.2 is increasing the thermal conductivity of the aluminium alloy to that of pure aluminium (185 % × k_{al}). This is attributed to conjugate heat transfer occurring in the domain. Moreover, the system is highly sensitive to the conductivity of the outer shell and the flange because, with an elevated k_{al}, the condensation heat flux travels farther through the flange and the annular outer shell, thereby increasing the effective interior convective heat transfer area and amplifying the observed heat transfer coefficient.

5.4.2 Validation results

The experimental results are now compared with the Four-Equation Transition SST CFD model in Figure 5.3 and Figure 5.4. Two corresponding impinging jet validation sets from Erasmus *et al.* (2020*b*) are also shown in the figures with the same turbulence model and settings.

[3]The incremental effects can be observed by zooming into Figure 5.2.

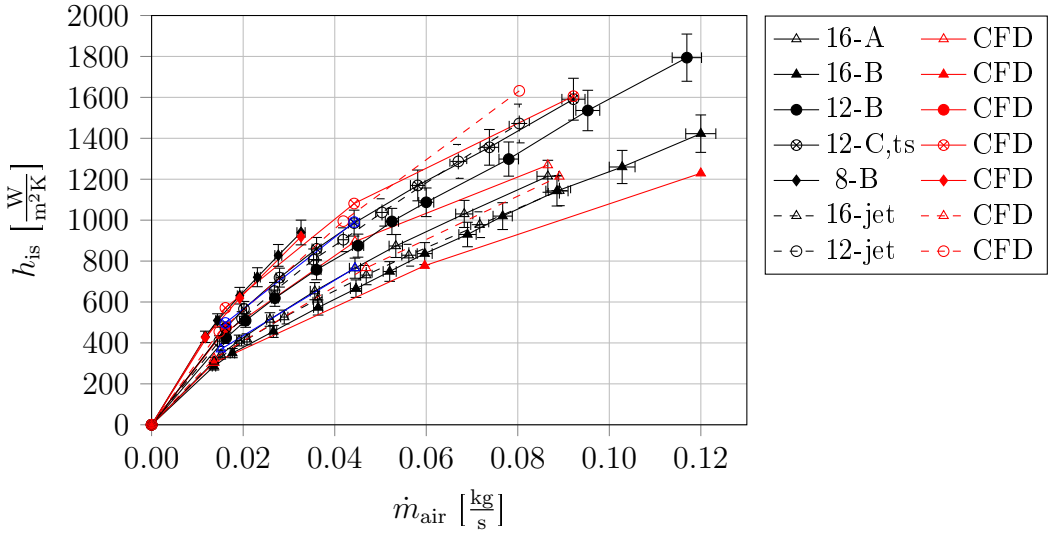

Figure 5.3: Comparison of the overall heat transfer coefficients between the experimental results (of the Tadpoles and impinging jets) and the default CFD results (red) as well as the corrected ξ CFD results (blue); with the maximum sensor uncertainty shown.

The subsonic and transonic Tadpole configurations deviate by an average (absolute value deviation) of 4.60 % in h_{is} and 27.8 % in Δp_t from the CFD results excluding four outliers with Δp_t deviations larger than 50 %.

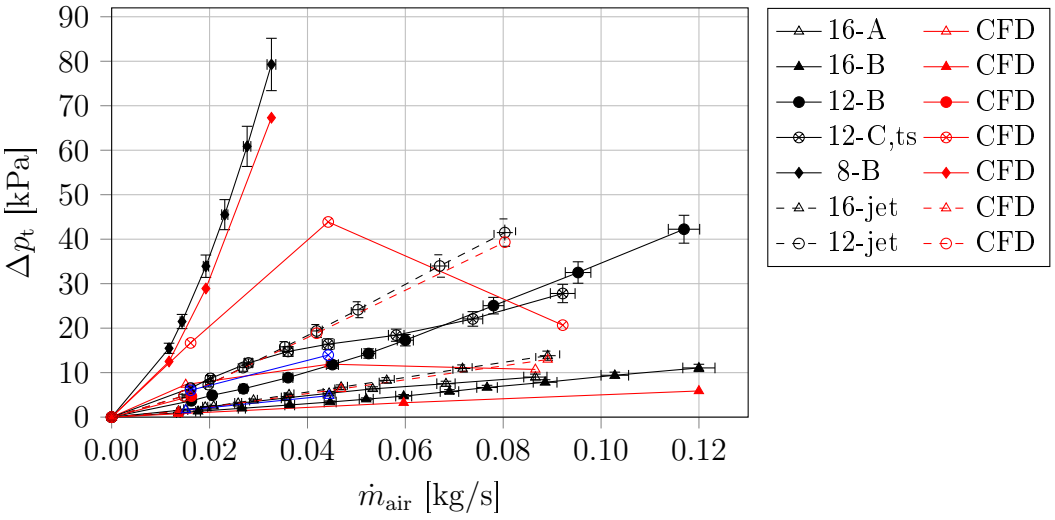

Figure 5.4: Comparison of the total pressure losses over the experimental heated domain (of the Tadpoles and impinging jets) and the default CFD results (red) as well as the corrected ξ CFD results (blue); with the maximum sensor uncertainty shown.

From Section 4.4.3, a dominating uncertainty was expected from the measurement of ξ for the domain. This is understood to be the cause of four outlier data points as well as the inconsistency in the deviations between configurations. Accordingly, a further analysis on ξ was conducted on the CFD mesh for these outliers to correct the predictions of ξ. Moreover, the ξ value in the CFD mesh of the outliers was modified until the resulting CFD h_{is} became similar to that of the experimental results — these are represented in blue in the validation figures. The average modification on ξ was $-0.42\,\text{mm}$ (near the $5\,\text{mm}$ discretization interval of the ξ measurement device shown previously in Figure 4.11). The result is that the corrected data points deviate significantly less than before and to a similar degree of the impinging jets' deviations. It is clear that a small change in ξ can affect the performance characteristics significantly.

Including the corrected results, the CFD validation deviation becomes $4.29\,\%$ for h_{is} and $22.9\,\%$ for Δp_{t}. The impinging jets demonstrate substantially better validation of $6.88\,\%$ for h_{is} and $7.71\,\%$ for Δp_{t} with the same turbulence model. Because it was shown that the increased deviation of only the Tadpole's CFD validation cases is attributed to the uncertainty in ξ, the CFD model is deemed satisfactorily validated.

5.4.3 Flow domain illustrations

Total pressure, Mach number and static temperature contours are presented in Figure 5.5. The temperature contours show the heating of the flow along with a thermal boundary layer development in the adverse pressure gradient of the narrow flow region. The conjugate heat transfer characteristics are shown visually: the condensation heat flux conducts through the hemisphere, the flange and the annulus (to a lesser degree) to reach the convection domain.

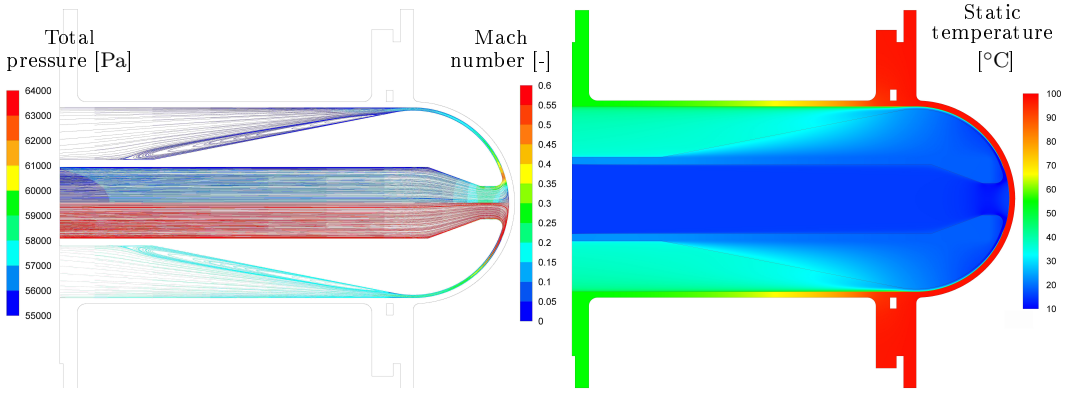

Figure 5.5: CFD pathlines showing the Mach number (left, top) and the total pressure (left, bottom) contours as well as the static temperature contours (right) for 12-C,ts at 'state 1' (the boundary conditions are given in Appendix G).

The characteristic total pressure and Mach number contours of a Tadpole configuration demonstrates that most of the total pressure losses occur in the adverse pressure gradient region, particularly the narrow flow region, where the sharpest reduction of Mach number occurs (this is echoed in the previously shown Figure 4.14). Because the change in total pressure is significantly sharper where the Mach number decreases instead of where the Mach number is highest near the walls, it is understood that, as with an impinging jet (Erasmus *et al.*, 2020*b*), skin friction plays a less important role in comparison with expansion losses in the Tadpole's domain of this investigation. This indicates that there is still room for improvement in the narrow flow region to reduce the rate of expansion with a non-hemispherical Tadpole surface such as a revolved spline. Reducing the rate of expansion here is expected to reduce the growth rate of the boundary layer and thereby should increase the heat transfer performance.

The total pressure pathlines also depict a narrow vortex occurring in the diffuser, thereby suggesting that a smaller expansion angle (and thus an increased diffuser length) may improve the domain. As described in Section 4.2.1, the maximum diffuser length was constrained in the experimental setup.

5.5 Conclusion

A CFD model based on the Four-Equation Transition SST turbulence model was developed and validated with the experimental results. The average (absolute) deviation between the model and the experimental results is 4.29 % for h_{is} and 22.9 % for Δp_{t} after four outliers were corrected. The model demonstrates satisfactory validation for both the Tadpole's flow domain and the impinging jet's flow domain. It was found that the greatest sensitivities to the CFD validation (besides the turbulence model) is ξ and k_{al}.

The results indicate that the performance of the Tadpole may be improved with a non-hemispherical Tadpole surface such as a revolved spline to constrain a near constant flow velocity in the narrow flow region. The CFD model can now be used to explore a variety of applications of the Tadpole, including its applications in the SCRAP receiver and the SUNflower receiver in the proceeding chapters.

Chapter 6

Applicability of the Tadpole within the SCRAP concept and a solar-hybrid Brayton cycle

This chapter explores the applicability of the Tadpole in the SCRAP receiver as well as the effect of this on the overall performance of solar-hybrid and pure solar Brayton cycles.

6.1 Introduction

It has previously been postulated that the improvement of the heat transfer and pressure loss characteristics of the SCRAP spike tip section should favourably contribute to the overall performance and lifespan of the receiver. This is expected to improve the coupled Brayton power cycle performance and thereby facilitate progress towards a lower $LCOE$.

The 1D SCRAP spike computational model developed by Lubkoll *et al.* (2020) (previously outlined in Section 1.2) will be used to investigate the application potential of the Tadpole within the SCRAP. Within the model, the spike is discretized into a series of sections along the path of the air flow. Each discrete cell has a characteristic heat transfer coefficient and experiences a pressure loss. The topology of the model is given in Appendix I. The SCRAP model considers the spike tip section as a single cell using characteristics obtained from high-temperature CFD simulations. The present study represents an initial estimate on the applicability of the Tadpole within the SCRAP concept and the tip section cell of the computational model is the scope of this study.

The model will be used to compare the impinging jet and the Tadpole using the metrics of the area-averaged local heat transfer coefficient (h_{local}) on the interior hemispherical heat transfer surface and the total pressure loss through the respective domains.

As an initial estimation of applicability, the integration makes the primary simplifying assumption of neglecting the heat transfer characteristics of the Tadpole's diffuser and the annular finned section integration. As part of a future layer of complexity, the diffuser integration with the finned section should be explored with a focused 3D CFD study.

The SCRAP computational model is verified using a data file from the computational model of Lubkoll *et al.* (2020) in Appendix I. The validated CFD models for both the impinging jet and the Tadpole will be used to obtain the high-temperature performance characteristics. These will be implemented into the tip section of the computational model and investigated at various operating conditions. Thereafter, the solar-hybrid gas turbine thermodynamic model from McDougall (2019) will be integrated with the receiver model to establish a new SCRAP operating condition and to estimate the system level performance benefit of the Tadpole.

6.2 Receiver integration

The improved SCRAP design presented in Lubkoll *et al.* (2020) employs an impinging jet with a 7 mm diameter. McDougall (2019) determined that the heat transfer and pressure loss characteristics affected by a jet with a diameter of around 12 mm results in a favourable thermodynamic efficiency for the Brayton cycle. In view of these observations, the present investigation will examine jet diameters of 7 mm and 12 mm and Tadpoles with the same nozzle-region diameter on the improved SCRAP design.

Multiple dimensional degrees of freedom in the Tadpole facilitate obtaining a favourable combination of heat transfer and pressure loss characteristics. To simplify the comparison with the impinging jets, the reference dimensions of the Tadpoles have been been chosen to demonstrate either: a similar h_{local} as the baseline impinging jets so that the total pressure loss can be compared or a similar total pressure loss so that h_{local} can be compared. These manifestations were iteratively created using the the previously developed kinematic and CFD models.

The dimensions of the reference Tadpole configurations for the SCRAP concept are given in Table 6.1. The 12-Tadpole,1 configuration was chosen for a similar h_{local} to a 12 mm impinging jet and the 12-Tadpole,2 was chosen for a similar total pressure loss. The 7-Tadpole was chosen for a similar h_{local} to a 7 mm jet. A second 7-Tadpole was not developed because, to match the pressure drop of the 7 mm jet, unfavourable supersonic flow develops.

The employed CFD model of the Tadpole was developed in Chapter 5 and corresponds in modelling parameters with the impinging jet model developed in Erasmus *et al.* (2020*b*). Inconel 718 is modelled for each solid cell zone. For the temperature dependent thermal conductivity of Inconel, the same piecewise linear model from Lubkoll (2017) is used.

Table 6.1: Dimensions of the high-temperature Tadpole configurations (dimensions depicted in Figure 3.1

Dimension	Unit	12-Tadpole,1	12-Tadpole,2	7-Tadpole
d_{n}	[mm]	12	12	7
r_{nose}	[mm]	3.5	3	4
r_{t}	[mm]	31.75	32.07	32.5
l_{c}	[mm]	0.5	0.5	0.5
l_{d}	[mm]	90	90	90
ξ	[mm]	0.03	0.03	0.079

The comparative spike tip heat transfer and pressure loss characteristics are shown in Figure 6.1. With a similar h_{local}: the total pressure loss reduction for the 12-Tadpole,1 is on average 53.2 %, and the pressure loss reduction is on average 40.5 % for the 7-Tadpole. With a similar total pressure loss: the 12-Tadpole,2 demonstrates an average increase in h_{local} of 17.6 %. The Tadpole therefore performs favourably as a heat transfer device when compared with an impinging jet at the high temperature of a solar receiver.

Table 6.2 comparatively presents the SCRAP performance characteristics from the 1D simulation model. The 'advanced gas turbine integration' cases represent the verified 1D model, further modified to incorporate the CFD results presented in Figure 6.1 and the new compressor outlet temperature and pressure boundary conditions yielded by the gas turbine model — which will be described in the next section. The spike mass flow rate was further modified to reach $T_{\mathrm{out}} \approx 800\,^{\circ}\mathrm{C}$ for the nominal baseline 12-jet case as a boundary condition.

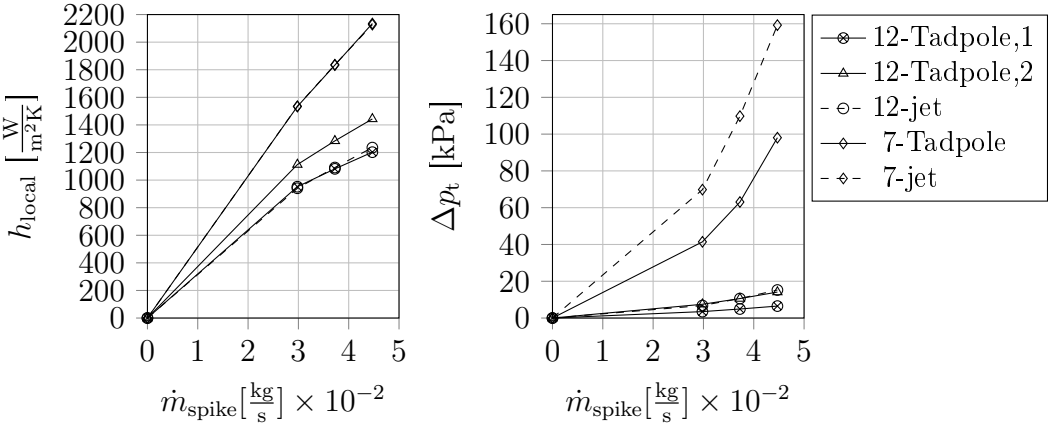

Figure 6.1: Comparison of the area-averaged hemispherical heat transfer coefficient (left) and the total pressure loss (right) between the CFD results of Tadpole configurations and corresponding impinging jet configurations at various operating conditions of the SCRAP concept.

Table 6.2: Progressive operating characteristics comparison of a SCRAP spike.

Parameter		Baseline[1]	Advanced gas turbine integration				
			7-jet	7-Tadpole	12-jet	12-Tadpole,1	12-Tadpole,2
$\dot{m}_{\text{spike}}$	$[\frac{\text{kg}}{\text{s}}]$	0.0352	0.037 25	0.037 25	0.037 25	0.037 25	0.037 25
T_{in}	[°C]	300	351	351	351	351	351
T_{out}	[°C]	815	806	806	800	800	802
$\overline{T_{\text{tip}}}$	[°C]	777	743	742	841	843	809
$\overline{T_{\text{root}}}$	[°C]	862	852	851	845	845	848
η_{th}	[%]	87.5	87.7	87.7	86.9	86.9	87.2
$\Delta p_{\text{t,spike}}$	[kPa]	12.3	113	65.8	13.2	7.47	13.2
$\dot{Q}_{\text{out}}$	[kW]	17.6	17.7	17.7	17.5	17.5	17.6

[1] Verified against Lubkoll *et al.* (2020) in Appendix I.

The SCRAP simulation model demonstrates that the significantly lower pressure loss affected by the 7-Tadpole and 12-Tadpole,1 configurations (from the corresponding impinging jets) corresponds to a substantial improvement on the overall SCRAP spike pressure loss — the 12-Tadpole,1 implementation depicts a 43.4 % lower SCRAP spike total pressure loss than the 12-jet implementation.

The improved h_{local} from the 12-Tadpole,2 implementation reduces the average spike tip outer surface temperature by 32.6 K from the 12-jet implementation. This material temperature reduction increases the spike air outlet temperature by 2.4 K and the spike thermal efficiency by 0.304 %. The reduced tip temperature creates a lower temperature gradient from the tip to the outer tube. This may facilitate safely reaching a higher air outlet temperature when considering the allowable creep and thermal stresses near the spike tip.

Figure 6.2 gives the temperature and pressure characteristics of the 12-Tadpole,1 implementation within the SCRAP concept. It is depicted that the temperature and pressure boundary conditions are modified from Lubkoll *et al.* (2020) to correspond with the Brayton cycle model's boundary conditions. It is illustrated that the receiver maintains a surface temperature below 850 °C. The expected peak stress state for the SCRAP concept is around 14.2 MPa (Lubkoll *et al.*, 2020). As was presented in Section 2.4.2, a typical Inconel material such as Inconel 800H ruptures at 24 MPa after 10 000 h at 870 °C. This indicates that the SCRAP concept could endure around 2.3 operational years with a safety factor of 1.6.

It is now of interest to explore the effect of the receiver performance improvement of the Tadpole on a coupled Brayton cycle's performance.

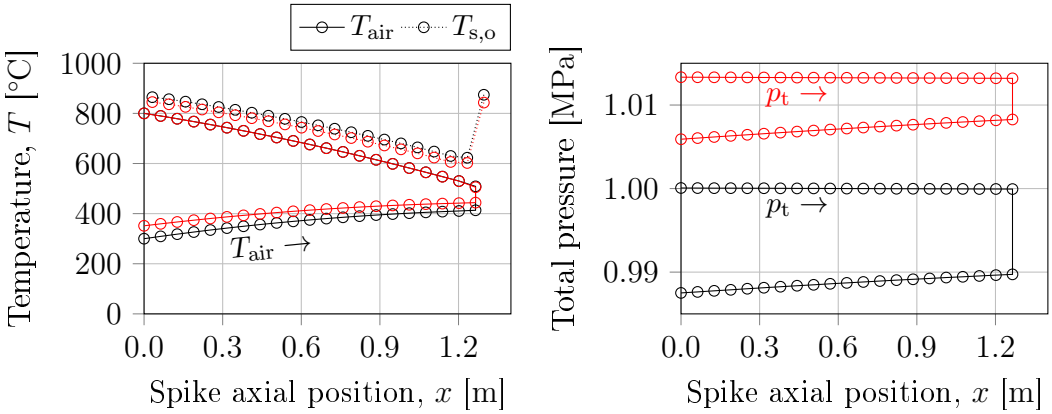

Figure 6.2: Distribution of a SCRAP spike's outer tube temperature, $T_{s,o}$, the air temperature, T_{air} (left) as well as the total pressure (right); results from Lubkoll *et al.* (2020) are shown in black and the advanced gas turbine integration with the 12-Tadpole,1 is shown in red.

6.3 Brayton cycle integration

McDougall (2019) developed a thermodynamic model that will be integrated into the present study to estimate the performance of a hybrid Brayton cycle that incorporates the SCRAP as a pressurized air pre-heater for a downstream combustion chamber. The model enables valuing both the performance metrics of a solar receiver (the efficiency and pressure loss) through the overall Brayton cycle thermal efficiency, $\eta_{th,Br}$.

The system diagram of the cycle is shown in Figure 6.3. Ambient air enters the Brayton cycle through the compressor inlet at $b1$, the compressed air then proceeds through the SCRAP to reach the pre-heated state, $b3$.

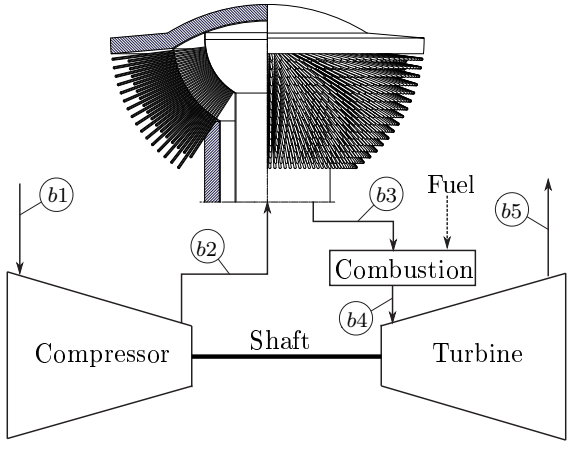

Figure 6.3: System diagram of the SCRAP concept hybrid Brayton cycle (adapted from McDougall, 2019).

The solar-heated air is then mixed with a hydrocarbon (or hydrogen) fuel and is combusted to reach a constant set point temperature state at $b4$. The working fluid finally advances through the turbine and exits at $b5$. The Brayton cycle boundary conditions are given in Table 6.3:

Table 6.3: Boundary conditions of the SCRAP Brayton cycle.

Parameter	Variable	Unit	Value
Ambient temperature	T_{b1}	[°C]	25
Ambient pressure	$p_{\text{b1,abs}}$, $p_{\text{b5,abs}}$	[kPa]	101.325
Input solar power	$\dot{Q}_{\text{in,spike}}$	$[\frac{\text{kW}}{\text{spike}}]$	20.16,[1]
Turbine inlet temperature set point	T_{b4}	[°C]	1027,[2]
Compressor pressure ratio	$\frac{p_{\text{b2,abs}}}{p_{\text{b1,abs}}}$	[-]	10,[2]
Hydrocarbon heat rate	Δh_{burn}	$[\frac{\text{kJ}}{\text{kg}}]$	43 100,[3]

[1] Lubkoll *et al.* (2020).
[2] McDougall (2019).
[3] Kerosene, Saravanamuttoo *et al.* (2001).

The Brayton cycle performance assumptions were estimated by McDougall (2019) and are retained for this analysis in Table 6.4. The specific heat capacity ratio used is 1.4 for the low temperature air (compressor) and 1.333 for the high-temperature air as well as the air and fuel mixture (turbine) (Saravanamuttoo *et al.*, 2001).

Table 6.4: Performance assumptions of the Brayton cycle (adapted from McDougall, 2019).

Parameter	Unit	Assumption
Isentropic compressor efficiency	[%]	85
Isentropic turbine efficiency	[%]	87
Shaft efficiency	[%]	99
Combustion efficiency	[%]	98
Combustion chamber pressure loss	[kPa]	6

Figure 6.4 demonstrates the Brayton cycle progression through the Brayton cycle states ($b1$ to $b5$) in the cycle. It is shown that the mass flow rate affects the receiver outlet temperature and pressure significantly, although the combustor reaches the set point temperature for all mass flow rates due to the set point boundary condition. Also evident is that the highest pressure losses are experienced by 7-jet and 7-Tadpole. From the perspective of the cycle pressure ratio, these losses weigh around an order of magnitude below the cycle pressure ratio.

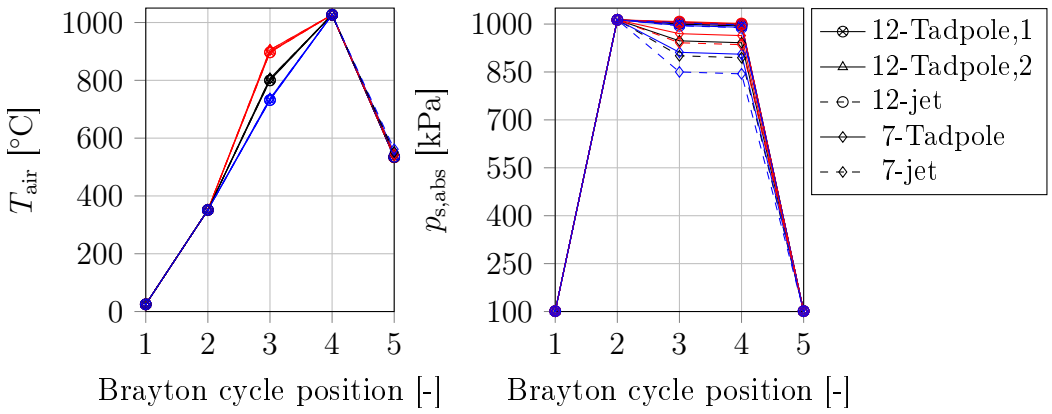

Figure 6.4: Comparison of the hybrid Brayton cycle temperature and pressure states (as depicted in Figure 6.3) at the nominal mass flow rate depicted in Table 6.2 (black), 20 % higher (blue) and 20 % lower (red).

Figure 6.5 presents the Brayton cycle performance characteristics of the SCRAP concept. The Brayton cycle performance is demonstrated with the overall efficiency[1] ($\eta_{th,Br}$), output shaft power and the specific fuel consumption (SFC). The pure solar case of no combustion is also explored, where the turbine expands from the output (temperature and pressure) state of the receiver outlet.

Many variables affect the Brayton cycle performance characteristics simultaneously, placing the heat transfer improvement of the Tadpole in perspective with other cycle components. It is shown that, for both the hybrid and pure solar cycles, the 12-Tadpole,1 and 12-Tadpole,2 configurations are marginally more efficient than 12-jet (a favourable nozzle diameter based on Brayton cycle efficiency as assessed by McDougall (2019)) for all mass flow rates.

The 53.2 % lower pressure loss from 12-Tadpole,1 translates to a Brayton cycle efficiency improvement from 30.68 % to 30.81 % and a 0.43 % reduction in specific fuel consumption. The increased receiver outlet temperature (2.4 K higher) of the 12-Tadpole,2 implementation from the 12-jet implementation results in a cycle efficiency improvement from 30.68 % to 30.78 % and a 0.91 % reduction in specific fuel consumption. The improvement for 7-Tadpole from 7-jet is more pronounced because the 7-jet is a less favourable impinging jet configuration. For this comparison, the cycle efficiency improves from 28.52 % to 29.73 % and the specific fuel consumption reduces by 4.1 %. Although the 7-Tadpole is less optimal than the 12 mm impinging jet and corresponding Tadpoles.

[1] The ratio of: the shaft output power and the input thermal power (constituting solar aperture irradiation and burnt fuel).

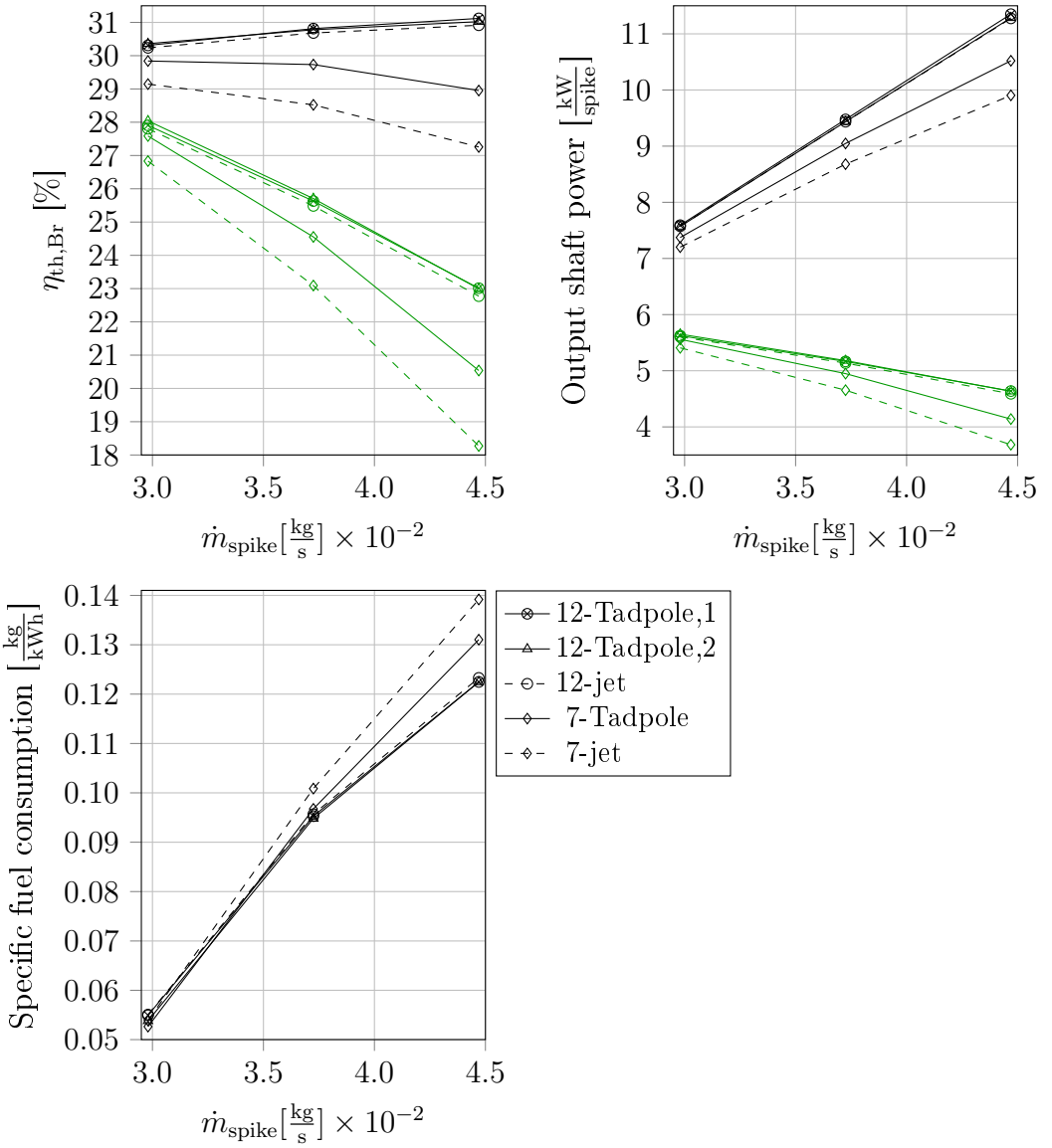

Figure 6.5: Performance comparison of the overall Brayton cycle efficiency (top left), the cycle output shaft power (top right) and the specific fuel consumption (bottom); the hybrid cycle is shown in black and the pure solar cycle with no combustion chamber, with $T_{\text{b4}} = T_{\text{b3}}$, is shown in green.

At the start of this study, it was expected that the initial estimate of the Tadpole's improvement on the Brayton cycle would be more pronounced on the 12 mm Tadpole. The Brayton cycle appears rather insensitive to an improvement on what was previously found to be a favourable trade-off between heat transfer and pressure loss characteristics for the impinging jet. It must be noted that this is an initial study, the study does not include an integration of the finned section with the Tadpole's diffuser (as shown in Chapter 1, Figure 1.7).

It is possible that this may further improve the performance value proposition for the Tadpole integration. The previous chapters describe potential improvements on the Tadpole which may lead to a further marginal performance improvement for the Brayton cycle.

6.4 Conclusion

The applicability of the Tadpole within the SCRAP concept was explored. The CFD results show that the Tadpole demonstrates favourable performance as a heat transfer device at elevated temperatures. The Tadpole demonstrated to be capable of increased heat transfer performance or increased pressure loss performance in relation to what was previously found to be a favourable impinging jet. Further, the Tadpole could be designed to achieve a favourable combination of performance characteristics.

The SCRAP simulation model shows that the pressure loss benefit of the Tadpole corresponds to a substantial 43.4 % reduction in the pressure loss of a SCRAP spike from what was previously found to be a favourable impinging jet. The Tadpole can also result in improved thermal absorption at the spike tip with a reduction in average spike tip temperature of 32.6 K for a similar spike total pressure loss. This improved thermal absorption may lead to an improved lifespan of the receiver.

The Brayton cycle performance investigation demonstrates that the pressure loss and heat transfer improvements translate to marginal improvements in thermodynamic cycle efficiency and specific fuel consumption. The improved total pressure loss of the 12-Tadpole,1 case from the 12-jet case results in a 0.13 % improvement in cycle efficiency and a 0.43 % reduction in specific fuel consumption. The improved outlet temperature of the 12-Tadpole,2 case from the 12-jet case results in a 0.10 % cycle efficiency improvement and a 0.91 % reduction in specific fuel consumption. It was also revealed that the 12-Tadpole,1 and 12-Tadpole,2 cases are more suitable than 7-Tadpole from the Brayton cycle perspective.

Chapter 7

Performance outlook on the SUNflower

The performance of the SUNflower, presented in Section 1.3.2, will be explored in this chapter. This chapter is pending journal submission in Erasmus *et al.* (2021*b*).

7.1 Introduction

The design of a new solar receiver involves many degrees of freedom. Significant considerations including the stress, dimensional scaling and fluid dynamics will first be explored, a reference design will then be chosen. To model the performance of the concept, a heliostat field and a suitable aiming strategy will first be developed to model the incoming concentrated irradiation. The resulting incoming flux distribution for a single characteristic SUNflower unit will then be extracted. A CFD investigation of this unit will follow to finally arrive at an initial performance outlook of the concept at various operating conditions. The SUNflower will be investigated here inclusively as a low-pressure and a high-pressure air receiver at various input flux magnitudes.

7.2 Reference design development

The overarching design considerations of the reference design are first detailed, thereafter the reference design is depicted. The considerations include: the mechanical stress, the dimensional scaling sensitivity as well as general fluid dynamics.

7.2.1 Mechanical stress considerations

A pressurized air receiver resists the gauge pressure of its heat transfer fluid at its elevated operating temperature where creep is pertinent.

It also experiences stresses from thermal gradients which will not be considered in this initial outlook.

Inconel 718 was chosen for this application because the thermal properties are well described in literature. As was previously depicted in Figure 2.2, it also has favourable creep strength characteristics. Appendix E contains the thermal properties. For Inconel in general, the ASME standard creep stress limit of 10 MPa at a temperature constraint of 950 °C will be enforced here(Swindeman and Marriott, 1994).

Of critical importance to satisfy this tough criterion is the stress occurring in the hemispherical dome. Dowling (2013) presents thick-walled pressure vessel equations for a hemisphere. Equation 7.1 gives the axial (σ_x) and hoop stress (σ_h) as a function of the radius, r:

$$\sigma_{x\ (r)} = \sigma_{h\ (r)} = \frac{p_g r_i^3}{r_o^3 - r_i^3}\left(\frac{r_o^3}{2r^3} + 1\right), \tag{7.1}$$

where r_i is the inner radius of the hemisphere and r_o is the outer radius. Similarly, Equation 7.1 gives the radial stress, $\sigma_{r\ (r)}$:

$$\sigma_{r\ (r)} = -\frac{p_g r_i^3}{r_o^3 - r_i^3}\left(\frac{r_o^3}{r^3} - 1\right). \tag{7.2}$$

Additionally, the dome region tensile stress caused by: firstly, the thrust generated in the Tadpole's nozzle region impacting onto the hemisphere and secondly, the outlet thrust of the Tadpole's narrow flow region (or diffuser inlet) can be accounted for through a linear momentum balance: $F_x = \dot{m}_{\text{unit}}(V_n + V_{nf,out})$, where V_n is the nozzle's outlet velocity and $V_{nf,out}$ is the narrow flow region's outlet velocity. Although this contribution to the overall stress is relatively small in comparison to that of the gauge pressure (for a high-pressure operating condition). Nevertheless, the force must be withstood by the dome and transferred through its base in the axial direction. The stress contribution over the base area ($\sigma_{x,F}$) is given in Equation 7.3:

$$\sigma_{x,F} = \frac{F_x}{\pi(r_o^2 - r_i^2)} \tag{7.3}$$

The peak 3D von Mises stress state can then be compared to the allowable creep stress to obtain a safety factor. It was found that the peak stress characteristically occurs on the inside of the hemisphere at the base in tension.

7.2.2 Dimensional scaling sensitivity

Considering the complexity of investigating and manufacturing a receiver based on hundreds of repeating units as shown in Garbrecht *et al.* (2012) and Kröger (2008), a solution may be to limit the number of repeating units in the SUNflower by maximizing the size of individual SUNflower units.

To understand the effect of increasing the outer-shell thickness (t_{os}), an example of Fouriers law of (1D) thermal conduction in spherical co-ordinates follows. Using an Inconel thermal conductivity of $25\,\frac{W}{mK}$[1] and an absorbed heat flux of $0.5\,\frac{MW}{m^2}$: the temperature drop over the outer shell follows $\frac{\Delta T}{t_{os}} \approx 20.03\,\frac{°C}{mm}$[2]. It is therefore important to maintain a minimal outer-shell thickness to reduce thermal losses caused by the temperature gradient through it.

An up-scaling sensitivity is now demonstrated for a constant operating gauge pressure and a constant outer-wall thickness to observe the peak von Mises stress with an increasing SUNflower hemisphere radius, r_o. The peak von Mises stress increases by $\times 3.67$ for a $\times 4$ increase in dimensional scale. Therefore, to withstand increased pressure stress, it will be required to up-scale t_{os} along with r_o to avoid high stresses.

It is demonstrated that up-scaling SUNflower units creates the concern of an increased gauge pressure stress with a thin wall thickness for a pressurized air receiver. Although, for a low-pressure air receiver, dimensional scaling is a less significant issue. The effect of the dimensional scaling of a SUNflower unit on the heat transfer performance will be explored later in Section 7.5.

Alternatively to up-scaling an individual unit, the number of SUNflower units along with the receiver aperture size can be increased or decreased to scale the receiver for a desired thermal requirement if a substantially uniform aperture flux distribution can be achieved — although this does not achieve the goal of reducing manufacturing complexity.

7.2.3 Input solar flux magnitude

A larger input flux density, $\dot{I}_{in}$, results in a larger thermal output for a relatively small receiver size. Along with a smaller surface area, the area from which thermal losses occur is also less. In support of this observation, it has been modelled that the CentRec particle receiver has seen an efficiency benefit with increased flux concentration from $0.2\,MW/m^2$ to $1\,MW/m^2$ (Wu *et al.*, 2015). However, because the metallic receiver of the present study requires thermal flux to move through its outer shell, the proportional temperature drop over the shell thickness is much greater with increased flux concentration. This creates a potential trade-off of an appropriate concentration. Accordingly, both a peak concentration of $2.5\,MW/m^2$ as well as half of this will be explored in this study to identify whether a significant sensitivity occurs due to flux concentration.

Previous experimental air receivers discussed in Chapter 1 were demonstrated at a thermal output power range between $0.4\,MW_{th}$ to $3.2\,MW_{th}$.

[1] For Inconel 718 at around 870 °C

[2] This calculation was conducted with an exterior curvature radius of 35 mm and differs from the flat plate calculation by 0.1 %.

The initial outlook on the SUNflower will therefore target a thermal output of $1\,\mathrm{MW_{th}}$ — a heliostat field will be developed around this target and an aperture diameter of 1 m is chosen for the tessellated structure.

7.2.4 Reference domain

The reference domain model will be isolated to only the heat transfer region of the concept. The inlet, the manifolds and the outlet of the receiver are thus excluded from the simplified model. These components will increase the overall pressure losses and contribute insignificantly to additional heat loss. The maximum dynamic pressure experienced in the heat transfer region of a SUNflower unit is around 6 orders of magnitude greater than that experienced in the excluded components. Total pressure losses are directly proportional to the dynamic pressure. This indicates that the excluded components represent negligible pressure losses.

It is also desirable to constrain the Tadpole's domain to develop a similar area at its inlet and outlet to develop similar dynamic pressures in these regions. This can avoid unnecessary expansion losses because the required area ratio over the diffuser is not unnecessarily large. The diffuser's expansion half angle will be conservatively small ($\theta_h = 6.5°$) because the suitability of a conservatively small diffuser half angle was discussed in Section 2.3.

Figure 7.1 gives the reference dimensions for a 30° sector of a SUNflower unit: this is the simplest representation to capture the geometry of the hexagonal tessellation structure in a unit. In Chapter 5. it was found that the Tadpole's domain can be improved with a revolved spline to more closely approximate channel flow. Accordingly, a spline was introduced here to reduce the rate of expansion in the narrow flow region. In Figure 7.1, the spline is constrained using three thickness dimensions through the progression of the narrow flow region. It is shown that the thickness reduces near the middle of the narrow flow region in order to substantially maintain the Mach number developed in the nose.

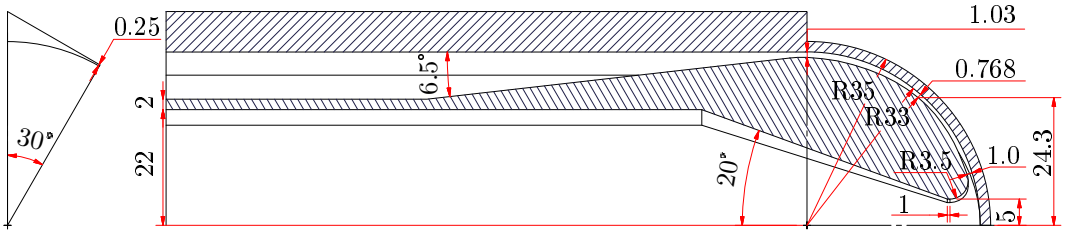

Figure 7.1: Dimensions (in mm) of the SUNflower's reference domain.

7.3 Heliostat field integration

7.3.1 Introduction

For a more holistic understanding of receiver operational performance, the exploration now expands to include the heliostat field.

The incoming solar flux distribution of a receiver can be largely uniform or non-uniform. The set of aiming points of the heliostats on the receiver, controlled by the aiming strategy, affects the receiver's flux distribution. Single point aiming causes a high peak flux magnitude on a receiver aperture with a weak flux gradient in the radial direction around its peak. A multi-point aiming strategy producing a uniform flux profile affects a more homogeneous receiver surface temperature distribution and reduced thermal stresses compared with a single aiming strategy (Sánchez-González and Santana, 2015). However, the corresponding relatively high flux density imposed near the edges of the aperture causes increased spillage losses when compared with single aiming.

If single aiming is implemented on the SUNflower, it would be necessary to model multiple repeating SUNflower units to incorporate effects such as net radiative heat transfer between the exteriors of units as well as the mixing of air flows from units with varying outlet temperatures — this kind of analysis was done by Craig *et al.* (2018*b*).

However, if an aiming strategy is employed to produce a uniform flux on the SUNflower so that the flux absorbed by each unit is similar then the net radiation and varying outlet temperatures between receiver units would be negligible. This firstly enables the receiver to achieve higher surface and outlet operating temperatures because the overall surface temperature distribution can be constrained nearer to the material's allowable limit without first reaching failure at the peak flux region of the aperture. Secondly it enables a simplified analysis of the receiver's performance because only a single repeating unit needs to be considered. The objective is thus to incorporate a heliostat field with such an aiming strategy to produce a relatively uniform flux distribution on the receiver.

7.3.2 Flux modelling

To develop the aiming strategy, the flux distribution from the heliostat field on a central receiver aperture must be modelled. This can be done using the Monte-Carlo Ray-Tracing (MCRT) approach or using a convolution-projection method.

A convolution-projection method consists of two operations. Firstly, the flux distribution produced by each heliostat on the image plane (receiver aperture) is determined by means of a Gaussian function resulting from the mathematical convolution of the solar intensity distribution from the sun (sun shape) and mirror surface slope error (σ_{slope}).

Secondly, the resulting image plane flux distribution is projected onto the discretized receiver surface.

Sánchez-González and Santana (2015) present a convolution-projection computer program called FluxSPT[3] requiring two orders of magnitude less computational time than MCRT. The code was validated with experimental data from the Plataforma Solar de Almería and the SolTrace MCRT software. The program was further used to investigate a multi-aiming strategy on a cylindrical receiver. This convolution model will be used to model the flux distribution on the SUNflower. This was enabled through a research collaboration with Dr. Sánchez-González at UC3M in Madrid which was made possible by the Erasmus+ program. The convolution model considers the following characteristic losses incurred by a heliostat field:

- Blocking: losses arising from neighbouring heliostats intercepting reflected radiation.
- Shading: arising from neighbouring heliostats intercepting incident radiation.
- Cosine: resulting from and increasing with the incidence angle of solar irradiation towards a heliostat.
- Reflectivity: associated with radiation absorbed by a heliostat.
- Attenuation: incurred in the traversed distance of reflected radiation through the atmosphere between the heliostat and receiver.
- Spillage: reflected radiation not intercepted by the receiver's aperture.

As discussed previously in Section 2.4.1, the receiver thermal efficiency does not include spillage, so it is considered here with the field losses.

7.3.3 Heliostat field

In an exploration to find an appropriate heliostat field for the SUNflower, it was found that a field containing small heliostats is better suited for a uniform flux aiming strategy because small heliostats produce small beam images on the aperture and so less spillage would be observed on the aperture compared to large heliostats. Examples of small heliostat implementations are: the Jemalong field (Cumpston and Coventry, 2017), the pilot plant in Daegu (Lee *et al.*, 2015), and a Heliopod manifestation (Domínguez-Bravo *et al.*, 2016).

[3]The program can be downloaded from http://ise.uc3m.es/research/solar-energy/fluxspt.

The Heliopod manifestation was chosen because the heliostat design parameters are available in (Domínguez-Bravo *et al.*, 2016). The Heliopod modelled here consists of six heliostats in a staggered formation, rigidly connected to form an equilateral triangle boundary containing four inner equilateral triangles with heliostats at the vertexes. The heliostat modelling parameters required to reproduce the results are given in Table 7.1.

Table 7.1: Modelling parameters of the heliostat field.

Parameter	Unit	Assumption
Mirror reflectivity	[%]	95
Sun shape	[-]	Circular Gaussian
Sun shape standard deviation	[mrad]	2.09,[1]
Surface slope error standard deviation (σ_{slope})	[mrad]	1.2,[2]
Geographic latitude (PS 10, Seville)	[°]	37.442 26
Solar direct normal irradiance (DNI)	$[\frac{\text{kW}}{\text{m}^2}]$	1

[1] Sánchez-González *et al.* (2018).
[2] Landman (2017).

7.3.4 The field layout development

The convolution model was used for iteratively improving the Heliopod layout. An oversized square layout was initially chosen. Single point aiming on the centre of the aperture was then simulated to determine the actual efficiency of each heliostat. From the results, an appropriate first row displacement was chosen and the Heliopods with the lowest optical efficiency were sequentially removed until the field size was appropriate. The layout parameters are given in Table 7.2. The SUNflower's tilt angle was chosen to approximate that of the previously discussed Tulip receiver (Doron, 2020). The tower height was optimized to reach a maximum single aiming overall field efficiency at equinox noon.

7.3.5 Aiming strategy

As discussed at the start of this section, a relatively uniform aperture flux distribution is particularly desirable for this receiver concept. A 1 m (diameter) discretized 2D circular aperture was used in the development of a new aiming strategy implementation. The implementation is called Blossaim[4] and is applicable for circular apertures and polar heliostat fields. The reader is referred to Appendix J for an overview.

[4]The development of Blossaim was a collaborative effort where Dr. Sánchez González contributed it's conception and conducted simulations on it's implementation.

Table 7.2: Layout dimensions of the heliostat field and receiver.

Parameter	Unit	Dimension
Heliostat		
Width	[m]	1.83,[1]
Height	[m]	1.22,[1]
Height from ground to reflective mid-point	[m]	1.5,[1]
Heliopod triangular boundary length	[m]	6,[1]
First row displacement	[m]	6,[2]
Count	[-]	1068
Receiver		
Aperture diameter	[m]	1,[2]
Tilt	[°]	32.5,[2]
Height	[m]	36,[3]

[1] Domínguez-Bravo *et al.* (2016).
[2] Design decision.
[3] Optimized for the given tilt angle.

The resulting Blossaim aperture flux concentration map is shown comparatively with a single aiming strategy (where all heliostats aim at the aperture's centre) in Figure 7.2. The dimensionless flux concentration depicts the ratio of aperture incident flux and DNI. The corresponding map of heliostat optical efficiency is shown in Figure 7.3. The Blossaim strategy achieves a relatively uniform flux distribution on the aperture with a 66 % reduction in the peak flux.

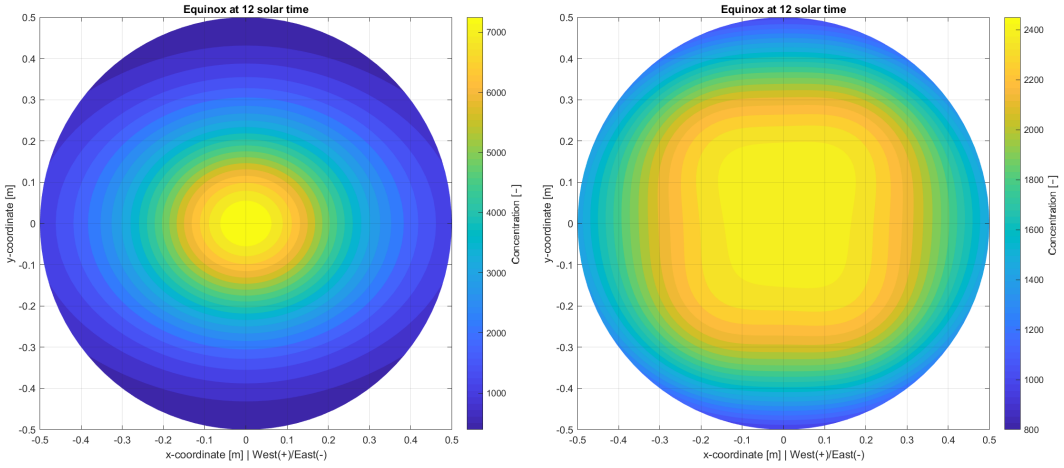

Figure 7.2: Comparison of flux distributions between single point aiming (left) and the Blossaim strategy (right) at 12 pm solar time during equinox.

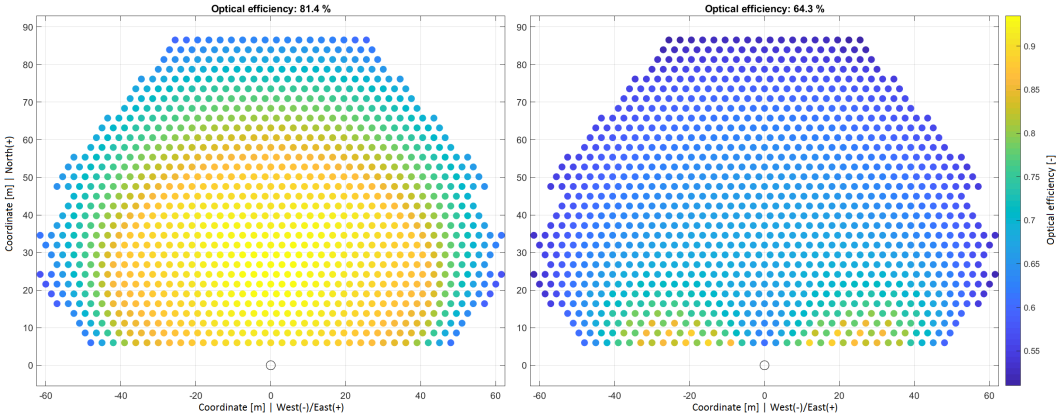

Figure 7.3: Optical efficiency distribution of the heliostat field for single point aiming (left) and the Blossaim strategy (right) accounting for the losses described in Section 7.3.

The deterministically arranged aiming points produce a flux distribution that is robust to a changing field optical efficiency distribution with solar time (Erasmus *et al.*, 2021*c*).

Table 7.3 shows the overall optical efficiency of Blossaim is 17.1 % lower than the single aiming strategy because of increased spillage losses from all heliostats aimed near the edge of the 1 m aperture. The spillage losses incurred by Blossaim can be reduced significantly by extending the acceptance aperture for the same aiming points as before. By opening up the aperture by 50 % to 1.5 m, the efficiency reduction with Blossaim becomes only 2 %. The idea is that a secondary reflector should be used (the petals of the flower) to extend around the 1 m aperture to 1.5 m or larger, capture the spillage and direct it toward the flux gradient region near the aperture edge.

Table 7.3: Comparison of field optical efficiency between a single aiming strategy and the Blossaim strategy for a 1 m aperture and an extended aperture with the previous aiming points.

Aperture diameter	Single aiming	Blossaim
1 m	81.4 %	64.3 %
1.5 m	88.6 %	86.6 %

7.3.6 Applying the convolution flux projection to the SUNflower's surface

On the absorber surface of the SUNflower, the hemispherical domes slightly shade incoming flux (from some heliostats) from reaching deeper regions of the receiver's exterior. The convolution-projection model accounts for this with a calculation on each discretized surface node which determines whether the node is blocked by another node[5]. These effects are demonstrated in a relative flux distribution from a single heliostat on an isolated central SUNflower unit (shown on the left) in Figure 7.4. The overall flux distribution is obtained from the superposition of the flux images from all the heliostats (shown on the right of the figure). The next step is to explore the unit's thermal performance using CFD by applying this flux as the heat source boundary condition.

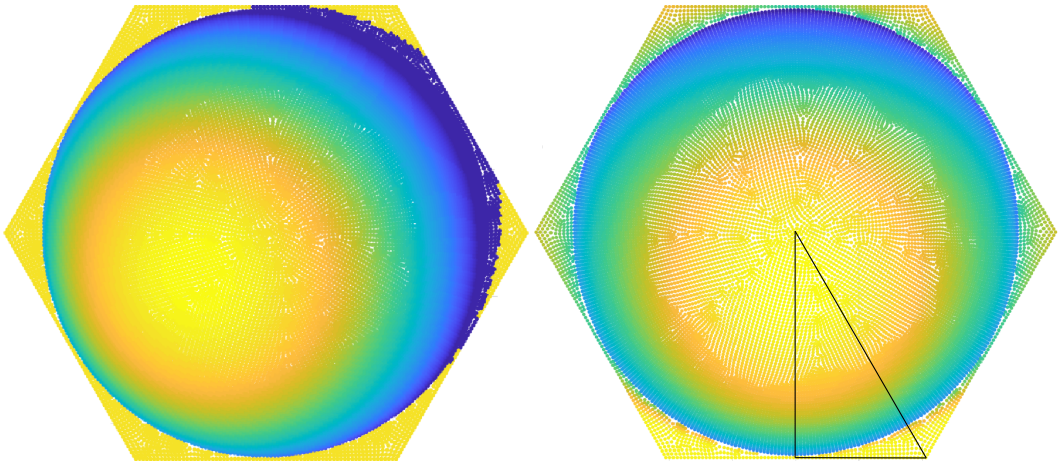

Figure 7.4: Relative flux image from a single heliostat (left) and from the entire field (right) on a central SUNflower unit with the selected region showing the reference heat source boundary condition to be interpolated into the CFD model.

7.4 CFD Modelling

7.4.1 Overview

The CFD flow domain is similar to the validation model described in Chapter 5. The main difference is that this model has a 3D domain with symmetry boundary conditions on the sides of the sector. The domain is further detailed in Appendix K. The previously validated Four-Equation Transition-SST turbulence model is employed.

[5]This contribution was made by Dr. Sánchez González.

The exterior surface in the reference design is coated with Pyromark 2500 paint. The emissivity and absorptivity are modelled. Concerning internal radiation modelling (between the Tadpole and the interior heat transfer surface), the emissivity of Inconel is applied. The thermal properties can be found in Appendix E.

It is required to apply the receiver's surface flux distribution from the convolution-projection model to the CFD model. The procedure presented by Slootweg *et al.* (2018) for the implementation of a heat source boundary conditions in ANSYS Fluent® is adopted here. The procedure permits modelling heat absorption into the receiver as well as radiative losses from its surface. The exterior heat transfer surface is given an arbitrary thickness — in this case 0.01 mm — to create a thin volume (cell zone). A volumetric heat source is then applied to this cell zone through a boundary condition profile file from the distribution as shown in Figure 7.4. The heat source profile is transported in a text file that contains a list of 3D surface co-ordinates along with the heat generation rate. Heat generation rate with a thin cell-zone is required instead of heat flux on a surface to enable flux to be absorbed through the receiver and also radiated outwards from it. Fluent® interpolates this heat generation rate distribution into the unit's exterior cell zone (as depicted in Appendix K).

The volumetric heat source method cannot account for reflected radiation from the receiver's surface. Therefore, an assumption must be made to model the reflective losses. The reflective losses from the incident aperture radiation can be approximated conservatively by assuming a relative loss of $1 - \alpha_{\mathrm{Pyr}}$, the inverse of the absorptivity of the Pyromark surface coating. This sets the upper limit of this loss to 5 %. This limit would apply for a flat plate absorber surface. However, the absorber of the SUNflower substantially traps reflective losses because parts of it's surface does not directly face ambient. Garbrecht *et al.* (2012) reported reflective losses of 1.3 % from their similar pyramidal receiver using the same absorptivity constant. The reflective losses are hence assumed as an average of these values: 3.15 %.

This leaves the radiative heat losses to be modelled. The exterior of the receiver's surface interacts with the sky and the ground through radiation. This is modelled with the DO model which is previously described in Chapter 5. A semi-transparent wall boundary with an external radiation temperature of 25 °C (and an emissivity and diffuse fraction of 1) is modelled at a small distance away from the exterior surface to represent the aperture. Between the aperture and the receiver's surface is a cell-zone through-which radiation can freely travel (as depicted in Appendix K). This zone has negligible thermal conductivity and is modelled as a solid. Net radiative heat transfer between receiver units is considered negligible because the units are assumed to operate at the same temperature in the initial performance outlook.

Heat loss through ambient convection is dependent on the cavity geometry as well as the operating temperature of the receiver. Correlations from Siebers and Kraabel (1984) show that ambient convective losses for cavity receivers

are relatively small. Natural and forced convection are neglected in the initial outlook because the scope is constrained to the heat transfer units instead of the cavity geometry.

A radiative thermal efficiency, $\eta_{\text{th,rad}}$, is defined which includes reflective and radiative emission losses:

$$\eta_{\text{th,rad}} = (1 - 0.0315)\frac{\dot{Q}_{\text{fluid}}}{\dot{Q}_{\text{fluid}} + \dot{Q}_{\text{rad}}}. \tag{7.4}$$

This expression is calculated in the Fluent® environment.

7.4.2 Computational considerations

The mesh is similar to the previously described one (depicted in Appendix H) in that the previous mesh was retained and revolved around its axis to make the 3D structured mesh.

To asses grid independence, a coarse mesh and a fine mesh containing 1.3×10^6 elements and 6.6×10^6 elements respectively were investigated with the fine mesh resembling about double the cell divisions of the coarse mesh. The solver settings were kept as in Appendix H except that Green-Gauss cell based spatial discretization was used for improved stability. After 6000 iterations, the air flow temperature change and the total pressure loss varies between the coarse and fine mesh by 0.910 % and 1.53 % respectively. Stable convergence on these results was also obtained and the peak y^+ value in the fine mesh convection domain was around 0.88. This assures confidence on the results of the fine mesh to be used for further calculations.

7.4.3 Uncertainty in the CFD domain

The uncertainty of the calculated radiation efficiency due to the symmetry boundary conditions in the simplified 3D domain shown in Appendix K is assessed. The symmetry boundary (characteristically receiving the highest re-radiative flux of the three symmetry boundaries) was replaced with the physical reflection of the outer shell with the temperature profile of the original surface while the exterior air domain and aperture boundary was extended over the reflected domain. The reflected temperature profile was iterated until its average temperature corresponded within 4 K of the original surface. This resulted in a 0.33 % reduction in efficiency and a 127 K (7.68 %) increase in average surface temperature. The reflection test case demonstrates that the symmetry boundary marginally affects the efficiency whilst creating a substantial uncertainty in the temperature of the outer shell. This test case represents the expected uncertainty of the proceeding results.

7.5 Results

The concept's capability of heating an air flow from 351 °C to approximately 800 °C was investigated at varying operating irradiation and pressure conditions. Figure 7.5 illustrates the heating of the air flow for the most favourable (high-pressure, low-flux) operating condition. The figure shows a peak in surface temperature at around midway through the narrow flow region — this is the same region where the Tadpole's revolved spline constrains the minimum thickness in the narrow flow region. The spline was introduced to mitigate the peak temperature here from previous CFD iterations.

The temperature of the Tadpole's volume is higher than the flow temperature as it is being significantly heated through internal radiation. A developing thermal boundary layer is accordingly observed on both surfaces of the narrow flow region and the surface of the inner tube and nozzle. The set of operating and performance characteristics of a SUNflower unit is shown in Table 7.4.

It was assessed that the thermal efficiency goal of 80 % was not achieved for any of the operating conditions. This is attributed to the exceedingly high exterior surface temperature ($\overline{T_{\text{es}}}$) causing high radiative heat losses. The high surface temperature also does not meet the 950 °C limit enforced in Section 7.2.1 although the peak von Mises stress remained under the limit as depicted in Table 7.4.

The lesson from these findings is that, although the convective heat transfer performance of the Tadpole is relatively high, the ratio of: the exterior surface area and the aperture area ($A_{\text{es}}/A_{\text{ap}}$) of the SUNflower concept is insufficient for this high flux and outlet temperature. Convective heat transfer is characteristically proportional to both the heat transfer coefficient and the convective surface area and therefore both parameters should be maximized for a most favourable design.

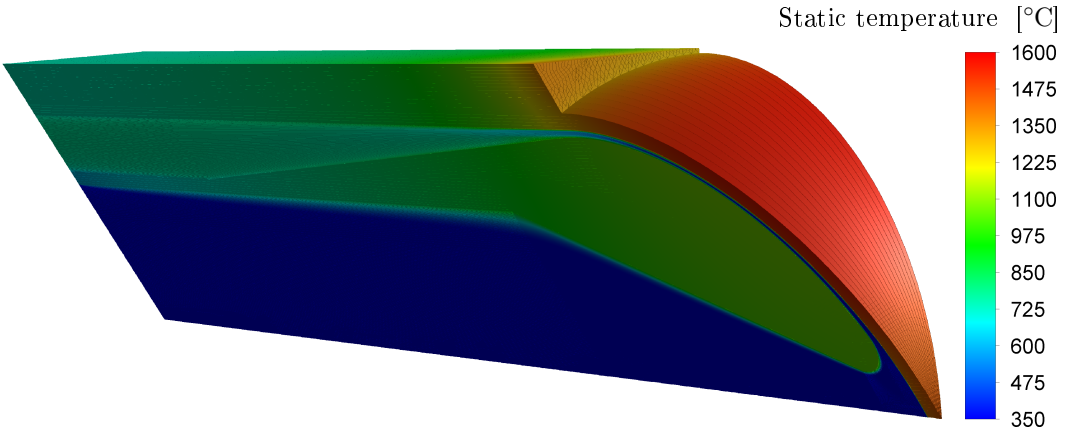

Figure 7.5: Temperature contour of the (high-pressure, low-flux) SUNflower unit showing the required exterior Inconel temperature to heat the air flow to 800 °C.

Table 7.4: Operating characteristics of the SUNflower unit cases: where 'H' and 'L' indicate high and low, 'P' and 'F' indicate pressure and flux and 'US' represents an up-scaling of ×4 in dimensions with the same outer-shell thickness.

Parameter	Unit	HP, HF	LP, HF	HP, LF	LP, LF	LP, LF, US
Boundary conditions						
$\dot{m}_{\text{unit}}$	$[\frac{\text{kg}}{\text{s}}]$	0.016 97	0.016 97	0.008 904	0.008 904	0.1030
$\dot{I}_{\text{in,max}}$	$[\frac{\text{MW}}{\text{m}^2}]$	2.53	2.53	1.27	1.27	1.27
T_{in}	[°C]	351	351	351	351	351
$p_{\text{out,abs}}$	[kPa]	1007.9	202.65	1007.9	202.65	202.65
Results						
T_{out}	[°C]	801.1	800.2	800.4	799.3	799.7
$\overline{T_{\text{es}}}$,[1]	[°C]	1691	1690	1383	1383	1498
$\eta_{\text{th,rad}}$	[%]	59.5	59.4	62.7	62.6	49.3
Δp_{t}	[kPa]	4.78	28.0	1.64	8.49	2.94
$\dot{Q}_{\text{out}}$	[kW_{th}]	8.44	8.43	4.45	4.44	51.7
$\sigma_{\text{VM,peak}}$,[2]	[MPa]	8.41	0.952	8.40	0.943	3.45

[1] Average hemisphere exterior temperature.
[2] Peak mechanical von Mises stress.

A small surface area ratio also leads to a large radiative view factor to ambient for losses to occur. Because of the small surface area, the air flow rate must be small to obtain the $\Delta T \approx 450\,°\text{C}$ to reach $T_{\text{out}} \approx 800\,°\text{C}$ causing a relatively low internal heat transfer coefficient compared to what the device can achieve at higher flow rates. For the SUNflower, the small exterior surface area is a limitation in the design.

The high-pressure, low-flux SUNflower can be compared with the SCRAP concept because they operate under the same aperture flux. The SCRAP concept has been predicted to perform at a significantly higher thermal efficiency and a lower exterior surface temperature in Chapter 6. Both the SCRAP and the SOLUGAS concepts make use of significantly larger exterior surface areas ($A_{\text{es}}/A_{\text{ap}}$) and achieve 800 °C at higher efficiencies.

Table 7.4 shows that the high-pressure test cases undergo significantly lower pressure losses than the lower pressure cases. For example, the HP, HF case shows a 82.9 % reduction in Δp_{t} from the LP, HF case. This suggests lower pumping losses for a high-pressure receiver. Although pressure losses are not the only variable affecting the pumping losses, it was hence sought to estimate the fluid pumping power loss. The power dissipation through a reduction in total pressure can be estimated using the Bernoulli equation from Çengel and Cymbala (2014); with the simplifying assumptions of 1D adiabatic incompressible flow: $P_{\text{loss,fluid}} = \dot{Q}\Delta p_{\text{t}}$ (where $\dot{Q}$ is the volumetric flow rate).

By this estimation, the HP, HF case shows a 96.3 % reduction in $P_{\text{loss,fluid}}$ from the LP, HF case. This indicates that the high-pressure air receiver experiences a significantly lower pumping loss for comparable thermal performance[6].

Table 7.4 further shows that the peak von Mises stress is much larger for the high-pressure cases and that it marginally increases with mass flow rate as a consequence of the tension caused by the fluid-body force. The effect of a $\times 4$ dimensional up-scale was explored for the LP, LF case (because this case can afford the additional mechanical stress). As shown in the table: the mass flow rate and the output thermal power increase by almost $\times 4^2$ to reach the same outlet temperature. However, the thermal efficiency decreases with a corresponding increase in exterior surface temperature.

7.6 Conclusion

It was found that the dimensional scaling of the SUNflower's heat transfer units is sensitive to material stress and the constraint of a thin outer-shell thickness does not permit a large internal volume for the units.

The Blossaim aiming strategy implementation was developed to produce a uniform flux distribution on a circular receiver aperture with a polar heliostat field. The implementation demonstrates promising performance by producing a relatively uniform flux distribution while reducing the peak flux magnitude by 66 % at an optical efficiency cost on an extended aperture of only 2 %. The deterministically arranged aiming points produce a flux distribution that is robust to a changing field optical efficiency distribution with solar time.

The SUNflower's capability to reach an outlet temperature of 800 °C was examined at various operating conditions. The initial outlook estimated a thermal efficiency of 62.7 % (excluding convection losses) and a total pressure loss of 1.64 kPa. The efficiency goal of 80 % was not achieved and the material temperature limit of 950 °C was exceeded.

The exploration of the SUNflower represents a lesson that a large internal heat transfer coefficient characteristic of an impinging jet or a Tadpole is not sufficient on its own to achieve the high outlet temperatures required in a receiver for the future of CSP. Instead, the ratio of exterior surface area to the aperture area of a receiver must also be maximized to enable absorbing a large aperture flux, achieve a high outlet temperature with a safe absorber temperature and a competitive thermal efficiency. Further development of the SUNflower is not recommended because concepts such as the SCRAP receiver are more promising.

[6]It must be noted that the adiabatic and incompressibility assumptions cause a large uncertainty. The average density was used for calculating $\dot{Q}$ through mass conservation. An uncertainty of 36.3 % is expected, attributed to the density variation (peak to average) through the domain. Because the relative error applies similarly for the compared cases, the comparison is deemed to hold for a rough estimation of power loss improvement.

Chapter 8

Summary

This chapter describes how the formulation of this thesis satisfies the research objectives and answers the research question. Thereafter, recommended further work is outlined.

8.1 Contribution

To satisfy the first research objective: Chapter 3 was formulated to describe the Tadpole's flow domain and design Tadpoles based on the kinematic distribution through the domain. Chapter 4 described an experimental investigation of the Tadpole which demonstrated that the Tadpole is capable of outperforming the conventional impinging jet as a heat transfer device. Multiple dimensional degrees of freedom facilitate obtaining a favourable combination of heat transfer and pressure loss characteristics. Chapter 5 describes a CFD model which can predict the performance of the Tadpole in a variety of applications. The Four-Equation Transition-SST CFD model was validated with the experimental results and demonstrated a deviation of 4.29 % for h_{is} and 22.9 % for Δp_{t} after four outliers were corrected. The CFD model also satisfactorily verified the kinematic model.

Chapter 6 aimed to satisfy the second research objective by exploring the application potential of the Tadpole within the SCRAP receiver together with a coupled Brayton cycle. The CFD model showed that the Tadpole demonstrates favourable performance relative to the impinging jet at the elevated operating temperature of the SCRAP receiver. The Tadpole demonstrated to be capable of increased heat transfer performance or increased pressure loss performance in relation to what was previously found to be a favourable impinging jet configuration. In comparison to the favourable jet, one Tadpole manifestation resulted in a 43.4 % reduction in the total pressure loss of the SCRAP spike and another manifestation resulted in improved thermal absorption with a reduction in the average spike tip temperature of 32.6 K. This improved thermal absorption may lead to an improved lifespan of the receiver.

However, these receiver performance improvements reflect marginally from the macro perspective of a Brayton power cycle. Improvements of less than 1 % are estimated for the cycle efficiency and the specific fuel consumption.

Chapter 7 exhibits a design exploration and an initial performance outlook on the SUNflower solar receiver to satisfy the third objective. A new aiming strategy implementation was developed and presented to develop a relatively uniform flux distribution with a low peak on the receiver. The implementation demonstrates promising performance by reducing the peak flux magnitude by 66 % at an optical efficiency cost on an extended aperture of 2 %. The SUNflower's capability of heating air to reach an outlet temperature of 800 °C was assessed with a 3D CFD model. The initial outlook estimated a thermal efficiency of 62.7 % (excluding convection losses) and a total pressure loss of 1.64 kPa. The receiver therefore does not achieve the thermal efficiency goal of 80 %. It was assessed that the relative exterior surface area compared with the aperture area (A_{es}/A_{ap}) is a limitation of the SUNflower. It is postulated that, in order to absorb a large aperture flux, achieve a high outlet temperature with a safe exterior surface temperature and a competitive thermal efficiency, the exterior surface area ratio of solar receivers should be maximized.

In answer to the research question, the Tadpole is a viable heat transfer device because it is a step forward from the prior art for application as a high flux heat transfer device. The device shows promise for improving the performance of the SCRAP concept. However, the SUNflower receiver is not satisfactory as a thermal receiver for heating air to 800 °C.

8.2 Further work

It is recommended that the inherent potential in the multiple degree design space freedom of the Tadpole's domain be explored with an optimisation study. To constrain a near constant velocity in the narrow flow region, a non-hemispherical Tadpole surface should also be investigated.

The SCRAP concept deserves further work to optimize the internal geometry to achieve maximal Brayton cycle efficiency, bounded by the operating temperature limits of the receiver. This can be conducted using existing impinging jet correlations in the current computational model. Thereafter, the full integration of the Tadpole and the finned annular section can be explored using a 3D CFD model containing a sector of the full spike.

Further work is also recommended on the Tadpole's applications in the bayonet tube heat exchanger and in gas turbine blade cooling. The Tadpole receiver was presented but not explored, the receiver has a more favourable relative heat transfer surface area than the SUNflower concept and could be investigated in a focused study.

Appendices

Appendix A

An outline of the Tadpole receiver

A dish collector developed by Wang and Laumert (2018) for a Brayton cycle was described in Chapter 2, Section 2.1. The Tadpole receiver shown in Figure A.1 is presented as a potentially improved parabolic dish receiver concept because it is expected that the Tadpole implementation produces improved pressure recovery.

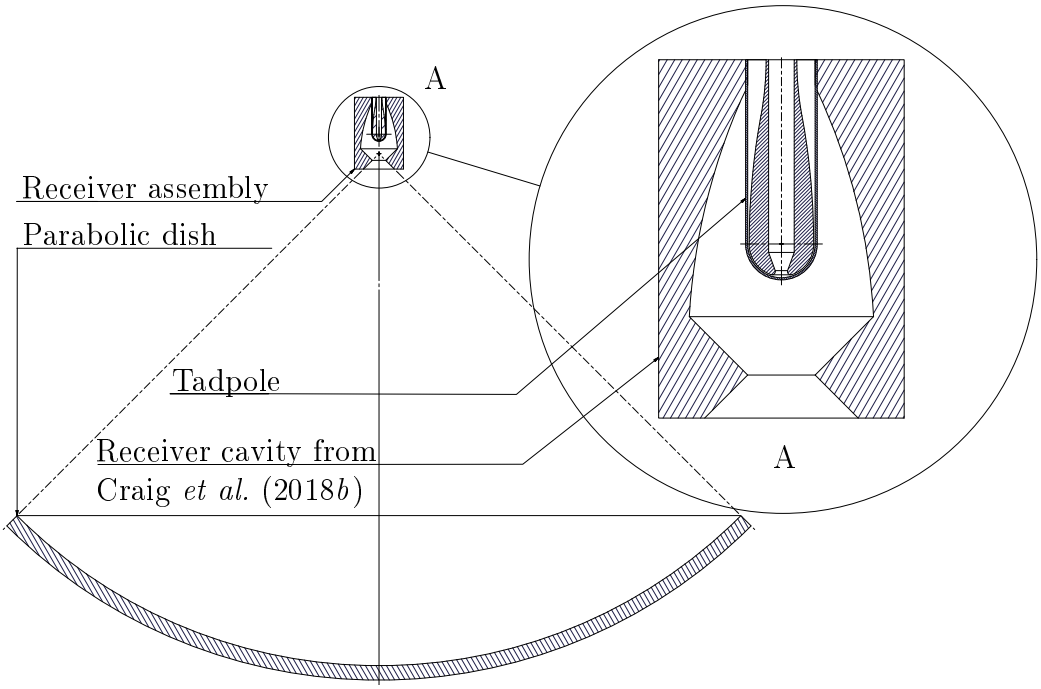

Figure A.1: A sectional view of the Tadpole parabolic dish receiver concept (adapted from Wang and Laumert, 2018).

This Tadpole manifestation forms a curved diffuser[1] which is expected to reduce the velocity and recover static pressure in the regions where less heat flux is directed to the thermal absorber. Moreover, the fluid velocity and the heat transfer characteristics are elevated in the region of the maximum radiation flux, near the aperture of the cavity. The cavity shape has previously been presented by Craig *et al.* (2018*b*) and explored by Slootweg *et al.* (2019). The purpose of the cavity is to trap concentrated incoming solar irradiation.

[1]The curve is formed with circular arcs along with tangent constraints imposed.

Appendix B

Geometric calculations

Geometric solutions for calculating the flow area are given here. The mathematical derivation and procedure for calibrating the axial position of a Tadpole prototype within an experimental apparatus are also detailed.

B.1 The non-concentric Tadpole frustum area calculation

The calculation procedure for obtaining the flow area within the non-concentric narrow flow region where $\xi > 0$ and $\xi < 0$ is first necessary. The referred dimensions are depicted in Chapter 3, Figure 3.1. The first task is to derive a geometric representation of the flow area as a function of α.

Figure B.1 demonstrates the frustum area approximation for non-concentric surfaces; the midpoint of the mean-pathline curve (shown in Chapter 3, Figure 3.2) is placed between the midpoints of the Tadpole surface and the heat transfer surface respectively. From this new midpoint, a line is drawn to intersect the pathline perpendicularly; the intersection between this line and the narrow flow region walls represents the flow area approximation.

It is necessary to define additional (accented) dimensions to account for the circular origins of the Tadpole, the inner surface and the mean pathline. r_{t} is the radius of the Tadpole surface from the origin of the hemispherical heat transfer surface; r_{t}' is centred from the origin of the Tadpole hemisphere; r_{t}'' is centred midway between the two (from which the pathline is drawn). The same convention is followed for the other variables. The flow area is calculated with Equation 3.1 (in Chapter 3) by using r_{i}'', r_{t}'' and α'' instead of r_{i}, r_{t} and α.

The calculation procedure is now outlined. The angle subtended between the tangential intersection of the nose section and the Tadpole (hemispherical) surface and the x-axis from the origin of the Tadpole hemisphere is:

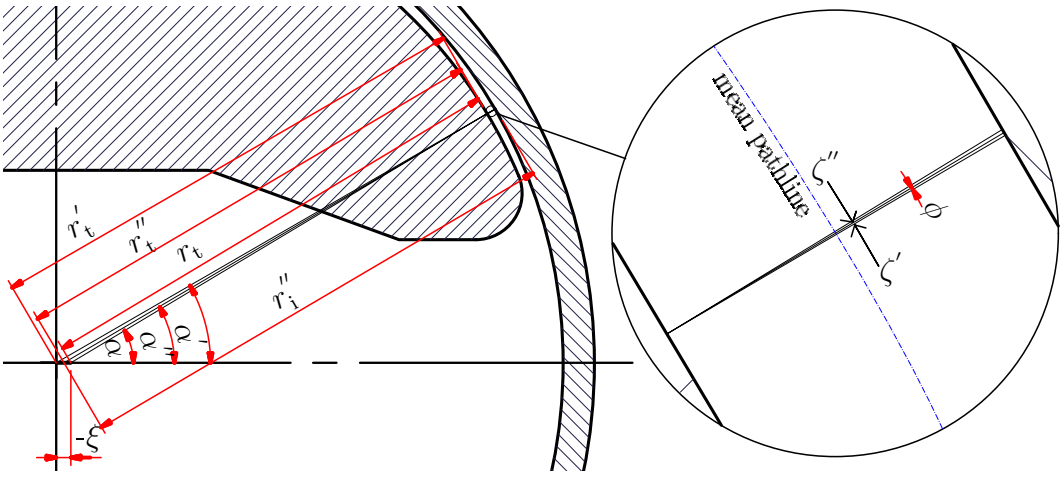

Figure B.1: Geometry of the narrow flow region — demonstrated in a negative ξ position.

$$\alpha_1 = \sin^{-1} \frac{d_\mathrm{n}/2 + r_\mathrm{nose}}{r_\mathrm{t} - r_\mathrm{nose}}. \tag{B.1}$$

This is the location of the first node of the narrow flow region, also known as the nose. The angle must also be known in terms of the origin of the hemispherical heat transfer surface (α'). This is calculated using the sine rule and holds for any α:

$$\alpha'(\alpha) = \sin^{-1} \left(\frac{r_\mathrm{t} \sin(\pi - \alpha)}{r'_\mathrm{t}}\right). \tag{B.2}$$

The initial first projected Tadpole radius is calculated from the cosine rule:

$$r'_{\mathrm{t},1} = \sqrt{r_\mathrm{t}^2 + \varepsilon_\mathrm{t}^2 - 2 r_\mathrm{t} \varepsilon_\mathrm{t} \cos(\alpha_1)}. \tag{B.3}$$

B.2 Implicit solution for $\xi > 0$

The node points are first defined in terms of α'. The general first projection of the Tadpole radius must be computed using the cosine rule, for any α':

$$r'_\mathrm{t}(\alpha') = \sqrt{r_\mathrm{t}^2 - \varepsilon_\mathrm{t}^2 + 2 r'_\mathrm{t} \varepsilon_\mathrm{t} \cos(\pi - \alpha')}. \tag{B.4}$$

This is an implicit calculation. The calculation converges quickly when using a previous (iteration) result as an input, with an initial value of r_t. Thereafter, α can be calculated using Equation (B.1). It is now necessary to calculate ϕ — the angle required to approximate the average projection (referred to as the

flow area line) perpendicular to both the boundary layers in the narrow flow region, α'':

$$\phi = \frac{\alpha' - \alpha}{2}, \tag{B.5}$$

$$\alpha'' = \alpha + \phi. \tag{B.6}$$

The frustum slant height that is parallel to r_t' is now required:

$$\zeta' = r_i' - r_t', \tag{B.7}$$

and the slant height projection to the line parallel to the flow area is:

$$\zeta'' = \zeta' \cos\phi. \tag{B.8}$$

Finally, again from the sine rule, the general second projection of the Tadpole radius is:

$$r_t'' = \frac{r_t' \sin(\pi - \alpha')}{\sin\alpha''}, \tag{B.9}$$

and the general second projection of the inner radius is:

$$r_i'' = r_t'' + \zeta''. \tag{B.10}$$

This is valid for any node in the narrow flow region between ${\alpha_1}' \leq \alpha' \leq 90°$. The flow area can now be calculated with Equation 3.1 (in Chapter 3) by using r_i'', r_t'' and α''.

B.3 Explicit solution for $\xi < 0$

In this situation, the area calculation procedure follows as a function of α instead of α', resulting in a simpler set of equations. Starting with α_1' as shown previously, the node points are defined in terms of α'.

The general first projection of the Tadpole radius can now be calculated explicitly:

$$r_t'(\alpha) = \sqrt{r_t^2 + \xi^2 - 2r_t|\xi|\cos(\pi - \alpha)}. \tag{B.11}$$

After r_t' is known, r_t'' can be worked out explicitly using Equations (B.5) - (B.10), with the exception that:

$$r_t'' = \frac{r_t \sin\alpha'}{\sin(\pi - \alpha'')}. \tag{B.12}$$

This is valid for any node in the narrow flow region between $\alpha_1 \leq \alpha \leq 90°$. The flow area can now be calculated with Equation 3.1 (in Chapter 3) by using r_i'', r_t'' and α''.

B.4 The calibration of the axial position

Because the flow behaviour is critically sensitive to a change in ξ, it is of interest to determine the most accurate ξ dimension with the experimental apparatus. This can be obtained after calibrating the Tadpole at a 'null' position by pushing the Tadpole and the (connected) nozzle assembly toward the interior heat transfer surface until the Tadpole and the surface make contact. At this position, a light permanent marking is made using a sharp knife at the point of communication between the nozzle assembly and the exhaust section (labelled as calibration marking in Chapter 4, Figure 4.3). It can be shown geometrically that when this occurs, the nose of the Tadpole (exactly where $\alpha = \alpha_1$) is touching the interior of the hemisphere. It then follows that in this position: $r'_{t,1} = r_i$. Hence, the null-projected angle is:

$$\alpha'_{null} = \sin^{-1}\left(\frac{r_t \sin(\pi - \alpha_1)}{r_i}\right), \tag{B.13}$$

where α_1 is calculated using Equation (B.1). Now, the displacement of the null position from the zero position (ξ_{null} — the position where the Tadpole and the HT surface make contact) can be calculated from the relationship of the exterior angle of a triangle and the sine rule. It follows that:

$$\xi_{null} = -\frac{r_t \sin(\alpha_1 - \alpha'_{null})}{\sin \alpha'_{null}}. \tag{B.14}$$

The desired position of experimentation on the inner tube must then be set and marked next to the calibration marking. The distance between this position and the zero position is $\Delta\xi$. It is now required to relate the measured distance between the desired marking position and the calibration marking to the true ξ position:

$$\xi = \xi_{null} + \Delta\xi. \tag{B.15}$$

This calculation procedure was validated geometrically using Autodesk Inventor®.

Appendix C

Kinematic model CFD verification

The kinematic model (developed in Chapter 3) is verified here with the CFD model (developed in Chapter 5) to asses whether the kinematic model's results are reliable to be used for designing experimental prototypes. Figure C.1 presents the kinematic characteristics through the domain following the mean (1D) pathline. The mean pathline in the kinematic model is illustrated in Figure 3.2 and the CFD model's partition is shown in Figure 5.1. It should be noted that there are minor differences in the pathline definitions near the nozzle region due to the structured CFD mesh constraints.

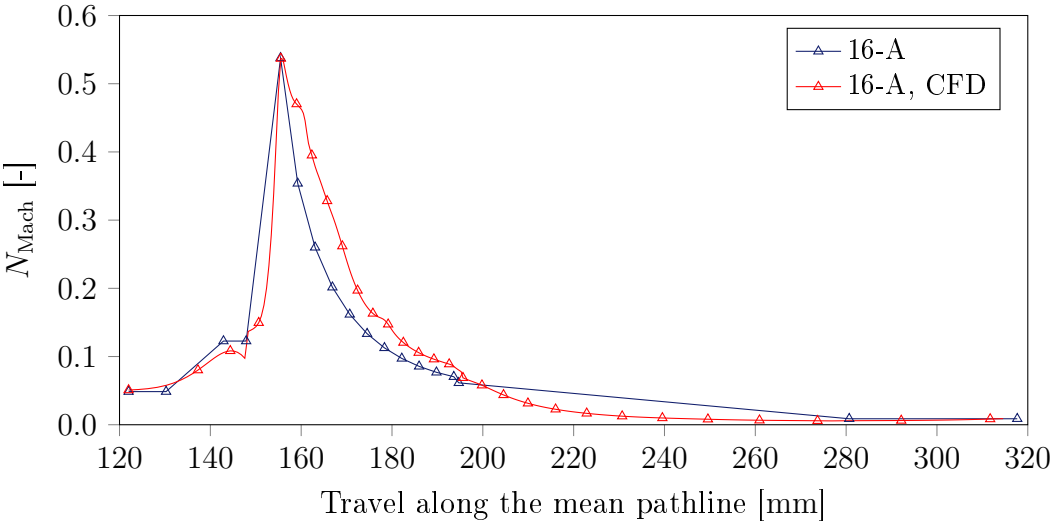

Figure C.1: Comparison of the kinematic model's Mach number development as a function of the mean (1D) pathline for a Tadpole configuration (blue) along with a CFD result (red) for verification.

It is depicted that the CFD model reaches a similar peak Mach number at the Tadpole's nose. Between the models there is a minor deviation near the stagnation region caused by the flow in the CFD model being repelled by a locally elevated pressure, a non-linear sudden spike in velocity then occurs at the nose (in the CFD model). Both models demonstrate non-linear deceleration in the narrow flow region, although here the CFD model deviates substantially with a higher Mach number — it is understood that this is primarily affected by the substantial adverse pressure gradient boundary layer accelerating the mean pathline flow in the CFD model while the kinematic model neglects boundary layer modelling. The variation could also be influenced by thermal effects such as expansion cooling or the heating of the flow in this region.

Because the kinematic model can satisfactorily reproduce the kinematic behaviour of the CFD model, it demonstrates to be a reliable tool to design Tadpole prototypes.

Appendix D

An overview of the steam generator

During the course of this research project a steam generator was designed, manufactured and commissioned. The purpose of the steam generator is to supply heat to the experimental apparatus in order to explore the heat transfer characteristics of the Tadpole prototypes.

D.1 Overview

A brief description of the design process will now be given. The steam generator consists of a stainless steel cylindrical vessel as shown in Figure D.1. A cylindrical vessel was chosen to minimize incurred material cost and welding time. An outer cylindrical shell covers 40 mm of foam insulation to avoid thermal losses. The insulated vessel remains hot for more than a day after reaching boiling temperature. The vessel can provide two simultaneous steam streams with differential flow rate control. It can also provide a third stream if the dedicated inlet is also used. The commissioned steam generator is presented in Figure D.2.

The steam generator nominally supplies almost 6 kW of steam at 100 °C. It currently contains three 2 kW heating elements. The steam generator can supply 9 kW of steam if three 3 kW heating elements are retrofitted. The heating elements are located 120° apart around the vertical axis with a vertical offset to avoid the elements touching each other as shown in Figure D.3.

The device has been designed to draw power from a 16 A three-phase supply to ensure a reliable power connection. Each heating element draws power between one of three phases and a neutral bridge as shown in Figure D.3 (during a preliminary electrical test run on the exposed inner vessel). This enables a 220 V relative connection per element. The figure shows the neutral bridge linking the blue (neutral) cables from the elements and the three-phase switch linking the colour (phase) cables. The power to the steam generator

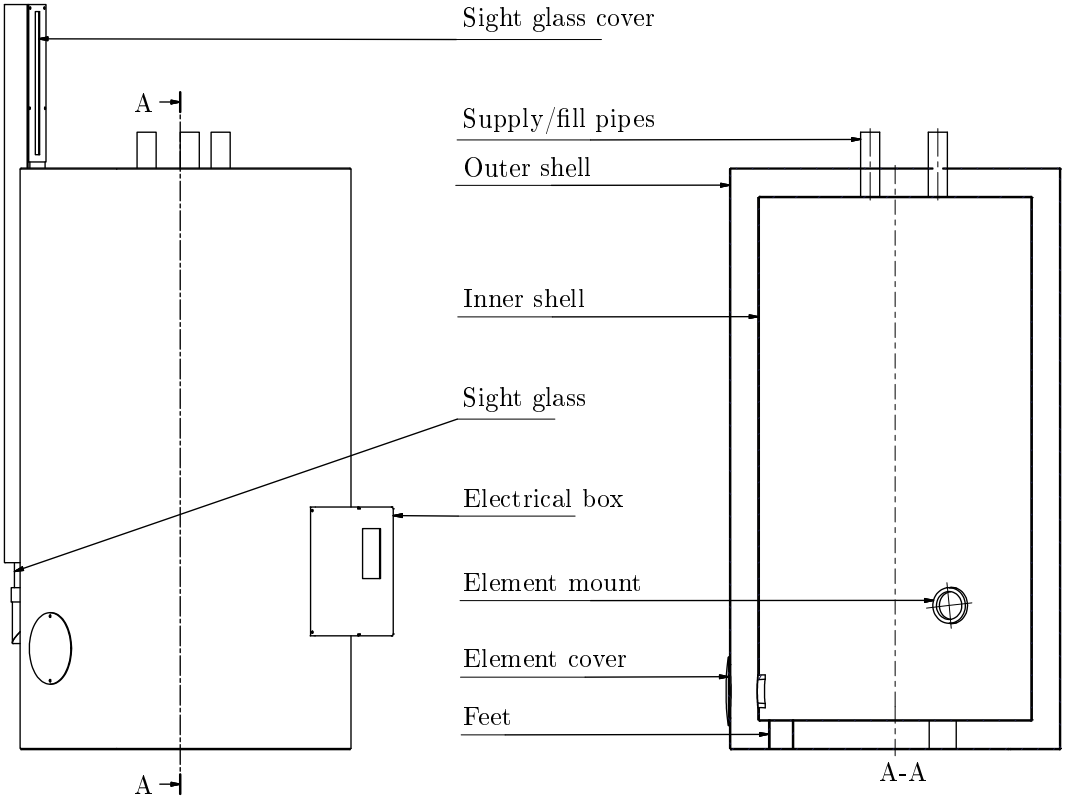

Figure D.1: Overview of the steam generator.

can be controlled at an electrical box on the side via a three-phase switch. The steam generator can also operate at three equal electrical load increments by switching individual phases on and off.

The total volume of the steam generator is 84.2 litres. At the maximum indicated level, the total usable volume is around 50 litres. This is sufficient to supply 6 kW of steam to the experimental apparatus for about 6 h — this is more than the amount of time required for a full uninterrupted test of a Tadpole prototype configuration. The steam generator has a sight glass to indicate the water level. The sight glass is open at the top to avoid significant pressurization of the vessel. The gauge pressure within the vessel does not exceed 10 kPa and the temperature does not exceed 101 °C. According to the SANS 347 pressure vessel standard (SABS, 2012), this falls within the not regulated region for a dangerous/non-dangerous liquid and gas — the vessel is inherently safe.

The steam generator also has three other ways to vent pressure, including two pipe feeds that are both open to atmosphere and one additional pressure release (filling cap). A small differential height of 24 mm is seen between the sight glass level and the actual water level inside the boiler during normal operation. This naturally occurs to provide a small pressure header to move

Figure D.2: Design of the steam generator: the foam insulation between the cylinders is shown (left); the exterior is shown as seen from the electrical box (middle) and the exterior from the sight glass side is shown (right).

the steam through the supply pipes. It is for this reason that the sight glass is substantially extended above the top of the vessel. It must be noted that the steam generator should be switched off when the water level reaches the maximum indicated operational level to avoid overflowing.

D.2 Operating Instructions

1. Inspect the steam generator for leaks. Look especially for cracks in the sight glass. Inspect for tampering or missing covers.

2. Open the filling cap. Fill the vessel to a level between the indicated 'minimum fill' and 'maximum fill'. Close the filling cap.

3. Switch the steam generator on, move the blue switch upwards. Ensure the lab's three-phase power supply is off. Unroll the extension lead. Connect the three phase cable to the lab supply and switch it on after it has been connected. This is to ensure a reasonable distance between the operator and the steam generator when initially switching it on in case of a short-circuit. However, the steam generator should be safe to touch

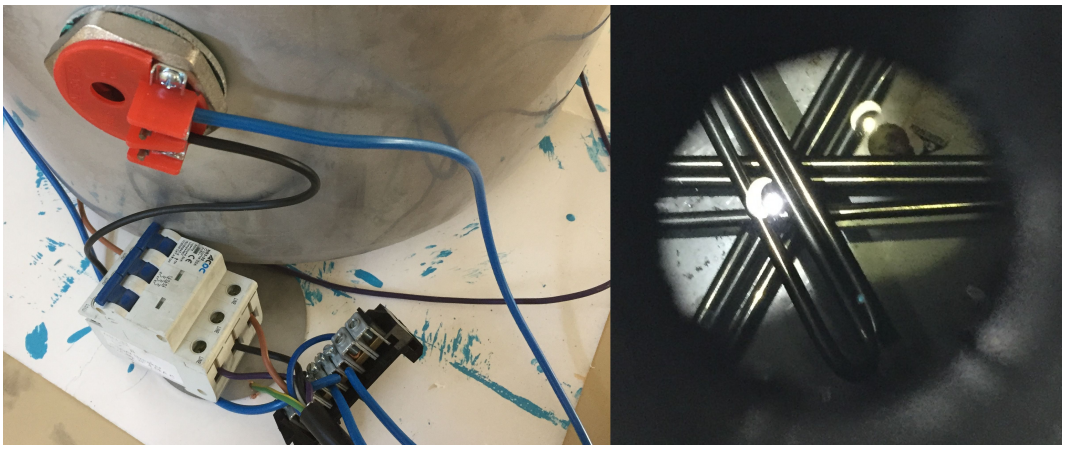

Figure D.3: Electrical components of the steam generator: the division and control of each electrical phase to supply the heating elements is revealed during an electrical test run (left) and a view (from a steam supply feed) of the heating elements is shown (right).

during operation as it is well grounded. Do not let the steam generator run unattended.

4. The steam generator should take about an hour to heat up. When the steam starts generating, ensure that there are no steam leaks from the vessel and the valves aren't leaking steam. If they are, switch off the machine and tighten/seal the connections.

5. Continuously ensure that the sight glass level does not drop below the 'minimum operating' level. Switch it off and refill if this occurs. This is to avoid damaging the top heating element.

6. The differential steam supply between the two supply pipes can be controlled by the control valve. Do not tamper with the control valve unless you are calibrating the steam lines. They have been positioned in such a way as to maximize the steam flowing into the steam bath while also allowing sufficient steam through the steam jacket to create a repeatable condensation reading.

7. When testing is completed, Switch off the steam generator and the three-phase supply switch. Wind up the extension lead and the steam generator lead and store the extension lead securely. Winding up the cable is important to be certain that the steam generator is off. This is critical because, if it is not switched off, the elements inside the steam generator may eventually melt down.

Appendix E

Fluid and material properties

This appendix holds the reference values of the material and fluid properties.

E.1 Experimental processing and validation

Empirical correlations by Lubkoll (2017) from the VDI Heat Atlas VDI (2010) were used to obtain μ and c_p of dry air during the processing of the mass flow rate in the experimental results. For the CFD model, correlations also based on VDI (2010) developed by McDougall (2019) for μ, c_p and k were used.

For the kinematic model of Chapter 3 and the post-processing of the experimental and CFD results (heat transfer coefficient and Nusselt numbers): constant air properties were assumed. The constant properties were interpolated from (VDI, 2010) at the average operating temperature and pressure of the flow domain in the experimental apparatus.

Because the exploration of the domain was conducted at steady-state, the heat capacity of the solid parts is not required. The conductivity of the 3D printed Tadpole prototypes was modelled by considering the Tadpole as a porous structure composed of air and Acrylonitrile Butadiene Styrene (ABS) plastic with a porosity, ε, of 50 %. The Maxwell-Eucken equation for porous media (Eucken, 1940) was used to approximate the effective thermal conductivity of the prototypes:

$$k_\mathrm{eff} = k_\mathrm{s}\frac{k_\mathrm{f} + 2k_\mathrm{s} + 2\varepsilon(k_\mathrm{f} - k_\mathrm{s})}{k_\mathrm{f} + 2k_\mathrm{s} - \varepsilon(k_\mathrm{f} - k_\mathrm{s})}. \tag{E.1}$$

Where k_s and k_f are the thermal conductivities of the solid and fluid respectively. The thermal conductivity of the aluminium parts was found to vary less than 0.5 % due to the operating temperature range within the experimental apparatus, and was thus assumed constant.

The emissivity characterizes the radiation heat losses from the receiver surface. Based on its shiny appearance, the internal heat transfer surface of the hemispherical dome in the experimental apparatus was approximated

by polished aluminium at 100 °C with regards to radiation emissivity. The emissivity and thermal conductivity of 3D printed ABS plus was assumed to be the same as moulded ABS because of a lack of such data in literature.

E.2 High-temperature applications

The thermal conductivity of Inconel 718 and Incoloy 800H alloys are given in Figure E.1. Variable conductivity was modelled.

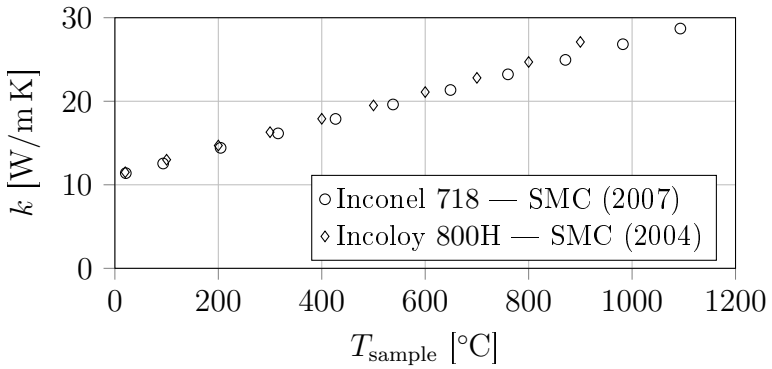

Figure E.1: The thermal conductivity of Inconel 718 and Incoloy 800H (adapted from Lubkoll, 2017).

The emissivity of Inconel 718 is given in Figure E.2. It can be observed that the emissivity does not vary significantly between the range of 500 °C and 800 °C therefore, the average emissivity in this range (0.841) is used for the SUNflower's internal radiation modelling.

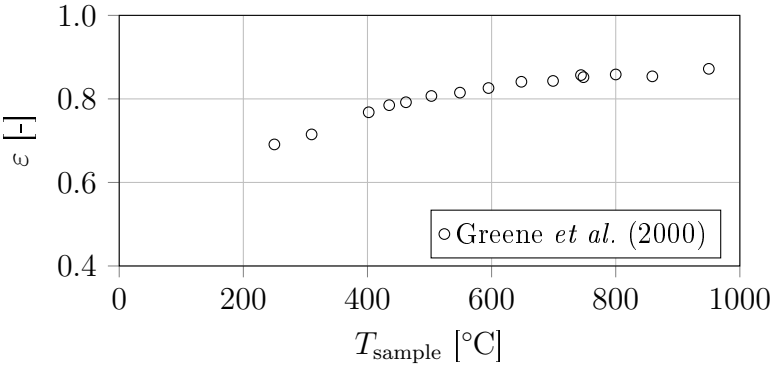

Figure E.2: The thermal emissivity of Inconel 718 (adapted from Lubkoll, 2017).

E.3 Reference values

The constant reference values for the air and steam are given in Table E.1 and Table E.2.

Table E.1: Air properties.

State	μ $[\frac{\mathrm{kg}}{\mathrm{m\,s}}]$	c_p $[\frac{\mathrm{kJ}}{\mathrm{kg\,K}}]$	k $[\frac{\mathrm{W}}{\mathrm{m\,K}}]$
$5\,\mathrm{bar_{abs}}$, 33 °C	18.873×10^{-6},[1]	1.0129,[1]	0.026941,[1]
$10\,\mathrm{bar_{abs}}$, 550 °C	38.121×10^{-6},[1]	1.1054,[1]	0.058562,[1]

[1] VDI (2010).

Table E.2: Saturated steam properties.

State	ρ_l $[\frac{\mathrm{kg}}{\mathrm{m^3}}]$	ρ_v $[\frac{\mathrm{kg}}{\mathrm{m^3}}]$	h_fg $[\frac{\mathrm{kJ}}{\mathrm{kg}}]$	μ_l $[\frac{\mathrm{kg}}{\mathrm{m\,s}}]$	$c_\mathrm{p,l}$ $[\frac{\mathrm{kJ}}{\mathrm{kg\,K}}]$	k_l $[\frac{\mathrm{W}}{\mathrm{m\,K}}]$
$1\,\mathrm{bar_{abs}}$, 100 °C	957.9,[1]	0.5978,[1]	2.257,[1]	2.83×10^{-4},[1]	4.217,[2]	0.6676,[2]

[1] Çengel and Boles (2014).
[2] VDI (2010).

The constant reference values for the materials are given in Table E.3.

Table E.3: Material properties.

Material	k $[\frac{\mathrm{W}}{\mathrm{m\,K}}]$	ε [-]	α [-]
ABS	0.1575,[1]	0.95,[2]	0.95,[7]
ABS, porous	0.081756,[3]	0.95,[2]	0.95,[7]
Aluminium 7075-T6 (26 °C)	128,[4]	0.095,[2]	0.095,[7]
Inconel 718 (648 °C)	[-]	0.841,[5]	0.841,[7]
Pyromark 2500 (967 °C)	[-]	0.9,[6]	0.95,[6]

[1] MatWeb (2019).
[2] Mikron Instrument Company (2003).
[3] Equation E.1.
[4] Fives North American Combustion (2001).
[5] Greene *et al.* (2000).
[6] Garrido *et al.* (2019).
[7] Kirchhoff's law of thermal radiation was assumed.

Appendix F

Experimental procedure

This chapter details the experimental procedure followed to obtain the heat transfer and pressure loss characteristics of the experimental Tadpole prototypes.

1. Inspect the apparatus for damage and problems. Ensure that the apparatus is fully assembled and safe to operate. Check all flexible and solid pipes to ensure that they are fastened properly. Check the pressure tap fittings.
2. Blow through the outlet silencer and the steam-chamber outlet pipes to ensure that there are no particles in the pipes that can cause steam pressure to build.
3. Zero measurements of the pressure and temperature are taken. Obtain the ambient pressure from the barometer in the Mechanical Engineering building.
4. The apparatus safety valve is opened, thereafter the laboratory inlet safety valves are opened — this ensures that there is no sudden pressure accumulation inside the system. The air-supply system is now activated.
5. Before the steam generator is switched on. An ambient-temperature pressure test is executed: the air pressure is increased in 0.3 bar (gauge static pressure) increments until a maximum of 7 bar is reached. The pressure is held constant at each increment for 5 min. The system is continuously inspected for leaks and loose pressure tap fittings. During this step, the voltage reading on the differential pressure transducers must be monitored. In the event that the voltage reading on any pressure transducer exceeds 60 mV, the test must be stopped to avoid damaging the transducers. Thereafter, the air pressure is switched off and a zero reading is taken. This concludes

the ambient-temperature pressure test; the heated system test follows next.

6. The steam generator is switched on and allowed to reach operating temperature — within approximately 60 min. The operating instructions of the steam generator described in Appendix D must be followed. The temperature inside the steam bath (T_8) is monitored.
7. After T_8 reaches 100 °C, the pressure is increased for six 0.5 bar increments and three further 1 bar increments and kept constant at each increment for 20 min. Air temperature and pressure measurement averages are taken only over the last 10 min of each 20 min increment when steady-state is reached — this is checked by observing that the outlet and annulus flange temperatures are constant with time. After the first 9.5 min of each increment the condensate collector is emptied and replaced. Thereafter the condensate is allowed to accumulate for exactly 10 min and weighed on a scale for each increment. The steam bath temperature and the steam generator water level are continuously observed. The apparatus is monitored for steam and air leaks, especially near the pressure taps. During this step, the voltage reading on the differential pressure transducers must again be limited to 60 mV.
8. The steam generator is switched off. The laboratory air supply is then switched off and zero readings are finally taken to be able to observe if a change has occurred in the ambient measured temperatures and pressures.
9. The experimental setup air supply is then switched off. Thereafter, the experimental setup safety valve is closed and locked.
10. Ensure that all air-supply valves are closed, the power to the steam generator is off and the plugs are also disconnected.
11. Empty the condensate collector and clean up the accumulated condensate around the setup and on the floor under the steam generator.

Adapted from Erasmus (2018), page 22.

Appendix G

Experimental validation boundary conditions

Table G.1 and Table G.2 present the boundary conditions for the Tadpole and impinging jet experimental validation CFD simulations. The ξ values for the simulation states were interpolated or extrapolated based on the mass flow rate and the ξ_{low} and ξ_{high} values from the ambient pressure tests (as detailed in Section 4.2.1). Experiments were conducted at $p_{\text{abs,atm}} = 101.35\,\text{kPa}$.

Table G.1: Boundary conditions and variables for the CFD Tadpole validation simulations.

Parameter	Unit	16-A[1]	16-B[1]	12-B	12-C,ts	8-B
State 1						
$\dot{m}_{\text{in}}$	$[\frac{\text{kg}}{\text{s}}]$	0.015 13	0.013 62	0.016 28	0.016 12	0.011 72
T_{in}	[°C]	28.39	31.84	18.40	24.83	21.28
T_{es}	[°C]	98.68	98.84	97.90	97.94	97.99
$p_{\text{g,out}}$	[kPa]	54.18	48.91	55.36	57.45	35.37
TI_{in}	[%]	4.244	4.300	4.205	4.210	4.381
TI_{out}	[%]	5.021	5.087	4.975	4.981	5.184
ξ	[mm]	-0.3904,[2]	0.3048	0.1838	0.03,[2]	1.118
State 2						
$\dot{m}_{\text{in}}$	$[\frac{\text{kg}}{\text{s}}]$	0.044 41	0.059 64	0.059 98	0.0442	0.019 25
T_{in}	[°C]	27.18	32.01	18.30	26.02	21.68
T_{es}	[°C]	96.17	95.94	93.36	94.86	96.76
$p_{\text{g,out}}$	[kPa]	218.1	309.0	302.4	215.4	73.27
TI_{in}	[%]	3.709	3.575	3.573	3.711	4.118
TI_{out}	[%]	4.389	4.230	4.227	4.391	4.872
ξ	[mm]	-0.43,[2]	0.4601	0.5881	0.174,[2]	1.172
State 3						
$\dot{m}_{\text{in}}$	$[\frac{\text{kg}}{\text{s}}]$	0.086 54	0.1199	0.1169	0.092 12	0.032 63
T_{in}	[°C]	26.09	35.58	22.21	25.59	23.47
T_{es}	[°C]	93.30	93.26	89.10	90.94	94.87
$p_{\text{g,out}}$	[kPa]	465.0	657.4	633.5	493.2	148.7
TI_{in}	[%]	3.413	3.276	3.287	3.386	3.855
TI_{out}	[%]	4.038	3.876	3.889	4.006	4.561
ξ	[mm]	-0.5892	0.6636	1.115	0.3417	1.268

[1] This is the only physical prototype that contains a straight diffuser as depicted in Figure 4.6.
[2] This value corresponds to the corrected CFD result.

Table G.2: Boundary conditions for the jet CFD validation simulations.

Parameter		16-jet			12-jet		
		State 1	**State** 2	**State** 3	**State** 1	**State** 2	**State** 3
$\dot{m}_{\text{in}}$	$[\frac{\text{kg}}{\text{s}}]$	0.013 65	0.046 87	0.089 06	0.014 80	0.041 87	0.080 30
T_{in}	[°C]	21.30	19.02	17.18	19.90	17.96	16.08
T_{es}	[°C]	98.68	95.73	92.67	98.23	94.79	90.43
$p_{\text{g,out}}$	[kPa]	43.39	224.3	467.8	46.67	196.3	419.2
TI_{in}	[%]	4.299	3.684	3.400	4.256	3.737	3.445
TI_{out}	[%]	5.086	4.359	4.023	5.035	4.421	4.076

Appendix H

Computational considerations

This appendix details the solver settings, relaxation, mesh generation, grid independence study and convergence investigation of the ANSYS Fluent® CFD model. The Stellenbosch University High Performance Computer (HPC) and the Centre for High Performance Computing (CHPC) were employed for CFD computations using a Text User Interface (TUI) approach. More information on submitting a TUI file to a cluster can be found in McDougall (2019).

H.1 Discretization and solver settings

The Coupled pressure-velocity scheme was found to be robust and versatile for this domain. For spatial discretization: Green-Gauss node-based was used for the gradients; second-order was used for pressure; second-order Upwind was used for the energy equation, density, momentum, turbulence kinetic energy and turbulence dissipation rate; finally, the first-order Upwind scheme was used for intermittency and the Discrete Ordinates model.

It was found that the solver often diverges without high-order-term relaxation as the second-order terms in the transport equations may render the solver unstable. The second-order terms were opted for here for improved numerical accuracy. The default relaxation parameters suggested by Fluent® worked satisfactorily. Moreover, the pressure and momentum equations were relaxed with a factor of 0.5 while for energy and density, 1 was used.

The radiation Discrete Ordinates model can be tuned to increase its accuracy and computational cost by increasing the discretization resolution — the divisions and pixels of θ_{DO} and ϕ_{DO}. The default parameters were used in the validation simulations of Chapter 5 and finer accuracy was specified in the high-temperature application cases[1]. Table H.1 gives the chosen settings of the model.

[1]It was determined that the performance characteristics of Chapter 5 are not sensitive to refinement from the default DO model settings.

Table H.1: Discrete Ordinates radiation model parameters.

Parameter	Chapter 5	Chapter 6 and Chapter 7
θ_{DO} divisions	2	3
θ_{DO} pixels	1	3
ϕ_{DO} divisions	2	3
ϕ_{DO} pixels	1	3
Energy iterations per radiation iteration	10	4

H.2 Mesh generation

An example axisymmetric validation mesh is shown in Figure H.1.

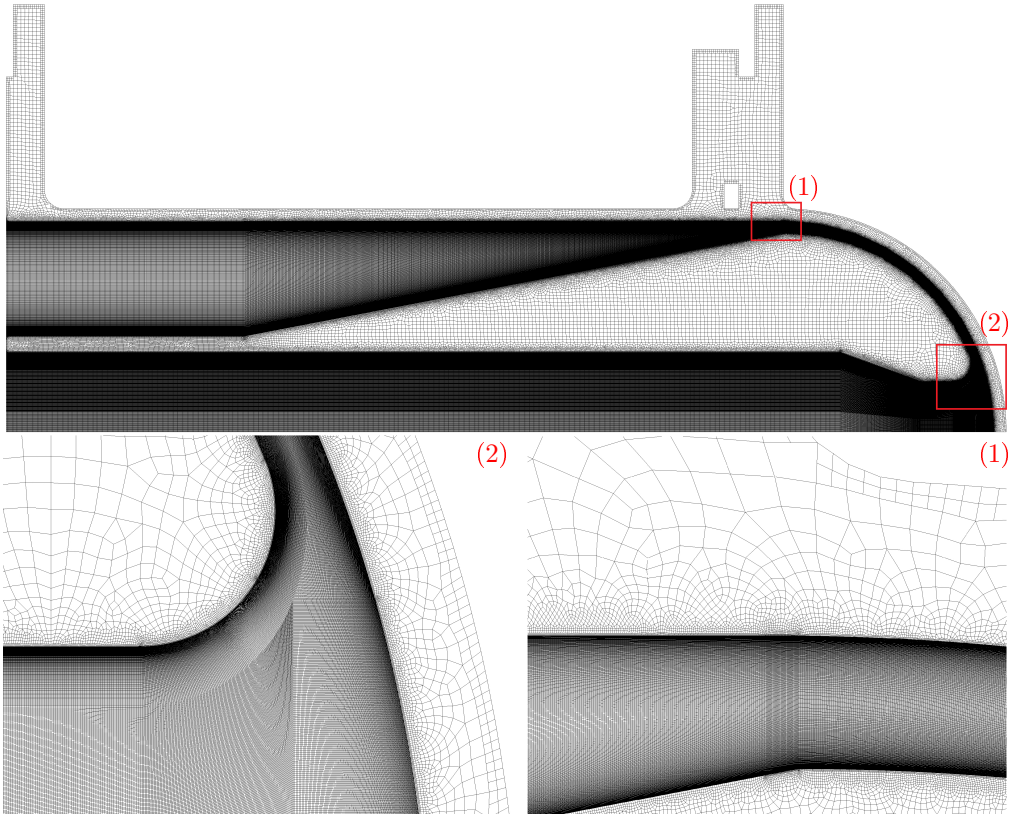

Figure H.1: Mesh with enlarged sections of a typical axisymmetric validation case.

The convection flow domain was partitioned (as shown in Chapter 5, Figure 5.1) so that a fully-structured mesh could be generated. The structured grid enables resolving fine detail within the domain as well as robust grid independence. The convection structured mesh scales for all prototype configurations. A high resolution is not required within the conduction domain (solid and porous materials) because conduction temperature gradients are linear in these regions so it was resolved by quadrilaterals with a minimum face size of 0.6 mm.

H.2.1 Grid independence

A grid independence study was conducted for the validation mesh with the largest cell size for the structured mesh region (convection domain) — the 16-B[2] mesh and the boundary conditions used correspond with the largest experimental validation mass flow rate and thereby the largest anticipated y^+ value. The performance characteristics were monitored while changing the mesh resolution. The grid dependence results are shown in Figure H.2.

It is demonstrated that the heat transfer coefficient and the total pressure loss converge at 0.25 % and 0.58 % respectively between the two most fine meshes. This convergence is sufficient because it is well below the experimental uncertainty. The mesh with around 1.8×10^6 nodes is the chosen mesh. In the narrow flow region, there are 120 divisions perpendicular to the flow direction and 1000 divisions parallel to the flow direction. For the LRN turbulence models, the wall condition of $y^+ \approx 1$ (Bredberg, 2000) was achieved for all simulations after additional near-wall refinement in some meshes.

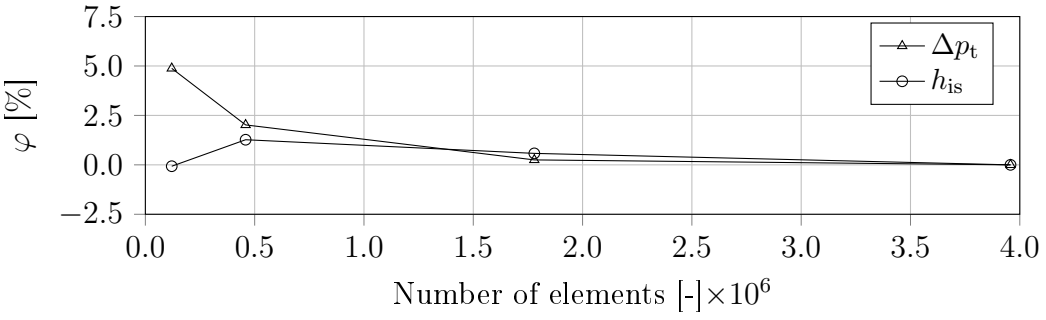

Figure H.2: Deviation of the performance characteristics from that of the finest computational mesh over the number of elements in the mesh.

[2]The naming convention was detailed in Section 4.2.1.

H.2.2 Convergence

The convergence criterion on the normalized residuals was set to 10^{-6} for all equations, with the exception of 10^{-12} for the energy equation. However, a few simulations did not achieve this level after 15 000 iterations. To ensure that the achieved convergence levels are acceptable, the oscillation in the characteristic parameters for the weakest convergence data points was observed for an additional 2000 iterations. The mean and the maximum relative convergence instability amplitudes of h_{is} and Δp_{t} are shown in Table H.2.

Table H.2: Weakest converging CFD data points of the validation Tadpole and jet configurations described in Chapter 4.

Test	Data point	Peak N_{Mach}	Continuity residual	Energy residual	Maximum deviation: h_{is}	Maximum deviation: Δp_{t}
12-C	2	1.22	1.18×10^{-2}	1.67×10^{-7}	4.46 %	0.687 %
16-A	1	0.569	3.78×10^{-3}	1.11×10^{-8}	2.64 %	8.34 %
8-B	1	0.578	1.35×10^{-2}	2.37×10^{-8}	1.73 %	5.16 %
8-B	2	0.844	4.67×10^{-3}	4.16×10^{-9}	0.599 %	0.647 %
12-jet	2	0.38	3.39×10^{-3}	2.06×10^{-9}	0.0247 %	0.114 %

The second data point of the 12-C simulation demonstrated the weakest convergence. This iterative instability indicates that the Tadpole is unstable near the transonic and supersonic realms and that it could perhaps be better understood with a transient simulation in a future study. The data points in the table were corrected with iteration-averaged results over the final 2000 iterations. For all subsonic validation cases not shown in Table H.2, the 8-B serves as the weakest convergence uncertainty — this convergence level is satisfactory because it is well below the experimental sensor uncertainty.

Appendix I

Topology and verification of the SCRAP simulation model

The discretization of the 1D SCRAP simulation model (developed by Lubkoll *et al.* (2020)) is shown in Figure I.1. The single node in zone III of the spike tip is the scope of this study. The model is verified here for its use in Chapter 6. Lubkoll *et al.* (2020) presents an improved design for the SCRAP spike based on a sensitivity analysis on the initial reference geometry, the improved geometry given in Table I.1 is used for verification.

The verification attempt of the temperature and pressure characteristics along the one-dimensional flow path is depicted in Figure I.2. The verification attempt demonstrates increased heating at the tip with a substantially lower tip temperature, decreased heating in the finned section and lower pressure losses in the finned section. At the same mass flow rate, the outlet temperature is 15.3 K (1.43 %) higher, the total pressure loss is 2.50 % lower and the thermal efficiency is 0.806 % higher. It is understood that the observed variations will not significantly affect a relative comparison between an impinging jet and the Tadpole and therefore the model is deemed satisfactorily verified.

Table I.1: Improved design of the SCRAP concept from Lubkoll *et al.* (2020) (dimensions depicted in Chapter 3, Figure 3.1).

Dimension	Unit	Verification model
d_{n}	[mm]	7
r_{i}	[mm]	33
t_{os}	[mm]	2
d_{it}	[mm]	39
t_{it}	[mm]	2
Fin tip width	[mm]	1
Spike length	[mm]	1300

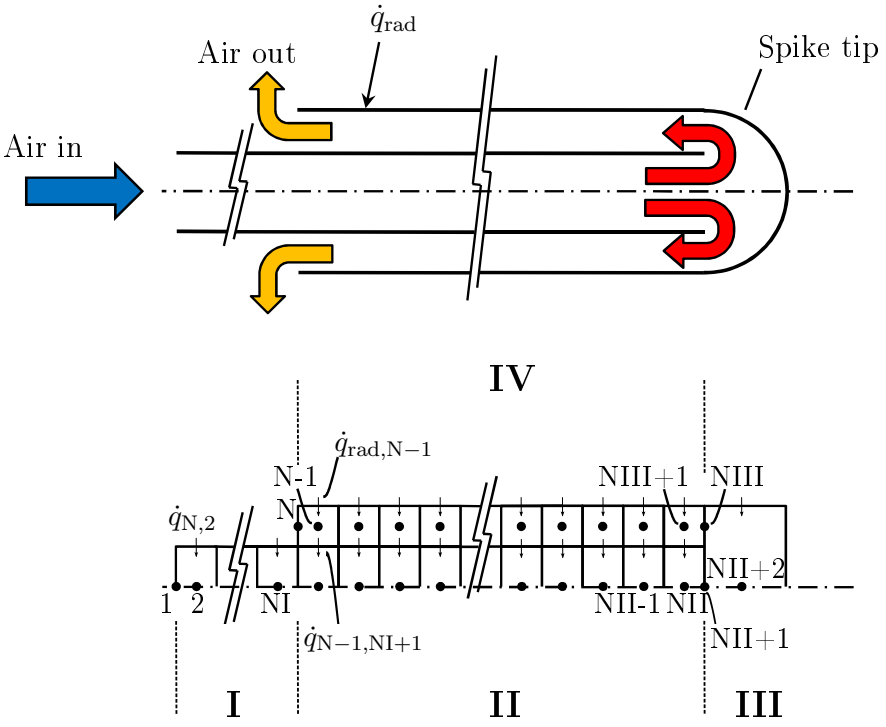

Figure I.1: Topography of the SCRAP spike simulation model: the inner tube is depicted in zone I and zone II, zone III contains the spike tip and the finned annulus is depicted in zone IV (adapted from Lubkoll, 2017).

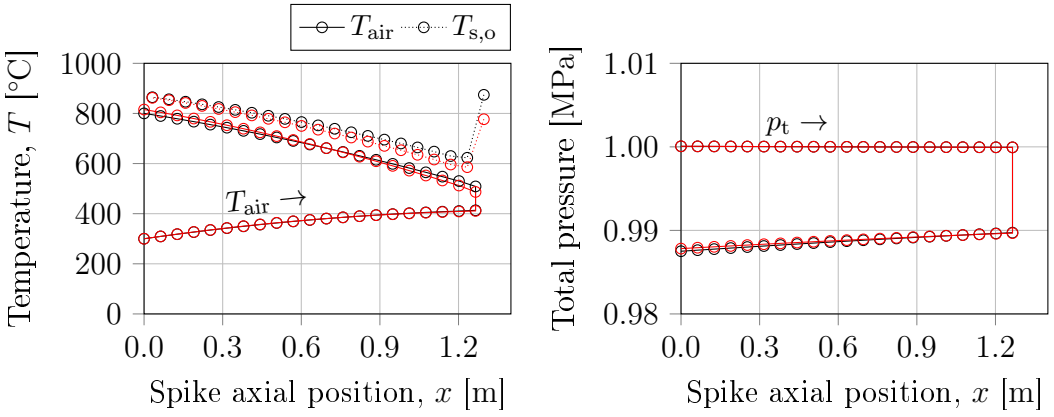

Figure I.2: Axial distribution of the SCRAP spike's outer tube temperature, $T_{\text{s,o}}$, the air temperature, T_{air} (left) as well as the total pressure (right); results from Lubkoll *et al.* (2020) are shown in black and the verification attempt is shown in red.

Appendix J

Blossaim, a deterministic aiming strategy for circular aperture receivers

This chapter develops of a new aiming heliostat aiming strategy implementation for a circular aperture receiver with a polar heliostat field such as the SUNflower, the Centrifugal Particle Receiver (CentRec) (Ebert *et al.*, 2019), the DIAPR receiver in the Tulip system Doron (2020) and the SOLUGAS receiver Korzynietz *et al.* (2016). This appendix along with the results of the strategy has been submitted for a SolarPACES conference publication (Erasmus *et al.*, 2021*c*).

J.1 Introduction

Vant-Hull (2002) described an aiming strategy to reduce the peak flux of a cylindrical receiver. The idea is that all heliostats are initially aimed at the equator of the cylinder. Half of the heliostats are then aimed a vertical offset above and below the equator so as to produce flux images with beam edges tangent to the receiver edges. Finally, individual heliostats are used to fill flux gaps. This leads to a relatively uniform receiver flux with a sharp gradient at the receiver edges. The strategy requires an estimation of the beam edge.

Sánchez-González and Santana (2015) implemented this strategy deterministically on a cylindrical receiver with a Gaussian convolution-projection flux modelling approach. He controlled the aiming strategy with a beam radius (r_{beam}) definition. The beam radius describes the extent of the quasi-circular flux distribution from each heliostat on the receiver. This was estimated in relation to the convolution standard error deviation (σ_{e}) of the Gaussian heliostat flux image on the receiver. Where $3\sigma_{\text{e}}$ would estimate a radius containing 99.7 % of the beam flux and σ_{e} a radius with 68 % of the flux.

Equation J.1 demonstrates the beam radius definition for each heliostat:

$$r_{\text{beam}} = SLR\, k\, \sigma_{\text{e}}, \tag{J.1}$$

where the slant range (SLR) is the distance between the heliostat and the receiver, k is a multiplier between $0 \leq k \leq 3$ used to control the number of standard deviations of flux considered part of the beam radius. A smaller k results in a scattered distribution and more spillage because the aiming points are closer to the receiver edges. The convolution standard deviation, (σ_{e}), is calculated from:

$$\sigma_{\text{e}} = \sqrt{\sigma_{\text{sun}}^2 + 2(1 + \cos^2 \omega)\sigma_{\text{slope}}^2 + \sigma_{\text{track}}^2}, \tag{J.2}$$

where σ_{sun} is the sunshape standard deviation, ω is the angle between the heliostat normal and the sun beam unit vectors, σ_{slope} is the slope error and σ_{track} is the tracking error.

The beam radius of heliostats planted nearer to the receiver are smaller and those farther away produce larger flux images on the receiver. Thus, incorporating SLR, the strategy aims far away heliostats nearer to the equator and nearby heliostats toward the aperture edges to reduce spillage.

J.2 Implementation

The Blossaim implementation differs from the previous implementation in that there is an additional degree of freedom on the position of each aim point. The implementation requires a combination of a vertical and horizontal offset for each aim point. Figure J.1 qualitatively illustrates the aiming parameters of Blossaim.

All heliostats are aimed so that the respective beam edges draw the circumference of the circular aperture, this constrains the radial distance of each aim point from the aperture centre as shown in Figure J.1.

Throughout the progression of solar time, the optical efficiency distribution of the heliostat field changes. It is therefore necessary for the strategy to deterministically produce similar flux uniformity on the aperture while the field efficiency distribution is changing. To achieve this, the aiming points of heliostats and their rows are systematically alternated (from the aiming points of their neighbours) between adjacent regions of the aperture. Moreover, each consecutive heliostat row aims inside the alternate semicircle (top and bottom halves) of the aperture. The heliostats are also individually aimed within each row at an angular progression around the aperture midpoint. The angular progression starts with a side heliostats of each row (farthest from the N-S symmetry axis of the field) aiming at an edge of the semicircle with an aiming angle of $\theta_{\text{aim}} = 90°$. With each consecutive heliostat, the progression alternates between the left and right sides of the aperture with a sign change of

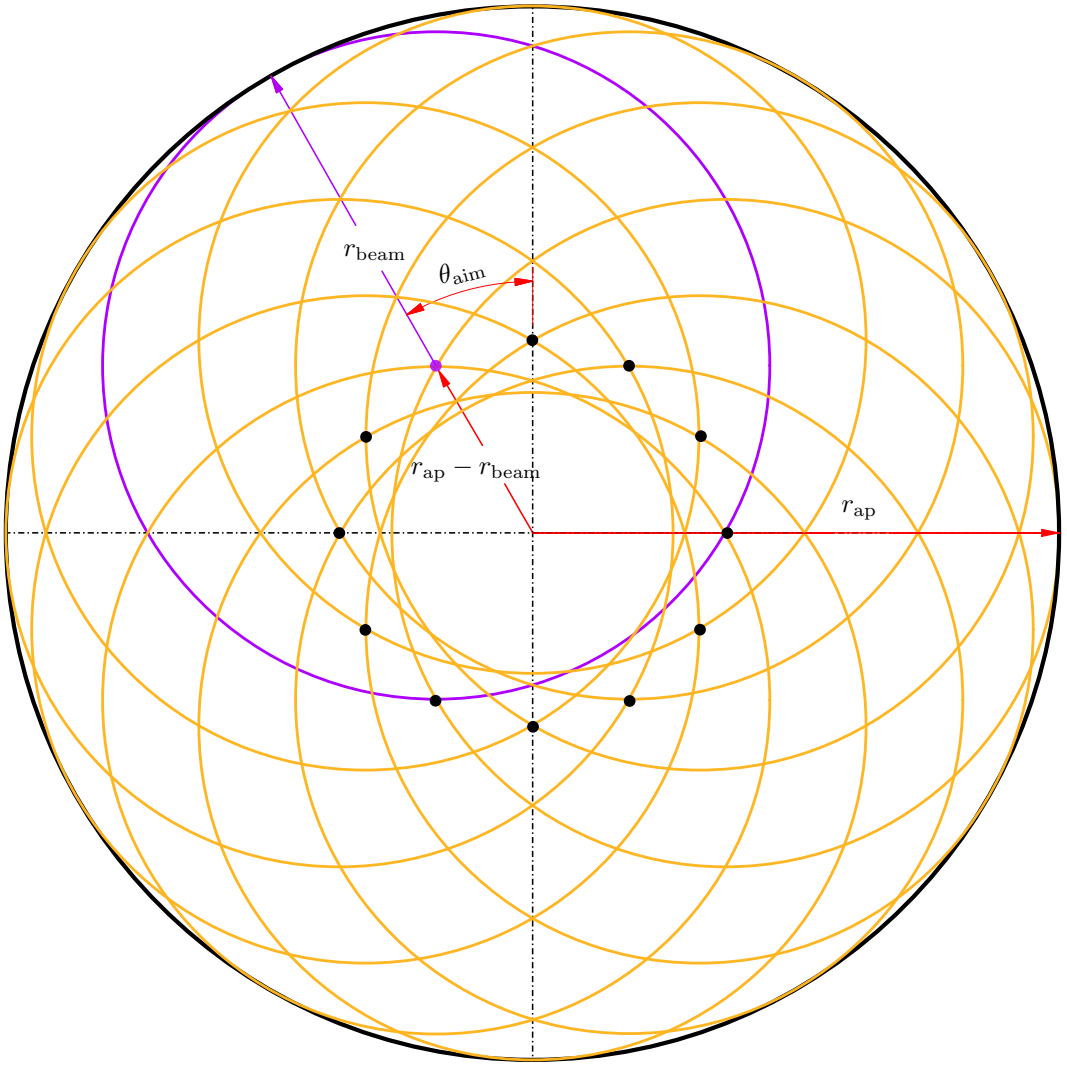

Figure J.1: Qualitative illustration of Blossaim's aiming parameters with a regular distribution of θ_{aim} and a constant r_{beam}.

θ_{aim} to progress towards the middle of the semicircle. The centreline heliostats therefore aim towards the vertical centreline of the aperture ($\theta_{\text{aim}} = 0°$).

The alternation between the left and right sides of the aperture is key to producing a similar relative flux distribution throughout the day. The angular development is also non-linear because it was found that a linear progression creates an unsymmetrical flux distribution where the more optically efficient (centreline) heliostats outshine the side heliostats. It was found that a product combination of logarithmic and linear functions for the heliostat aiming angle (θ_{aim}) creates a near uniform flux distribution. This function densifies the heliostat aiming points near the horizontal centreline of the aperture.

The linear and logarithmic functions were created using the 'linspace' and 'nonLinspace' functions respectively in Matlab®. The linspace is defined be-

tween the extents of a tuned damping factor (0.6 was found to be most suitable in this case) and 1 while the nonLinspace is a $\log_{10}$ spacing defined between 0° and 90°. Between these extents, there are as many discrete aiming angles as half the heliostats in each row. If the row has an odd number of heliostats, the middle heliostat is excluded from the nonlinear spacing and aims directly at the vertical centreline ($\theta_{\text{aim}} = 0$). The generation of the aiming angles for any row is demonstrated in the Matlab code snippet:

```
%number of heliostats in the row:
nhr
%Logarythmic spacing:
v_thetas = nonLinspace(0,pi/2,nhr,'log10');
%Tuned damping factor:
damp=0.6;
%Linear damping function:
damping = linspace(damp,1,nhr);
%if nhr is odd:
if mod(nhr,2) ~= 0
%compile aiming angles:
thetasHalf = v_thetas(3:2:end) .* damping(3:2:end);
thetas_r1=-(-1).^(1:1:nhr).*[fliplr(thetasHalf) 0 thetasHalf];
%if nhr is odd:
else
thetasHalf = v_thetas(2:2:end) .* damping(2:2:end);
%compile aiming angles:
thetas_r1=-(-1).^(1:1:nhr).*[fliplr(thetasHalf) thetasHalf];
end
```

For the example of the East half of the first row (the first 16 heliostats in first row of the Heliopod field described in Chapter 7, Section J.1), the aiming point angles progress with heliostat number approximately according to:

$$\theta_{\text{aim}} = -(-1)^n \left[0.576 + 0.0242(18 - n)\right] \cdot \left[0.0885 + 1.21 \log_{10}(18 - n)\right] \quad \text{[rad]}, \tag{J.3}$$

where n is the heliostat identification number within the first row with $n = 1$ representing the first heliostat on the East side. It must be observed that the first product term in the equation changes the sign for odd heliostats in the row. The aiming points of the West half of this row is a reflected version of the East side around the vertical axis of the aperture. The deterministic aiming points of the first two rows are shown in Figure J.2. Here, the heliostats are indexed according to $H_{m,n}$, where m is the heliostat row and n is the heliostat identification number.

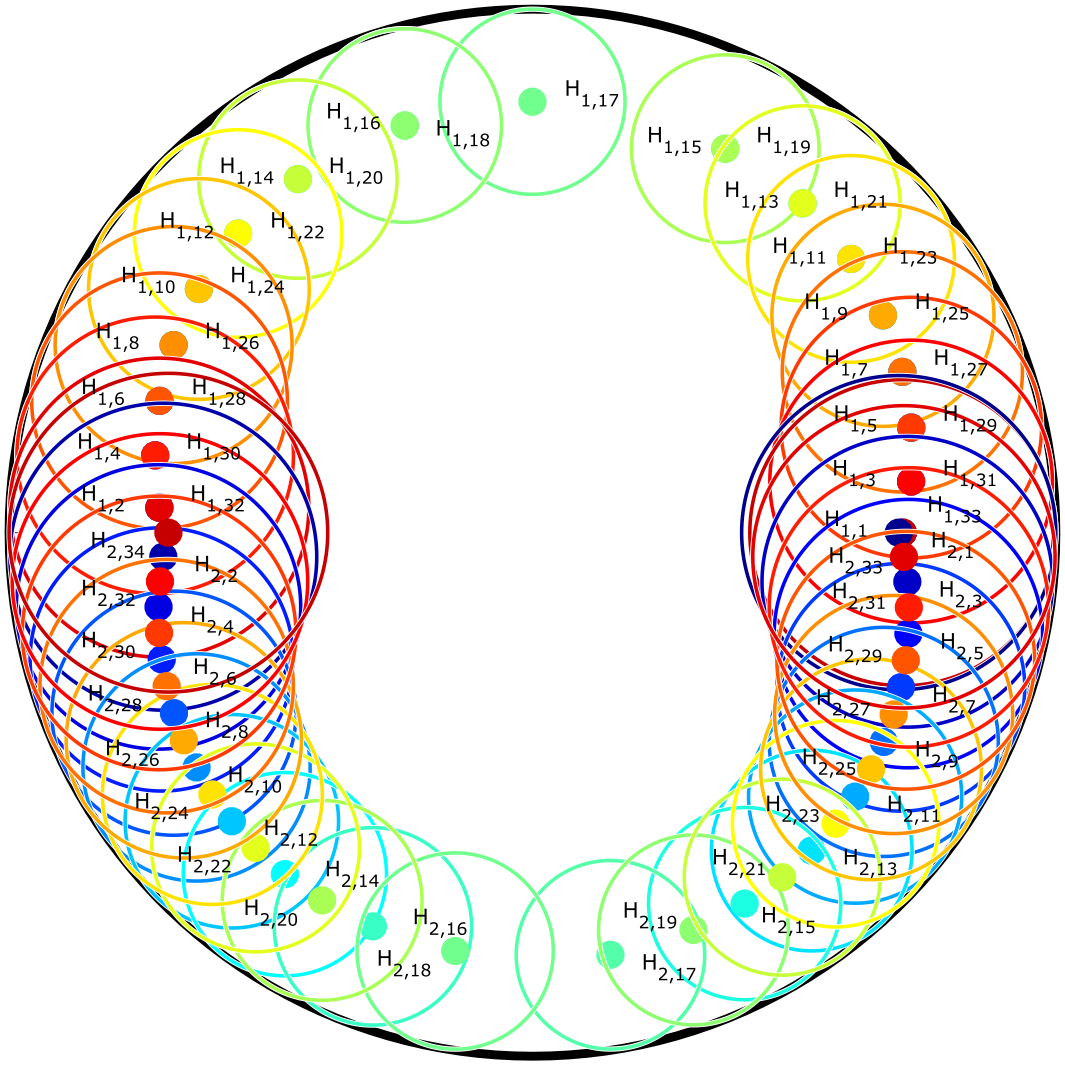

Figure J.2: The aperture aiming points and approximate beam images (with aiming parameter: $k = 0.8$) of the first two rows of the Heliopod field with a RGB colour map; red and blue represent the east and west side heliostats respectively and green the central heliostats; $H_{1,1}$ refers to the first East side heliostat in the first row for example.

It can be observed that the beam radius is larger for side heliostats because the distance to the receiver is larger. It is also depicted that the density of aiming points are greater at the left and right sides of the aperture.

Blossaim can now be implemented in Chapter 7 to reduce the peak flux of the SUNflower. The results of Blossaim on the SUNflower aperture is presented in Section 7.3.5.

Appendix K

The SUNflower's flow domain

Figure K.1 describes the flow domain of the 3D CFD model. Three faces are depicted in the figure: the transparent boundary as well as two of the three symmetry boundaries. The sector makes up the 1/12 repeating part of an axial revolution. The inlet and outlet boundary conditions are shown in the figure along with the assigned cell-zones. The heat source is implemented within the thin exterior heat transfer volume. Heat moves from the heat source primarily towards the convection domain through the outer shell but also in the opposite direction — through the transparent cell-zone and the semi-transparent boundary through radiation as a thermal loss to ambient.

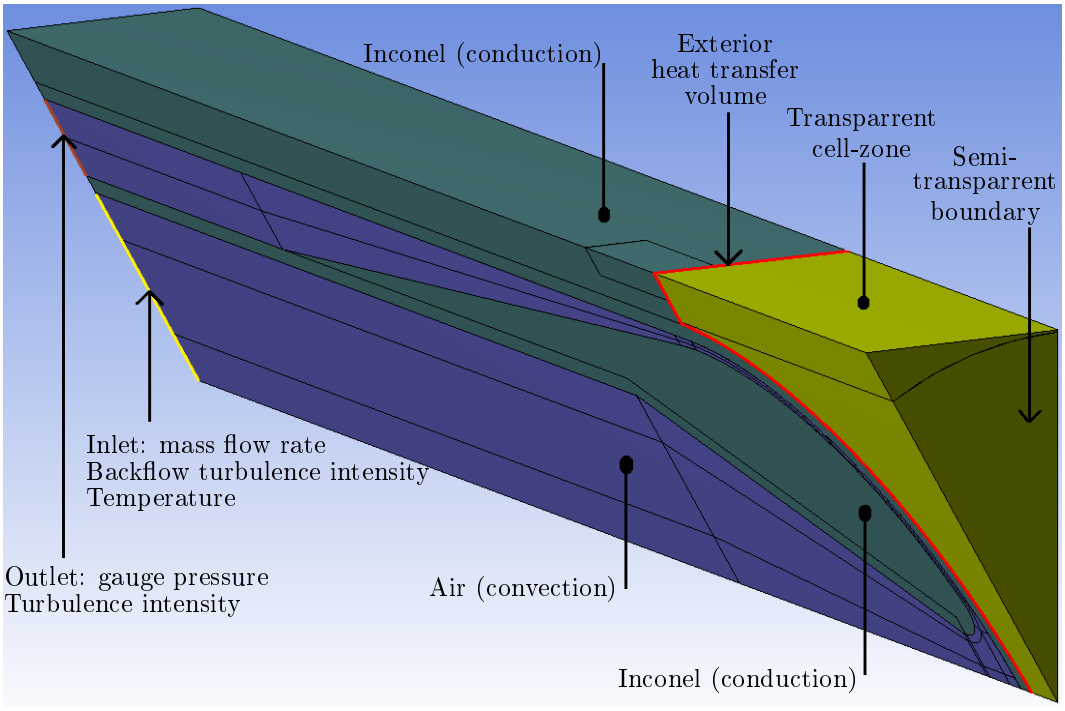

Figure K.1: Flow domain of the SUNflower's CFD model.

List of References

Adkins, R.C., Jacobsen, O.H. and Chevalier, P. (1983). A preliminary study of annular diffusers with constant diameter outer walls (suitable for turbine exits). *The American Society of Mechanical Enigneers*, vol. 1, no. 83-GT-218.
Available at: https://doi.org/10.1115/83-GT-218

ANSYS (2016). Fluent theory guide. in: ANSYS documentation. Tech. Rep. 17, ANSYS.

Boljanovic, V. (2007). 6.44 Frustum of Cone. Date accessed: October 2020.
Available at: https://app.knovel.com/hotlink/khtml/id:kt008X3L71/applied-mathematical/frustum-of-cone

Brand, J.H. and Dowhan, M.J. (2009). Anti-icing apparatus and method for aero-engine nose cone. Date accessed: October 2020.
Available at: https://patents.google.com/patent/US20090120099A1

Bredberg, J. (2000). On the wall boundary condition for turbulence models. Tech. Rep., Department of Thermo and Fluid Dynamics, Chalmers University of Technology.

Buck, R., Bräuning, T., Denk, T., Pfänder, M., Schwarzbözl, P. and Tellez, F. (2002). Solar-Hybrid Gas Turbine-based Power Tower Systems (REFOS). *Journal of Solar Energy Engineering*, vol. 124, no. 1, p. 2. ISSN 0199-6231.
Available at: https://doi.org/10.1115/1.1445444

Çengel, Y.A. and Boles, M.A. (2014). *Thermodynamics: An Engineering Approach*. 8th edn. McGraw-Hill Education, New York. ISBN 978-0-07-339817-4.

Çengel, Y.A. and Cymbala, J.M. (2014). *Fluid Mechanics Fundamentals and Applications*. 3rd edn. McGraw-Hill, New York. ISBN 978-0073380322.

Çengel, Y.A. and Ghajar, A.J. (2011). *Heat and Mass Transfer: Fundamentals and Applications*. 4th edn. McGraw-Hill, Inc., New York. ISBN 978-007-131112-0.

Craig, K.J., Slootweg, M. and Meyer, J.P. (2018*a*). Heat transfer enhancement in molten salt central receiver using jet impingement. In: *5th Southern African Solar Energy Conference (SASEC)*, vol. 5. Durban, South Africa. Date accessed: October 2020.
Available at: https://www.sasec.org.za/full_papers/53.pdf

Craig, K.J., Slootweg, M., Meyer, J.P., Robbins, J.C., Kotzé, R., Honiball, N.J.M., Grobler, E., Oosthuizen, T.J. and Winterbach, W. (2018*b*). CFD simulation of solar receiver jet impingement heat transfer: RANS vs LES. In: *16th International Heat Transfer Conference*, vol. 16, pp. 1971–1978.
Available at: `https://doi.org/10.1615/IHTC16.cms.023262`

Cumpston, J. and Coventry, J. (2017). Derivation of error sources for experimentally derived heliostat shapes. In: *AIP Conference Proceedings, SolarPACES 2016*, vol. 1850, p. 030013. Abu Dhabi.
Available at: `https://aip.scitation.org/doi/abs/10.1063/1.4984356`

Damiani, L., Montecucco, M. and Prato, A.P. (2013). Conceptual design of a bayonet-tube steam generator for the ALFRED lead-cooled reactor. *Nuclear Engineering and Design*, vol. 265, pp. 154 – 163. ISSN 0029-5493.
Available at: `https://doi.org/10.1016/j.nucengdes.2013.06.021`

Dixon, S.L. (1998). *Fluid mechanics and thermodynamics of turbomachinery*. 4th edn. Elsevier. ISBN 978-0-7506-7059-3. Date accessed: October 2020.
Available at: `https://app.knovel.com/hotlink/khtml/id:kt005H7WW4/fluid-mechanics-thermodynamics/some-remarks-diffuser`

Domínguez-Bravo, C.-A., Bode, S.-J., Heiming, G., Richter, P., Carrizosa, E., Fernández-Cara, E., Frank, M. and Gauché, P. (2016). Field-design optimization with triangular heliostat pods. In: *AIP Conference Proceedings, SolarPACES 2015*, vol. 1734, p. 070006. Cape Town.
Available at: `https://aip.scitation.org/doi/abs/10.1063/1.4949153`

Doron, P. (2020). A high temperature receiver for a solarized micro-gas-turbine. In: *AIP Conference Proceedings, SolarPACES 2019*. Daegu.

Dowling, N. (2013). *Mechanical Behavior of Materials: Engineering Methods for Deformation, Fracture, and Fatigue*. 4th edn. Pearson Prentice Hall. ISBN 9780131395060.

Ebert, M., Amsbeck, L., Rheinländer, J., Schlögl-Knothe, B., Schmitz, S., Sibum, M., Uhlig, R. and Buck, R. (2019). Operational experience of a centrifugal particle receiver prototype. In: *AIP Conference Proceedings, SolarPACES 2018*, vol. 2126, p. 030018. Casablanca.
Available at: `https://aip.scitation.org/doi/abs/10.1063/1.5117530`

Erasmus, D.J. (2018). Jet impingement heat transfer within a spherical dome. Tech. Rep., Stellenbosch University.

Erasmus, D.J., Lubkoll, M., Craig, K. and Von Backström, T.W. (2021*a*). Impingement heat transfer with pressure recovery. *Heat and Mass Transfer, Under preparation.*

Erasmus, D.J., Lubkoll, M., Craig, K.J. and Von Backström, T.W. (2020*a*). Capability of a novel impingement heat transfer device for application in future solar

thermal receivers. In: *AIP Conference Proceedings, SolarPACES 2019*, 00017. Daegu.

Erasmus, D.J., Lubkoll, M. and Von Backström, T.W. (2020*b*). Jet impingement heat transfer within a hemisphere. *Heat and Mass Transfer*.
Available at: `http://dx.doi.org/10.1007/s00231-020-02977-9`

Erasmus, D.J., Sánchez-González, A., Lubkoll, M., Craig, K. and Von Backström, T.W. (2021*b*). Performance outlook of the SUNflower receiver. *Solar Energy, Under preparation*.

Erasmus, D.J., Sánchez-González, A. and Von Backström, T.W. (2021*c*). Blossaim, a deterministic aiming strategy for circular aperture receivers. In: *AIP Conference Proceedings, SolarPACES 2020, Under review*. Online conference.

Erasmus, D.J., Von Backström, T.W., McDougall, D. and Lubkoll, M. (2019). Heat transfer device, PCT international patent application. PCT/IB2019/060650.

Eucken, A. (1940). Allgemeine Gesetzmäßigkeiten für das Wärmeleitvermögen verschiedener Stoffarten und Aggregatzustände. *Forschung auf dem Gebiet des Ingenieurwesens A*, vol. 11, no. 1, pp. 6–20. ISSN 1434-0860.
Available at: `https://doi.org/10.1007/BF02584103`

Fives North American Combustion, I. (2001). *North American Combustion Handbook*. page 85, 3rd edn. Fives North American Combustion, Inc. ISBN 978-0-9601596-2-8. Date accessed: October 2020.
Available at: `https://app.knovel.com/hotlink/toc/id:kpCHVIE001/north-american-combustion/north-american-combustion`

Garbrecht, O., Al-sibai, F., Kneer, R. and Wieghardt, K. (2012). Numerical Investigation of a New Molten Salt Central Receiver Design. In: *SolarPACES 2012*. Marrakech.

Garrido, J., Aichmayer, L., Abou-Taouk, A. and Laumert, B. (2019). Experimental and numerical performance analyses of dish-stirling cavity receivers: Radiative property study and design. *Energy*, vol. 169, pp. 478 – 488. ISSN 0360-5442.
Available at: `https://doi.org/10.1016/j.energy.2018.12.033`

Gauché, P., Von Backström, T.W., Brent, A.C. and Rudman, J. (2016). CSP opportunity and challenges in a national system: The WWF renewable vision for a 2030 South African electricity mix. In: *AIP Conference Proceedings, SolarPACES 2015*, vol. 1734, p. 080002. Cape Town.
Available at: `https://aip.scitation.org/doi/abs/10.1063/1.4949182`

Greene, G., Finfrock, C. and Irvine, T. (2000). Total Hemispherical Emissivity of Oxidized Inconel 718 in the Temperature Range 300C – 1000C. *Experimental Thermal and Fluid Science*, vol. 22, no. 3-4, pp. 145–153. ISSN 08941777.

Grobbelaar, D. (2019). *Improving the Heat Transfer Characteristicsof the Spiky Central Receiver (SCRAP) using Helically Swirled Fins.* Master's thesis, Stellenbosch University.
Available at: `http://hdl.handle.net/10019.1/105893`

IRENA (2020). *Renewable Power Generation Costs in 2019.* International Renewable Energy Agency, Abu Dhabi. ISBN 978-92-9260-244-4. Date accessed: October 2020.
Available at: `https://www.irena.org/publications/2020/Jun/Renewable-Power-Costs-in-2019`

Johnston, I.H. (1953). The effect of inlet conditions on the flow in annular diffusers. Memorandum M.167, National Gas Turbine Establishment.

Kobayashi, T., Banno, M. and Amaoka, K. (2000). Leading edge structure of aircraft airfoil and method of fabricating the same. Date accessed: October 2020.
Available at: `https://patents.google.com/patent/US6119978`

Kolb, G.J., Ho, C.K., Mancini, T.R. and Gary, J.A. (2011). Power tower technology roadmap and cost reduction plan. Tech. Rep. SAND2011-2419, Sandia National Laboratories, Albuquerque, New Mexico.

Korzynietz, R., Brioso, J.A., Del Río, A., Quero, M., Gallas, M., Uhlig, R., Ebert, M., Buck, R. and Teraji, D. (2016). Solugas — Comprehensive analysis of the solar hybrid Brayton plant. *Solar Energy*, vol. 135, pp. 578–589. ISSN 0038-092X.
Available at: `https://doi.org/10.1016/j.solener.2016.06.020`

Kröger, D.G. (2004). *Air-cooled Heat Exchangers and Cooling Towers.* 1st edn. University of Stellenbosch. ISBN 978-1593700195.

Kröger, D.G. (2008). Spiky Central Receiver Air Pre-heater (SCRAP). Tech. Rep., Stellenbosch University.

Kröger, D.G. (2012). SUNSPOT — The Stellenbosch UNiversity Solar POwer Thermodynamic cycle. Tech. Rep., Stellenbosch University.

Landman, W.A. (2017). *Optical performance of the reflective surface profile of a heliostat.* Doctoral thesis, Stellenbosch University.
Available at: `http://scholar.sun.ac.za/handle/10019.1/101210`

Langtry, R.B. and Menter, F.R. (2009). Correlation-based transition modeling for unstructured parallelized computational fluid dynamics codes. *AIAA Journal*, vol. 47, no. 12, pp. 2894–2906.
Available at: `https://doi.org/10.2514/1.42362`

Lee, D.H., Chung, Y.S. and Won, S.Y. (1999). The effect of concave surface curvature on heat transfer from a fully developed round impinging jet. *International Journal of Heat and Mass Transfer*, vol. 42, no. 13, pp. 2489–2497. ISSN 00179310.
Available at: `https://doi.org/10.1016/S0017-9310(98)00318-4`

Lee, H.-J., Kim, J.-K., Lee, S.-N., Yoon, H.-K., Kang, Y.-H. and Park, M.-H. (2015). Calculation of optical efficiency for the first central-receiver solar concentrator system in korea. *Energy Procedia*, vol. 69, pp. 126 – 131. ISSN 1876-6102. International Conference on Concentrating Solar Power and Chemical Energy Systems, SolarPACES 2014.
Available at: https://doi.org/10.1016/j.egypro.2015.03.015

Li, L. (2014). *Numerical study of surface heat transfer enhancement in an impinging solar receiver*. Master's thesis, Uppsala University. Date accessed: October 2020.
Available at: http://urn.kb.se/resolve?urn=urn:nbn:se:uu:diva-237365

Liu, Z. and Feng, Z. (2011). Numerical simulation on the effect of jet nozzle position on impingement cooling of gas turbine blade leading edge. *International Journal of Heat and Mass Transfer*, vol. 54, no. 23-24, pp. 4949–4959. ISSN 0017-9310.
Available at: https://dx.doi.org/10.1016/j.ijheatmasstransfer.2011.07.008

Lubkoll, M. (2017). *Performance characteristics of the Spiky Central Receiver Air Pre-heater (SCRAP)*. Doctoral thesis, Stellenbosch University.
Available at: http://hdl.handle.net/10019.1/101295

Lubkoll, M., Erasmus, D.J., Harms, T.M., Von Backström, T.W. and Kröger, D.G. (2020). Performance characteristics of the spiky central receiver air pre-heater (SCRAP). *Solar Energy*, vol. 201, pp. 773–786. ISSN 0038-092X.
Available at: https://doi.org/10.1016/j.solener.2020.03.027

Lubkoll, M., Harms, T.M. and Von Backström, T.W. (2017). Introduction to heat transfer test setup for the SCRAP receiver. In: *AIP Conference Proceedings, SolarPACES 2016*, vol. 1850, pp. 040003–1 – 040003–8. Abu Dhabi. ISBN 9780735415225.
Available at: https://doi.org/10.1063/1.4984399

Ma, T., Zeng, M., Ji, Y., Zhu, H. and Wang, Q. (2011). Investigation of a novel bayonet tube high temperature heat exchanger with inner and outer fins. *International Journal of Hydrogen Energy*, vol. 36, no. 5, pp. 3757 – 3768. ISSN 0360-3199.
Available at: https://doi.org/10.1016/j.ijhydene.2010.12.039

Manglik, R. (1987). *Heat transfer fluid flow data books*. Genium Publishing Corporation. ISBN 978-0-931690-02-0. Date accessed: October 2020.
Available at: https://app.knovel.com/hotlink/toc/id:kpHTFFDB0F/heat-transfer-fluid-flow/heat-transfer-fluid-flow

MatWeb (2019). Overview of materials for acrylonitrile butadiene styrene (ABS), molded. Online. Date accessed: October 2020.
Available at: http://www.matweb.com/search/datasheet_print.aspx?matguid=eb7a78f5948d481c9493a67f0d089646&n=1

McDougall, D. (2019). *Numerical simulation of jet impingement cooling of the inside of a hemisphere with application to SCRAP*. Master's thesis, Stellenbosch University.
Available at: `http://hdl.handle.net/10019.1/106154`

Menter, F.R. (1993). Zonal two equation k-ω turbulence models for aerodynamic flows. *AIAA Paper 93-2906. Date accessed: October 2020.*
Available at: `https://ntrs.nasa.gov/search.jsp?R=19960044572`

Mikron Instrument Company (2003). *Table of emissivity of various surfaces*. Mikron Instrument Company Inc.

Neises, T. and Turchi, C. (2014). A comparison of supercritical carbon dioxide power cycle configurations with an emphasis on csp applications. *Energy Procedia*, vol. 49, pp. 1187 – 1196. ISSN 1876-6102. Proceedings of the SolarPACES 2013 International Conference.
Available at: `https://doi.org/10.1016/j.egypro.2014.03.128`

Quick, J. (2020). *Computational Investigation of Swirling Jet Impingement in a Concentrated Solar Tower Cavity Receiver*. Master's thesis, University of Pretoria.

SABS (2012). South african national standard: 347:2012: Categorization and conformity assessment criteria for all pressure equipment. Tech. Rep., SABS.

Sánchez-González, A., Rodríguez-Sánchez, M.R. and Santana, D. (2018). Aiming factor to flatten the flux distribution on cylindrical receivers. *Energy*, vol. 153, pp. 113 – 125. ISSN 0360-5442.
Available at: `https://doi.org/10.1016/j.energy.2018.04.002`

Sánchez-González, A. and Santana, D. (2015). Solar flux distribution on central receivers: A projection method from analytic function. *Renewable Energy*, vol. 74, pp. 576–587. ISSN 0960-1481.
Available at: `https://doi.org/10.1016/j.renene.2014.08.016`

Saravanamuttoo, H., Rogers, G.F.C. and Cohen, H. (2001). *Gas Turbine Theory*. 5th edn. Pearson Education, Upper Saddle River, United States. ISBN 013015847X.

Schobeiri, M.T. (2010). *Fluid Mechanics for Engineers*. Springer. ISBN 978-3-642-11594-3.

Siebers, D.L. and Kraabel, J.S. (1984). Estimating convective energy losses from solar central receivers. Tech. Rep. SAND-84-8717, Sandia National Laboratories, Albuquerque, New Mexico.
Available at: `https://doi.org/10.2172/6906848`

Slootweg, M., Craig, K.J. and Meyer, J.P. (2018). Investigation into central receiver design for optimal optical and thermal performance. In: *5th Southern African Solar Energy Conference (SASEC)*. Durban, South Africa. Date accessed: October 2020.
Available at: `https://www.sasec.org.za/full_papers/54.pdf`

Slootweg, M., Craig, K.J. and Meyer, J.P. (2019). A computational approach to simulate the optical and thermal performance of a novel complex geometry solar tower molten salt cavity receiver. *Solar Energy*, vol. 187, pp. 13 – 29. ISSN 0038-092X.
Available at: `https://doi.org/10.1016/j.solener.2019.05.003`

SMC (2004). *Incoloy alloy 800*. SMC-046. Special Metals Corporation, Huntington.

SMC (2007). *Inconel alloy 718*. SMC-045. Special Metals Corporation, Huntington.

SMC (2019). *Product handbook of high-performance nickel alloys*. Special Metals Corporation, Huntington.

Stine, W.B. and Geyer, M. (2001). Power from the sun. Date accessed: October 2020.
Available at: `http://www.powerfromthesun.net/book.html`

Swindeman, R.W. and Marriott, D.L. (1994). Criteria for design with structural materials in combined-cycle applications above 815°F. *Journal of Engineering for Gas Turbines and Power*, vol. 116, no. 2, pp. 352–359.
Available at: `https://doi.org/10.1115/1.2906827`

Taylor, J. (1997). *An introduction to error analysis: The study of uncertainties in physical measurement*. 2nd edn. University Science Books, USA.

Vant-Hull, L.L. (2002). The Role of "Allowable Flux Density" in the Design and Operation of Molten-Salt Solar Central Receivers. *Journal of Solar Energy Engineering*, vol. 124, no. 2, pp. 165–169. ISSN 0199-6231.
Available at: `https://doi.org/10.1115/1.1464124`

VDI (2010). *VDI-Wärmeatlas*. 10th edn. VDI-Verlag.

Wang, W. and Laumert, B. (2018 nov). An axial type impinging receiver. *Energy*, vol. 162, pp. 318 – 334. ISSN 0360-5442.
Available at: `https://doi.org/10.1016/j.energy.2018.08.036`

Wang, W., Laumert, B., Xu, H. and Strand, T. (2015). Conjugate heat transfer analysis of an impinging receiver design for a dish-Brayton system. *Solar Energy*, vol. 119, pp. 298–309.
Available at: `https://doi.org/10.1016/j.solener.2015.07.013`

Wu, W., Uhlig, R., Buck, R. and Pitz-Paal, R. (2015). Numerical simulation of a centrifugal particle receiver for high-temperature concentrating solar applications. *Numerical Heat Transfer, Part A: Applications*, vol. 68, no. 2, pp. 133–149.
Available at: `https://doi.org/10.1080/10407782.2014.977144`